

PHYSIKALISCHES INSTITUT

FAKULTÄT FÜR PHYSIK

KARLSRUHER INSTITUT FÜR TECHNOLOGIE

Experiments on Asymmetric dc-SQUIDs Searching for the Münchhausen Effect

Diplomarbeit

von

Susanne Butz

27. Mai 2010

Referent: **Prof. Dr. A.V. Ustinov**
Korreferent: Prof. Dr. W. Wulfhekel

Contents

Introduction	1
1 The Basics of Josephson Tunnel Junctions and dc-SQUIDs	3
1.1 Superconductivity	3
1.2 The Josephson Junction	4
1.2.1 The Josephson Relations	4
1.2.2 The Resistively and Capacitively Shunted Junction Model	4
1.2.3 Escape Mechanisms	7
1.3 The dc-SQUID	9
1.3.1 Flux Dependence	12
1.3.2 Escape Mechanisms in Two Dimensions	15
2 The Theory of the Münchhausen Effect	17
2.1 Basic Idea	17
2.2 Strong Damping and Zero Temperature	18
2.3 Flux Dependence	20
3 Numerical Evaluation of the Asymmetric dc-SQUID	23
3.1 The Heun Method	23
3.2 Application to the Asymmetric dc-SQUID	24
4 Experimental Realization and Setup	25
4.1 Chip Design	25
4.2 Experimental Setup	26
4.3 Current Ramp Measurements	26
5 Experimental Results	29
5.1 SQUID S3	29
5.1.1 $I(V)$ -Characteristic	29
5.1.2 Current Ramp Measurements	31
5.1.3 Conclusions	38
5.2 SQUID S4	38
5.2.1 Current Ramp Measurements	39
5.2.2 Conclusions	46
5.3 SQUID S2	46
5.3.1 $I(V)$ -characteristic	46
5.3.2 Current Ramp Measurements	48
5.3.3 Conclusions	56
Conclusions and Outlook	57
A Chip and Sample Design	59

B Measurement Setup	61
C Nomenclature of Critical Currents	63
Zusammenfassung	65
Bibliography	69
Acknowledgments	71

Introduction

First of all: This thesis has nothing to do with people riding on cannonballs. Instead, dc-SQUIDS with large inductance and an additional capacitive asymmetry are investigated.

Superconducting QUantum Interference Devices (SQUIDS) attained a great deal of interest ever since it became clear that they can be used to resolve changes in magnetic fields as small as 10^{-14} T [Sch97]. A SQUID consists of a superconducting loop that is intersected by either one Josephson junction (rf-SQUID) or two Josephson junctions in parallel (dc-SQUID). One of the many applications where their large sensitivity is very much appreciated is their use as readout devices in the developing field of superconducting quantum bits. When using the SQUID as measurement device, the main figure of merit is its sensitivity and reliability.

However, in this work the SQUID itself is studied in a rather interesting variation. V. Geshkenbein, A. Thomann and G. Blatter theoretically predicted the escape of a classical degree of freedom out of a metastable minimum at zero temperature provided that it is coupled to a quantum mechanical degree of freedom [TGB09]. Since such a behavior reminds very much of Baron Münchhausen, who claimed to have himself (and his horse) rescued out of a swamp by pulling at his own hair, this escape mechanism was named “Münchhausen” effect.

Experimentally, such a system can be realized by a dc-SQUID that has two small junctions, one of them being shunted with a large capacitor. The equation of motion for a single Josephson junction within the RCSJ model is analogous to the equation of motion of a pendulum under external force: The bias current through the junction corresponds to a constant external torque and its intrinsic capacitance can be considered as the mass equivalent. Thus, a large shunting capacitor forces the shunted junction to behave classically. Additionally, if the capacitance of the unshunted junction is small enough, this junction exhibits quantum mechanical behavior such as the ability to tunnel through a potential barrier.

The aim of this work is to test the predictions made in Ref. [TGB09] and examine further properties of such a dynamically asymmetric system. The dc-SQUIDS under investigation have large inductances which is one of the conditions to observe the Münchhausen effect. This also creates a system with two almost independent variables and allows for the study of effects like phase diffusion in two dimensions.

Outline

In the first chapter, the basic properties of the Josephson tunnel junction and the dc-SQUID are in the center of attention. Additionally, thermal and quantum mechanical escape mechanisms for an escape out of metastable minima in one and two dimensions are reviewed and the phenomenon of phase diffusion in underdamped junctions is explained. Chapter 2 discusses the main features of the Münchhausen effect for the simple case of strong damping. The next chapter deals with the technical details of the numerical simulation that was implemented to include the effect of nonzero temperature on the system. In Chapter 4, the design of the SQUIDS and the experimental realization of the measurement procedure is considered. The measured results together with numerical simulations are presented and evaluated in Chapter 5. Due to different parameter regimes each of the different SQUIDS is considered separately. Finally, the

last part of this work contains a summary of the main results and presents the conclusions that can be drawn. It also contains an outlook on what would be interesting to investigate further.

Chapter 1

The Basics of Josephson Tunnel Junctions and dc-SQUIDs

This chapter gives a short overview over superconductivity and Josephson junctions. The basic properties of Josephson tunnel junctions and their use in superconducting quantum interference devices (SQUIDs), focussing on dc-SQUIDs, will be discussed.

1.1 Superconductivity

When Heike Kamerlingh Onnes first observed in 1911 [KO11] that the resistance of some metals disappeared below a certain material specific temperature, he probably never would have guessed that there was another side to the coin superconductivity, namely perfect diamagnetism. This discovery was made by Walther Meissner and Robert Ochsenfeld in 1933 [MO33]. Additionally, it took until 1957 to find the explanation on the microscopic scale which was done by John Bardeen, Leon N. Cooper, and John R. Schrieffer [BCS57].

In their theory they claim that two electrons couple to each other, forming a so-called Cooper pair. The coupling between the two electrons is due to a weak electron-phonon interaction which results in an effective attraction between the two electrons.

If the Cooper pair is considered as one particle, it has spin 0. Thus it behaves according to Bose-Einstein statistics and at $T = 0$ all Cooper pairs occupy the ground state.

Another consequence of the coupling is the resulting energy gap Δ between the ground state, occupied by Cooper pairs, and the excited states of the quasiparticles which, simplified, can be considered as single electrons. This is also the reason for the perfect conductivity of the superconductor. Scattering is forbidden because there are no states to scatter into.

In order to describe the macroscopic phenomena arising from superconductivity, instead of using the microscopic BCS theory, it is much more convenient to use the macroscopic Ginzburg-Landau theory developed by Vitali L. Ginzburg and Lew D. Landau, that can be deduced as limiting case of the microscopic theory [Tin04].

The wave function describing the macroscopic superconducting state is then given as

$$\Psi(\vec{r}, t) = |\Psi(\vec{r}, t)| \exp[i\theta(\vec{r}, t)] \quad (1.1)$$

where $|\Psi(\vec{r}, t)|^2 = n_s$ corresponds to the local density of superconducting electron pairs.

Flux Quantization When a loop is formed out of a superconducting material, the wave function must be single-valued after one turn around the loop. This leads to flux quantization [Sch97]. The flux threading a superconducting loop can only assume integer numbers of the flux quantum $\Phi_0 = h/(2e) = 2.07 \cdot 10^{-15}$ Vs.

1.2 The Josephson Junction

1.2.1 The Josephson Relations

A Josephson tunnel junction is formed by two superconductors that are separated by a thin insulating layer (cf. Fig. 1.1). The superconducting wave function decays exponentially in this layer but if it is thin enough the wave function is still appreciable at the other side of the barrier. Thus, Cooper pairs can cross the barrier. This creates a supercurrent that only depends on the difference $\varphi = \theta_1 - \theta_2$ between the phases of the two wave functions provided that the absolute values of the wave functions are equal on both sides of the insulator [Sch97].

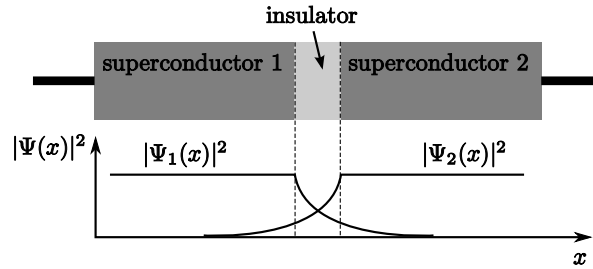


Fig. 1.1: Schematic of a Josephson tunnel junction (top) and the exponential decay of the superconducting wave function inside the insulator (bottom).

Brian D. Josephson [Jos62] developed two equations connecting the phase difference across the junction with the current I through, and voltage V across it.

$$I = I_c \sin \varphi \quad (1.2)$$

$$\frac{d\varphi}{dt} = \frac{2eV}{\hbar} \quad (1.3)$$

As long as the current through the junction is smaller than the critical value I_c , the junction is in the zero voltage state. The current through the junction then flows without dissipation and is sufficiently described by Eq. (1.2). If, however, the bias current exceeds the critical value, it cannot be sustained only by Cooper pairs, and quasiparticle (i.e. single electron) tunneling creates an additional contribution to the current. The junction then enters the normal resistive state. A voltage drop occurs and the phase difference is not constant anymore (cf. Eq. (1.3)).

1.2.2 The Resistively and Capacitively Shunted Junction Model

The resistively and capacitively shunted junction (RCSJ) model describes the time dependence of the phase difference φ across the junction. A resistor in parallel to the ideal junction models the quasiparticle resistance and a capacitor in parallel reflects the intrinsic capacitance between the two superconductors. The equivalent circuit is presented in Fig. 1.2.

With Kirchhoff's current law the current distribution across the three branches is given as

$$I = I_c \sin \varphi + \frac{V}{R} + C \frac{dV}{dt} \quad (1.4)$$

$$= I_c \sin \varphi + \frac{1}{R} \frac{\hbar}{2e} \dot{\varphi} + C \frac{\hbar}{2e} \ddot{\varphi} \quad (1.5)$$

The last expression is obtained using Eq. (1.3). Here, and throughout this work, $\dot{\varphi} = d\varphi/dt$.

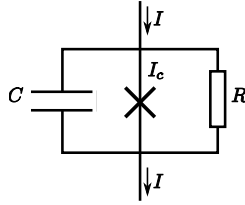


Fig. 1.2: Equivalent circuit of the Josephson junction in the RCSJ model

In order to gain a better understanding of this equation it can be rewritten as

$$E_J \left(\frac{1}{\omega_p^2} \ddot{\varphi} + \frac{1}{\omega_c} \dot{\varphi} \right) + \frac{\partial U}{\partial \varphi} = 0 \quad (1.6)$$

where

$$U(\varphi) = E_J(1 - \cos \varphi - j\varphi) \quad (1.7)$$

is the tilted washboard potential shown in Fig. 1.3 for different values of the normalized bias current $j = I/I_c$. Eq. (1.6) can then be understood as describing the motion of an artificial particle of mass $m = \hbar C/(2e)$ in this potential.

In Eq. (1.6) the Josephson energy $E_J = \Phi_0 I_c/(2\pi)$ and two vital frequencies are introduced.

$$\omega_p = \sqrt{\frac{2eI_c}{\hbar C}} \quad (1.8)$$

$$\omega_c = \frac{2eI_c R}{\hbar} \quad (1.9)$$

The plasma frequency ω_p defines the frequency of small oscillations of the phase particle at the bottom of the potential well for zero bias current. The characteristic frequency ω_c describes the strength of the damping, which is determined by the normal resistance R of the junction. In dimensionless units the damping can be quantified by the reciprocal quality factor $Q = \omega_c/\omega_p = \omega_p RC$ [Tin04].

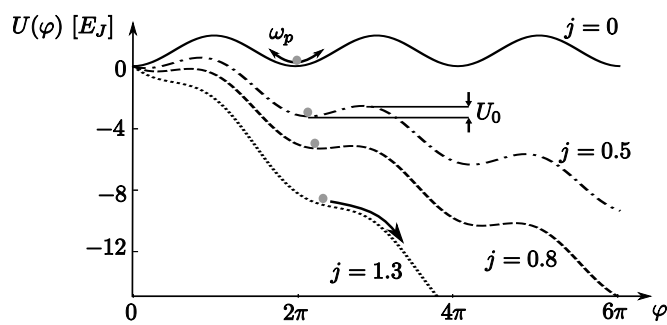


Fig. 1.3: Tilted washboard potential in units of E_J for different normalized bias currents j .

The tilt of the potential due to nonzero bias current changes the plasma frequency and the height of the barrier U_0 that separates one minimum from the other. The dependence of the plasma frequency on the bias current is given by

$$\omega_A(j) = \omega_p(1 - j^2)^{1/4}. \quad (1.10)$$

The exact expression for $U_0(j)$ can be found for example in Ref. [MDC87], but since it is rather awkward to handle, we will mostly use an approximation which is valid for $|1-j|/j \ll 1$.

$$U_0(j, I_c) \approx 2E_J(1-j)^{3/2} \quad (1.11)$$

At zero bias current the phase particle is localized in the minimum at $\varphi = 0$ performing small oscillations with the plasma frequency ω_p . When the current is increased, the potential starts to tilt, thereby decreasing the barrier that separates one minimum from the other. Once the bias current reaches the critical current I_c the minimum is turned into an inflection point and the particle is free to move down the potential. Now, the average velocity switches from $\dot{\varphi} = 0$ to $\dot{\varphi} > 0$, thus creating a finite voltage.

For strong damping, i.e. a small quality factor $Q \ll 1$, the kinetic part of Eq. (1.6) can be neglected, i.e. no kinetic energy can be stored in the system. The transition from $V = 0$ to Ohm's law $V = IR$ is continuous and the current-voltage characteristic is not hysteretic upon decrease of the bias current.

If, however, the junction is underdamped ($Q > 1$), the transition at the critical current when increasing I is discontinuous and the voltage jumps from $V = 0$ to a value near the gap voltage $V_{\text{gap}} = 2\Delta/e$.¹ A further increase in current smoothly interpolates between $V = V_{\text{gap}}$ and Ohm's law. Once the current is reduced, the voltage does not switch back to zero at $I = I_c$, but continues to stay close to $V = V_{\text{gap}}$. This happens because the kinetic energy of the phase particle is large enough to overcome the rising barriers. It only stops when the energy dissipated is greater than the energy gained by the tilt of the potential. Then it is retrapped in one minimum at the retrapping current $I_r \approx 4I_c/(\pi Q)$, where $Q = \omega_p RC$ is the quality factor that characterizes the damping. This creates a hysteretic $I(V)$ -curve as depicted in Fig. 1.4.

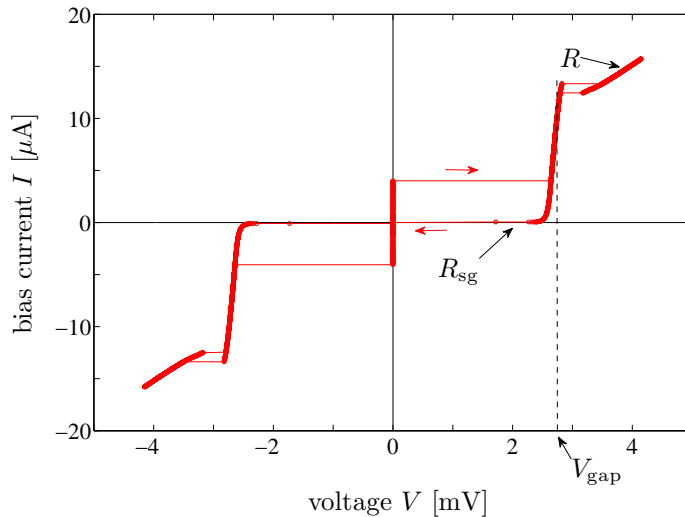


Fig. 1.4: Hysteretic $I(V)$ -curve of an underdamped Josephson junction.²

From the $I(V)$ -curve the junction parameters such as normal resistance R , the subgap resistance R_{sg} and the gap voltage V_{gap} can be extracted. Using the Ambegaokar-Baratoff formula

¹it should be noted that the RCSJ model only shows a jump to $V = RI$

²As a matter of fact, the $I(V)$ -curve displayed was measured for a underdamped dc-SQUID.

[Tin04] for zero temperature the critical current I_c of the junction can then be calculated.

$$I_c R = \frac{\pi}{4} V_{\text{gap}} \quad (1.12)$$

Throughout the rest of this work underdamped junctions will be the center of interest.

1.2.3 Escape Mechanisms

Thermal Activation

The above described situation, where the particle cannot escape before the barrier has completely vanished at $I = I_c$, applies only for a classical particle at zero temperature. For nonzero temperature there is a finite probability that the particle overcomes the barrier via thermal activation (TA) before the barrier has completely vanished at a switching current $I_{\text{sw}} < I_c$. This process is illustrated in Fig. 1.5.

The escape rate of a particle that escapes out of a metastable minimum because of being affected by thermal fluctuations was already determined in 1940 by Kramers [Kra40] for several regimes of damping. In the limit of small damping his result can be approximated [BHL83] to be

$$\Gamma_{\text{TA}} = \frac{\omega_A}{2\pi} \exp \left[-\frac{U_0}{k_B T} \right] \quad (1.13)$$

where ω_A is the current dependent plasma frequency as given in Eq. (1.10). It is also called attempt frequency. The escape rate depends on the ratio between the barrier height U_0 and the thermal energy $k_B T$, where $k_B = 1,38 \cdot 10^{-23}$ J/K is the Boltzmann constant.

Macroscopic Quantum Tunneling

So far, we considered the phase difference across the Josephson junction to be a classical variable, but for a sufficiently small ratio $k_B T / (\hbar \omega_p)$ and weak damping quantum effects become observable.

One of those effects is the escape of the phase particle by tunneling through the barrier of the washboard potential. Since this tunneling process involves not just one single Cooper pair but the phase difference between the two macroscopic wave functions, which therefore also is a macroscopic variable, this effect is called macroscopic quantum tunneling (MQT). It is also depicted in Fig. 1.5.

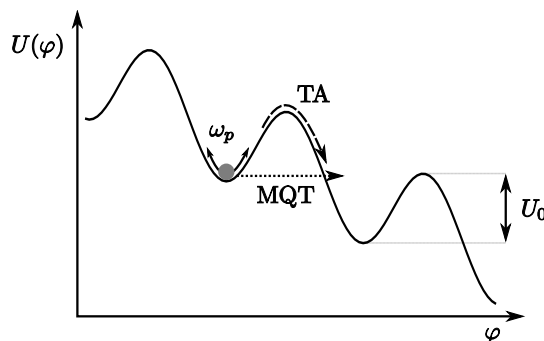


Fig. 1.5: Escape mechanisms out of a local minimum of the washboard potential via thermal activation (dashed) and macroscopic quantum tunneling (dotted).

As long as $U_0 \gg \hbar\omega_p/2$, the Wenzel-Kramer-Brillouin approximation can be applied to calculate the rate for macroscopic quantum tunneling in the case of negligible damping [Lic91].

$$\Gamma_{\text{MQT}} = \frac{\omega_A}{2\pi} \sqrt{\frac{864\pi U_0}{\hbar\omega_A}} \exp\left[-\frac{36U_0}{5\hbar\omega_A}\right] \quad (1.14)$$

Crossover Regime

At high temperatures escape due to thermal activation dominates. As the temperature decreases so does Γ_{TA} while Γ_{MQT} remains constant. Thus, below some crossover temperature T_{cr} macroscopic quantum tunneling becomes the dominating escape mechanism. By comparing the exponents of Eq. (1.14) and Eq. (1.13), the crossover temperature can be approximated to be [Tin04]

$$k_B T_{\text{cr}} \approx \frac{\hbar\omega_A}{2\pi}. \quad (1.15)$$

Phase Diffusion in Underdamped Junctions

Phase diffusion occurs when temperature is comparable to the barrier height $k_B T \approx \Delta U$ of the washboard potential. Additionally, the energy gain due to the tilt of the potential has to be smaller than the energy dissipated between two adjacent maxima. In this case, the phase particle can escape via TA but it will be retrapped in next minimum. From there, it can escape again, is then retrapped and so on.

These subsequent escape and retrapping events cause the particle to move with a slow, stop-and-go like motion down the potential. This creates a small average velocity for the phase particle, resulting in a small average voltage. It can be observed as a small deviation from the superconducting branch in the $I(V)$ -curve.

Phase diffusion in overdamped (nonhysteretic) junctions was understood ([AH69] and [SP70]) long before the explanation for phase diffusion in underdamped (hysteretic) junctions was found [KM90]. As mentioned above, the phase particle is retrapped in the next minimum when the energy gain between two adjacent maxima of the washboard potential is less than the energy dissipated. Within the noise-free RCSJ model for underdamped junctions the equilibrium between energy gained and dissipated is defined by the retrapping current $I_r \approx 4I_c/(\pi Q)$. Thus, phase diffusion in the underdamped regime should not be possible for bias currents above the retrapping current, given that $Q = \text{const}$.

Nonetheless, phase diffusion is observed at currents $I > I_r$. This is possible because the assumption, that the quality factor Q is constant, is not correct in general. In the phase diffusion regime, the phase particle spends most of the time trapped in one of the minima where its motion is defined by oscillations with the plasma frequency $\omega_A(j) \approx \omega_p$ (at small currents). In this frequency range (10–100 GHz) the dissipation of the system is not determined anymore by the constant ohmic resistance $R \sim 1000 \Omega$ of the junction and the resulting quality factor $Q = \omega_p RC$. Instead, the junction sees the impedance of the bias circuit Z_1 which is typically of the order of $Z_1 \sim 100 \Omega$ [Tin04].

Thus, the dissipation $1/Q(\omega)$ for high frequencies is much stronger than for low frequencies. Therefore, the retrapping current $I_r \propto 1/Q(\omega_p)$ for the phase diffusion regime can be considerably higher than the retrapping current out of the running state where $\omega \approx 0$ (cf. Ref. [MK89]).

A nice diagram separating the different regimes of thermal activation, macroscopic tunneling, overdamped and underdamped phase diffusion can be found in Ref. [KNC⁺05].

1.3 The dc-SQUID

A superconducting quantum interference device (SQUID) is realized when one or two junctions are placed in a superconducting loop. For historic reasons they are called rf- or dc-SQUID, respectively. This work is only concerned with two junction SQUIDs and the rf-SQUID will not be considered here.

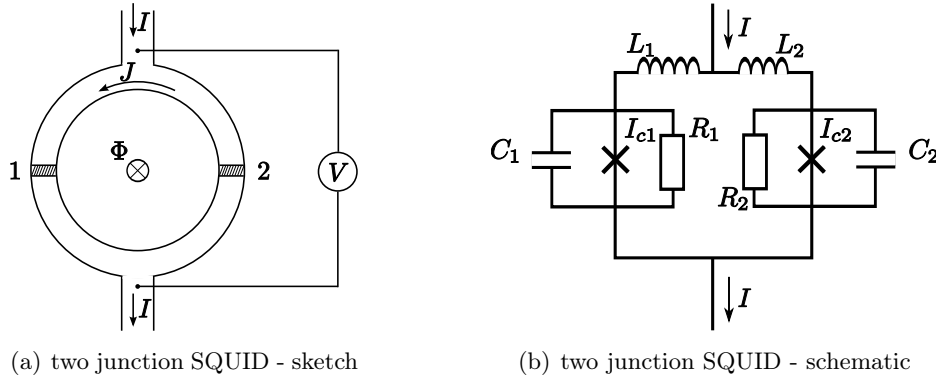


Fig. 1.6: Asymmetric dc-SQUID consisting of a superconducting loop with inductance $L = L_1 + L_2$ threaded by a magnetic flux Φ . The loop is intersected by two junctions with critical current I_{c1} and I_{c2} , intrinsic capacitances C_1 and C_2 and normal resistances R_1 and R_2 .

A sketch and a schematic of a dc-SQUID can be found in Fig. 1.6. The full SQUID is characterized by a total critical current of $2I_c$, a normal resistance R_S and a total loop inductance L . However, those quantities do not have to be distributed equally over the two SQUID arms, as illustrated in Fig. 1.6(b). The asymmetries in inductance and critical current can be characterized by the parameters η and α , respectively. They are defined as

$$L_1 = (1 - \eta) \frac{L}{2} \quad \text{and} \quad L_2 = (1 + \eta) \frac{L}{2}, \quad (1.16)$$

$$I_{c1} = (1 - \alpha) I_c \quad \text{and} \quad I_{c2} = (1 + \alpha) I_c. \quad (1.17)$$

The intrinsic capacitances of the single junctions are proportional to the area of the junctions, as are the critical currents. Therefore, the asymmetry in capacitance can also be described by the parameter α . For the different normal resistances the following equations hold:

$$R_1 = \frac{R}{(1 - \rho)} \quad \text{and} \quad R_2 = \frac{R}{(1 + \rho)} \quad (1.18)$$

where $R = 2R_S$. For simplicity, only the symmetric case $I_{c1} = I_{c2} = I_c$, $L_1 = L_2 = L/2$ and $R_1 = R_2 = R$ will be considered throughout the rest of this chapter.

While both junctions are in the superconducting state the total current I through the SQUID is composed of the current flowing through each junction

$$I = I_c (\sin \varphi_1 + \sin \varphi_2) \quad (1.19)$$

where φ_1 and φ_2 are the phase differences across junction 1 and junction 2, respectively.

In order to obtain the differential equations that describe the dynamic behavior of the two junctions, the RCSJ model is employed once more. Each junction consists again of the ideal junction, a resistor and a capacitor in parallel (cf. Fig. 1.6(b)). The difference to the single

junction is the contribution of the circulating current J , that flows through each junction in addition to half the bias current.

$$\frac{I}{2} + J = I_c \sin \varphi_1 + \frac{1}{R} \frac{\hbar}{2e} \dot{\varphi}_1 + C \frac{\hbar}{2e} \ddot{\varphi}_1 \quad (1.20)$$

$$\frac{I}{2} - J = I_c \sin \varphi_2 + \frac{1}{R} \frac{\hbar}{2e} \dot{\varphi}_2 + C \frac{\hbar}{2e} \ddot{\varphi}_2 \quad (1.21)$$

The total flux Φ through the SQUID loop is composed of the externally applied flux Φ_e and the flux due to a circulating current J .

$$\Phi = \Phi_e - LJ \quad (1.22)$$

Additionally, the flux quantization connects the phase differences across the junctions and the total flux through the loop [Sch97]

$$\varphi_1 - \varphi_2 = \frac{2\pi\Phi}{\Phi_0} \quad (1.23)$$

where Φ_0 is the flux quantum. Using Eqs. (1.22) and (1.23) the equations of motion of the two phase differences φ_1 and φ_2 can be rewritten as (after dividing by I_c)

$$\frac{1}{\omega_p^2} \ddot{\varphi}_1 + \frac{1}{\omega_c} \dot{\varphi}_1 = j - \sin \varphi_1 - \frac{1}{\beta_L} \cdot (\varphi_1 - \varphi_2 - 2\pi \frac{\Phi_e}{\Phi_0}) \quad (1.24)$$

$$\frac{1}{\omega_p^2} \ddot{\varphi}_2 + \frac{1}{\omega_c} \dot{\varphi}_2 = j - \sin \varphi_2 + \frac{1}{\beta_L} \cdot (\varphi_1 - \varphi_2 - 2\pi \frac{\Phi_e}{\Phi_0}). \quad (1.25)$$

They are the same equations as for the single junction (1.6) with an additional coupling term between the two junctions. Here, ω_p and ω_c are as defined in Eq. (1.8) and Eq. (1.9), the coupling term is determined by $\beta_L = 2\pi LI_c/\Phi_0$ and $j = I/(2I_c)$ is the normalized bias current through the SQUID. Physically, a change for example in φ_1 can be understood as the entry of flux into the loop. The induced circulating current decreases the total current through junction 1 while it increases the current through junction 2. This, in turn, changes the phase difference φ_2 across junction 2 (and also φ_1).

As was done already for the single junction, the differential equations (Eqs. (1.24) and (1.25)) can be understood as describing the motion of a particle in a potential. Only in this case the potential is two-dimensional (2D) where a change in φ_1 or φ_2 translates into the motion of the particle in φ_1 - or φ_2 -direction, respectively. By integrating the right part of Eqs. (1.24) and (1.25) with respect to φ_1 and φ_2 this potential $v(\varphi_1, \varphi_2)$ can be obtained to be

$$v(\varphi_1, \varphi_2) = (1 - \cos \varphi_1) + (1 - \cos \varphi_2) - j(\varphi_1 + \varphi_2) + \frac{k}{2}(\varphi_1 - \varphi_2 - 2\pi\phi_e)^2. \quad (1.26)$$

Here, $\phi_e = \Phi_e/\Phi_0$ is the external flux normalized with respect to Φ_0 and $k = 1/\beta_L$ denotes the coupling strength. It should be noted that Eq. (1.26) defines the direction of the flux. Positive flux values increase the current through junction 2, negative values increase the current through junction 1.

In Fig. 1.7 the 2D potential is shown for different coupling strengths $k = 1/\beta_L$. The bias current tilts the potential along the bisectrix $\varphi_1 = \varphi_2$ while the coupling imposes a parabolic deformation perpendicular to the bisectrix. As would be expected, increasing k reduces the influence of the cosine part, until it can be neglected for $k > 1$. Then the dc-SQUID behaves

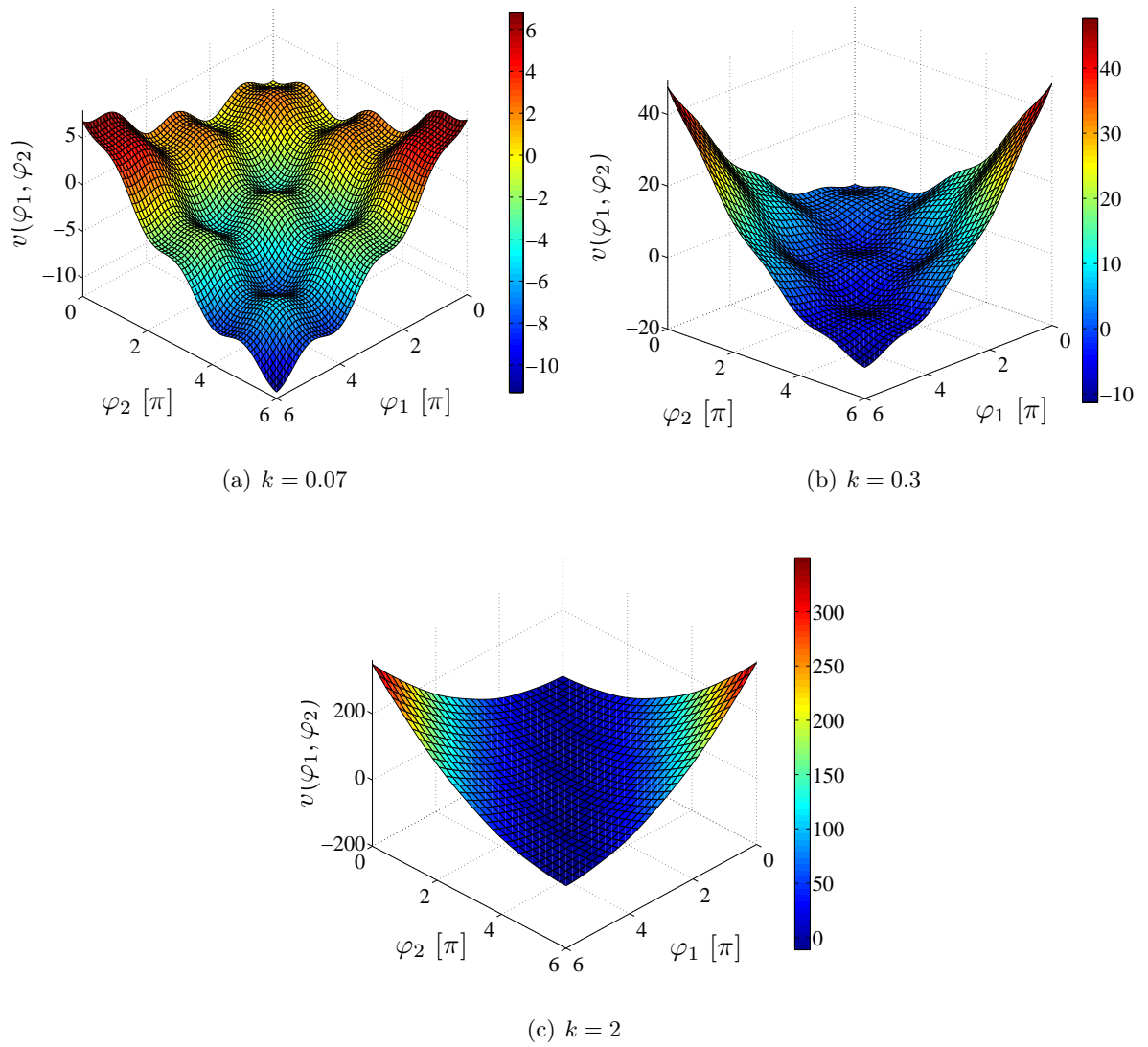


Fig. 1.7: Two-dimensional potential $v(\varphi_1, \varphi_2)$ plotted for $j = 0.3$ and zero external flux for different coupling strengths $k = 1/\beta_L$. Note the different scale for $v(\varphi_1, \varphi_2)$ in the different pictures.

like a single junction whose critical current can be tuned by changing the external magnetic flux.³

Throughout, the rest of this work we are only interested in the weak coupling scenario, i.e. $0 < k < 0.7$, where the cosine terms create wells and hills.

1.3.1 Flux Dependence

Depending on the coupling strength k , at $j = 0$ and $\Phi_e = 0$ there are $N(k)$ different minima in the potential as depicted by 0, 1 and 2 in Fig. 1.9(a). The other minima (e.g. 1' and 2') can be obtained by a trivial translation or reflection along the bisectrix, provided the SQUID is symmetric.

In Fig. 1.9, at $\phi_e = 0$ the barrier separating minimum 0 from minimum 1 is maximal. Upon increasing the flux, this barrier decreases until at some flux value it has completely vanished. During this process minimum 0 changes from being the deepest so-called main minimum to being the second then the third deepest minimum until it turns into an inflection point.

The smaller the barrier is in one direction the less bias current is necessary to remove it. Therefore, to each minimum n a critical current $I_0^{(n)}(\phi_e)$ can be assigned, that also depends on the external magnetic flux.

In Fig. 1.9(a) and 1.9(c), it can be observed that there is an ambiguity in escape direction for the deepest minimum at integer numbers of Φ_0 .

In Fig. 1.8, the effect of external flux and bias current on the potential landscape is illustrated: The external flux leads to a decrease of the barrier height in φ_2 -direction while the barrier in φ_1 -direction is increased (cf. crosses denoted by Z_1 and Z_2 in Fig. 1.8). Sending current through the SQUID tilts the potential along the bisectrix and decreases all barriers in the first quadrant (i.e. $\varphi_1 > 0$ and $\varphi_2 > 0$). However, the saddlepoint in Z_1 is lower than the saddlepoint in Z_2 and therefore vanishes at smaller bias currents (Fig. 1.8(b)). Once the barrier has vanished in one direction, the particle enters the running state.

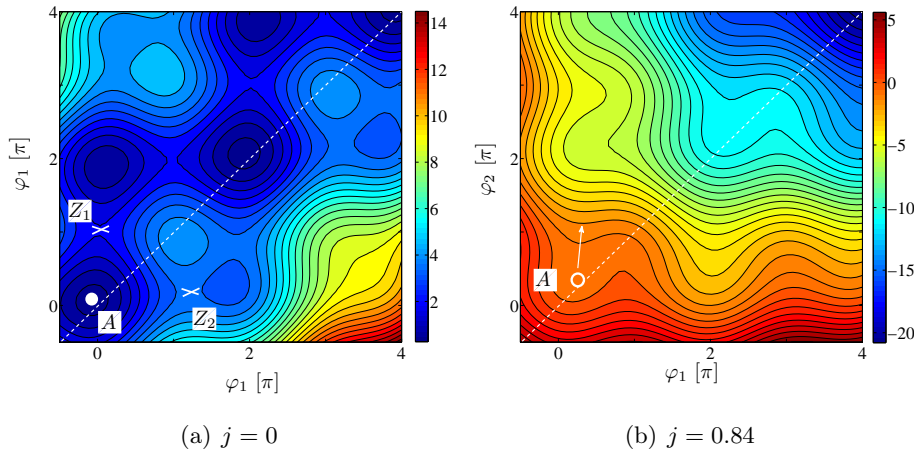


Fig. 1.8: Potential landscape at $\phi_e = 0.4$ for $k = 0.1$. Circles denote the minimum (a) and the inflection point (b). The arrow points into the initial escape direction particle, when entering the running state.

Physically, applying external flux perpendicular to the SQUID loop induces a circulating current in the loop. This additional current increases the total current through one junction,

³except for flux values close to odd numbers of half integer flux values ϕ_e

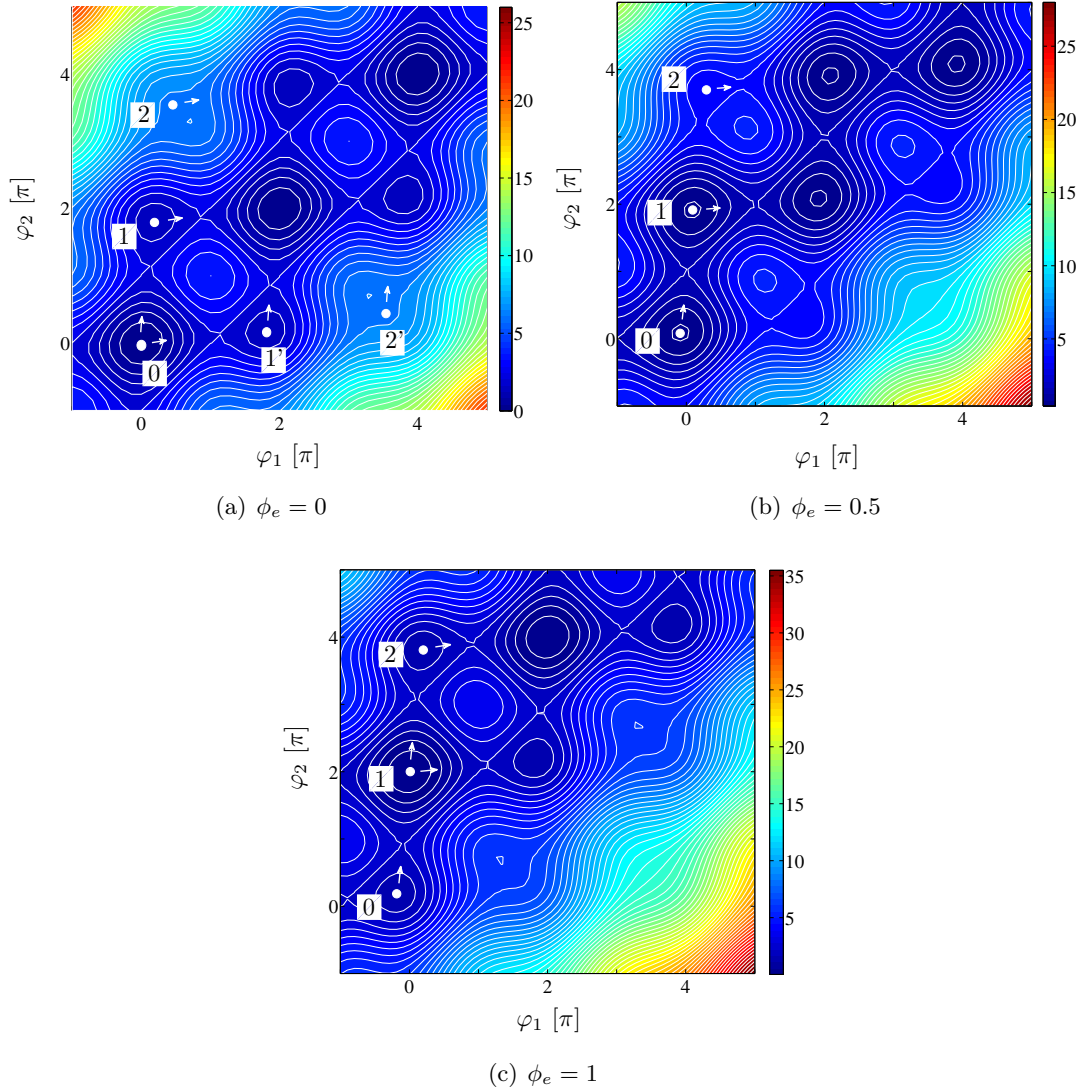


Fig. 1.9: Effect of applied external flux $\phi_e = \Phi_e/\Phi_0$ on the shape of the potential (Eq. (1.26)) for $k = 0.1$. All potentials are shown for $j = 0$. The white solid circles illustrate the different minima. The numbers denoting the different minima correspond to the numbers in Fig 1.10. Arrows point into the possible directions of escape once the bias current is increased in positive direction. (a) At $\phi_e = 0$ the minimum 0 is the deepest, the currents through both junctions are equal and the critical current of the SQUID is $I_0(0) = 2I_c$. (b) The barrier between minimum 0 and 1 is decreased and therefore vanishes already at a critical current $I_0(\phi_e) < 2I_c$. (c) At $\Phi_e = \Phi_0$ minimum 1 is the deepest minimum and the situation of an escape out of this minimum is the same as for minimum 0 in (a).

e.g. junction 2, while decreasing it through junction 1. As a result, the critical current I_c for junction 2 is reached before the total current sent through the SQUID is $I = 2I_c$.

In order to obtain the critical current for each flux value quantitatively, the critical point where the potential barrier vanishes has to be found. Therefore, a simple coordinate transformation $x = (\varphi_1 + \varphi_2)/2$ and $y = (\varphi_1 - \varphi_2)/2$ makes the potential easier to handle. As it is needed in Chapter 5 the asymmetry parameters α and η are included. The coordinate transformed potential then looks like

$$U(x, y) = 2E_J[-jx - \cos x \sin x - \alpha \sin x \sin y - \eta jy + k(y - \pi\phi_e)^2]. \quad (1.27)$$

For the new coordinates, the tilt of the potential due to the bias current is along the x -axis, while the curvature of the potential resulting from the coupling between the junctions is in y -direction.

At the critical point (x_c, y_c) the minimum (A) merges with the saddlepoint (Z_1). The conditions defining a minimum in a 2D potential $U(x, y)$ are given by

$$U_x = 0 \Rightarrow \sin x \cos y - \alpha \cos x \sin y = j, \quad (1.28)$$

$$U_y = 0 \Rightarrow \cos x \sin y - \alpha \sin x \cos y - \eta j + 2k(y - \pi\phi_e) = 0. \quad (1.29)$$

Here and in the following, $U_x = \partial U / \partial x$. To find the critical current for any minimum, the properties of the critical point have to be defined: The curvature of the potential has to vanish in the direction of escape, while the curvature remains positive in the perpendicular direction. The first condition is fulfilled when

$$\begin{aligned} U_{xx}U_{yy} - (U_{xy})^2 &= 0 \\ \Rightarrow (\cos x \cos y + \alpha \sin x \sin y)(\cos x \cos y + \alpha \sin x \sin y + 2k) &= \\ &(\sin x \sin y + \alpha \cos x \cos y)^2. \end{aligned} \quad (1.30)$$

The second condition corresponds to $U_{xx} + U_{yy} \geq 0$, which can be used to test the solutions for j_0 , x_c and y_c obtained when solving Eqs. (1.28)-(1.30) for fixed values of α , η and ϕ_e .

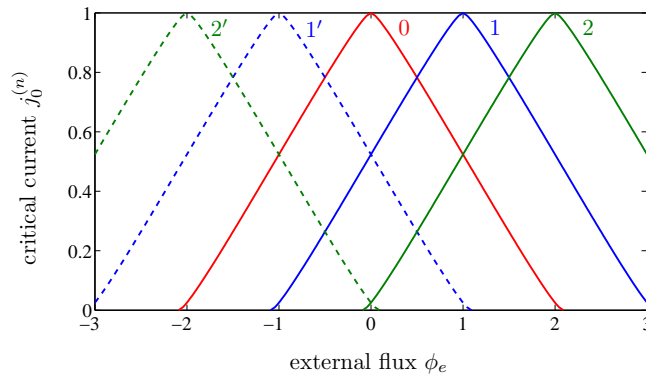


Fig. 1.10: Critical current vs. external flux dependence $j_0^{(n)}(\phi_e)$ for $k = 0.1$ with $\alpha = \eta = 0$. Red, blue and green solid lines correspond to minimum 0, 1 and 2 respectively, while the dashed blue and green lines correspond to the mirrored minima 1' and 2'.

In Fig. 1.10, the solutions $j_0^{(n)}(\phi_e)$ for $\alpha = \eta = 0$ are plotted for several minima n . They represent the dependence of the critical current on external flux. The numbers in the plot correspond to the numbers of the minima in Fig. 1.9(a).

The number $N(k)$ of different minima that are present at the same flux value can be extracted from the number of curves that exist at one fixed flux value. $N(k)$ depends on the coupling constant. Decreasing k creates more different metastable minima in the potential and also decreases the slope of the critical current vs. external flux curve depicted in Fig. 1.10. Increasing k leads to larger slopes and less different minima.

1.3.2 Escape Mechanisms in Two Dimensions

As for the single junction, thermal fluctuations and quantum tunneling decrease the switching current I_{sw} of the SQUID compared to its critical value $I_0^{(n)}(\phi_e)$ (in Appendix C a nomenclature for the different currents can be found). The same principles of escape out of a metastable minimum as mentioned earlier for the single junction apply. However, the fact that the particle can move in two dimensions and that the height of the barrier depends on the escape direction, influences the escape rates.

At zero applied bias current the particle is localized in one of the available wells. For now, let us assume that the particle is trapped in the well close to $(\varphi_1, \varphi_2) = (0, 0)$ as depicted with point A in Fig. 1.11(a). In order to avoid the ambiguity in escape direction for $\phi_e = 0$ the potential is plotted for $\phi_e = 0.2$. At zero bias current the barrier is lowest at the saddlepoint denoted by Z . Upon increase of the bias current, all barriers in the first quadrant decrease and when escaping the phase particle follows the optimal trajectory where it has to overcome the smallest barrier.

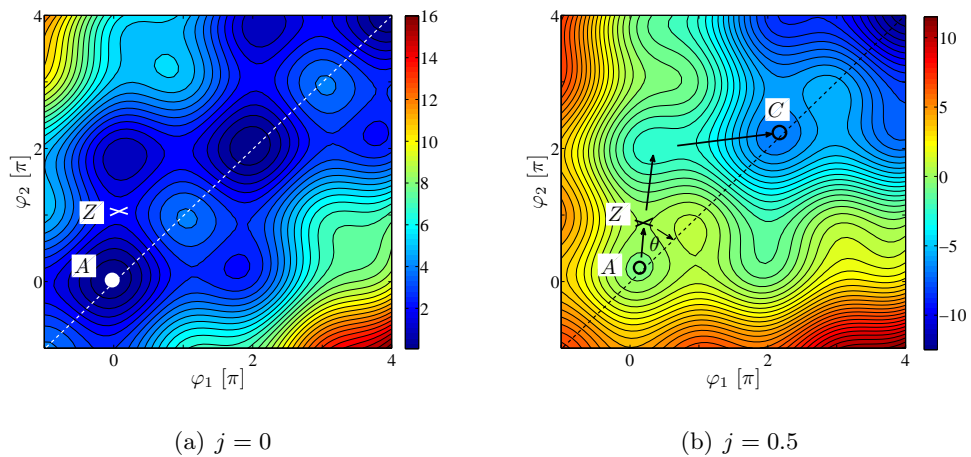


Fig. 1.11: Escape mechanisms illustrated for $\phi_e = 0.2$ and $k = 0.1$.

This optimal trajectory is illustrated in Fig. 1.11. Starting in A , the particle will overcome the barrier in Z (see Fig. 1.11(b)) and then follow the steepest decline in the potential to the next minimum in C . For underdamped junctions, the kinetic energy of the particle is large enough to allow it to overcome the next barrier in φ_1 -direction. Then the coupling parabola forces it back to the bisectrix. Due to this mechanism the phase particle follows a trajectory that oscillates around $\varphi_1 = \varphi_2$, comparable to a sailing boat moving against the wind. In order to accelerate the boat has to deviate from its course and move via beating in the favored direction.

In [LSTU⁺92] Valérie Lefevre-Seguin *et al.* developed an approach to calculate the rate of thermal escape in two dimensions. Therefore, the new complexity of the two dimensional system is included in the single junction escape rate.

The defining quantity for the thermal escape rate is the ratio of barrier height to temperature $\tilde{U}_0/(k_B T)$. Since the height of the barrier is not equal in all direction, the point with the smallest barrier has to be found. Assuming switching currents that are close to the critical current of the considered minimum n (i.e. $I_0^{(n)}(\phi_e)$), the least elevated point in the barrier is close to the critical point (x_c, y_c) defined earlier. The potential barrier height \tilde{U}_0 can then be approximated with a third order expansion of the potential $U(x, y)$ around this critical point and the escape trajectory comes close to being a straight line with an angle θ to the x -axis.

The barrier height is given by

$$\tilde{U}_0(j) = \sqrt{\cos^3(\theta) \frac{j_0}{u_3}} U_0(j/j_0, I_0) \quad (1.31)$$

where θ is the angle between x -axis and escape direction and u_3 is the third derivative of $U(x, y)$ in the critical point (x_c, y_c) and can be found in Ref. [LSTU⁺92]. $U_0(j, I_c)$ is the one-dimensional (1D) barrier height given by Eq.(1.11) and $j_0 = I_0/(2I_c)$ is the normalized critical current. It is also listed in table C.1 Appendix C.

Additionally, the attempt frequency ω_A is influenced by the two dimensionality of the system

$$\tilde{\omega}_p(j) = \omega_A(j/j_0) \left(\frac{u_3 \cos(\theta)}{j_0} \right)^{1/4}. \quad (1.32)$$

$\omega_A(j)$ is the 1D attempt frequency given by Eq. (1.10).

Eqs. (1.31) and (1.32) replace the respective 1D quantities in the 1D escape rates, i.e Eqs. (1.13) and (1.14). Although in Ref. [LSTU⁺92] only the TA rate was considered, their approach was also used in Ref. [LYZ⁺02] to get an expression for the MQT rate:

$$\Gamma_{\text{TA}} = \frac{\tilde{\omega}_p(j)}{2\pi} \frac{\omega_{w\perp}}{\omega_{s\perp}} \exp \left[-\frac{\tilde{U}_0(j)}{k_B T} \right]; \quad (1.33)$$

$$\Gamma_{\text{MQT}} = \frac{\tilde{\omega}_p(j)}{2\pi} \frac{\omega_{w\perp}}{\omega_{s\perp}} \sqrt{\frac{864\pi\tilde{U}_0(j)}{\hbar\tilde{\omega}_p}} \exp \left[-\frac{36}{5} \frac{\tilde{U}_0(j)}{\hbar\tilde{\omega}_p(j)} \right]. \quad (1.34)$$

The ratio $\omega_{w\perp}/\omega_{s\perp}$ represents the ratio between the frequencies of oscillations perpendicular to the escape direction in the well ($\omega_{w\perp}$) and in the saddlepoint ($\omega_{s\perp}$). For weakly coupled SQUIDS, the ratio $\omega_{w\perp}/\omega_{s\perp}$ is close to unity except when $I_0(\phi_e)$ approaches the maximum critical value $2I_c$ where the escape direction is not defined unambiguously. More details for this case where $j_0(\phi_e) \approx 1$ can be found in Ref. [LSTU⁺92].

The thermal or tunneling rates are obtained by first solving Eqs. (1.28)-(1.30) for the specific flux and asymmetry values to determine j_0 , x_c , y_c and θ . These values are used to calculate the barrier height \tilde{U}_0 and the attempt frequency $\tilde{\omega}_p$. These quantities then are inserted into Eqs(1.33) and (1.34) to calculate the respective escape rates.

Chapter 2

The Theory of the Münchhausen Effect

The idea of the Münchhausen effect was introduced by V. B. Geshkenbein, A.U. Thomann and G. Blatter in Ref. [TGB09]. They suggested that the coupling of one classical and one quantum mechanical degree of freedom can be realized in an asymmetric dc-SQUID. Since such a coupled system can escape from a metastable state seemingly on its own account, this behavior was called “Münchhausen” effect, after Baron Münchhausen who claimed to have rescued himself out of a swamp by pulling at his own hair.

2.1 Basic Idea

The idea for the experimental realization of the Münchhausen effect is to take a dc-SQUID with two small identical junctions. Using again the analogy of a particle in a 2D potential, the intrinsic capacitance of the junction can be considered as the mass equivalent $m = \hbar C / (2e)$. Thus, if its capacitance is small enough, the junction exhibits quantum mechanical behavior. In order to make one junction of the SQUID behave classically, its “mass” is artificially increased by shunting it with a large capacitor C_0 close to the junction as shown in Fig. 2.1. Both junctions

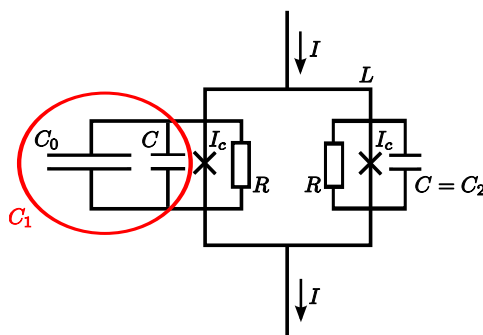


Fig. 2.1: Asymmetric dc-SQUID.

have the same critical current I_c and the same normal resistance R but different capacitances $C_1 \gg C_2$. Throughout the rest of this thesis the “heavy”, classical junction will be referred to as junction 1 and the phase difference across it will be denoted as φ_1 . The “lighter”, supposedly quantum mechanical junction will be named junction 2 with the corresponding phase difference φ_2 .

The same equations of motion as for the symmetric SQUID (cf. Sec. 1.3) can be applied.

$$\frac{1}{\omega_{p1}^2} \ddot{\varphi}_1 + \frac{1}{\omega_c} \dot{\varphi}_1 = j - \sin \varphi_1 - k \cdot (\varphi_1 - \varphi_2 - 2\pi \frac{\Phi_{\text{ext}}}{\Phi_0}) \quad (2.1)$$

$$\frac{1}{\omega_{p2}^2} \ddot{\varphi}_2 + \frac{1}{\omega_c} \dot{\varphi}_2 = j - \sin \varphi_2 + k \cdot (\varphi_1 - \varphi_2 - 2\pi \frac{\Phi_{\text{ext}}}{\Phi_0}) \quad (2.2)$$

where ω_{p1} and ω_{p2} are the plasma frequencies of junction 1 and junction 2, respectively. ω_c is again the reciprocal damping parameter, $j = I/(2I_c)$ denotes the normalized bias current sent through the SQUID and $k = 1/\beta_L = \Phi_0/(2\pi I_c L)$ is the coupling strength.

In the particle-in-a-2D-potential picture the particle behaves classically in φ_1 - and quantum mechanically in φ_2 -direction.

2.2 Strong Damping and Zero Temperature

The basic behavior of the system can be best understood in the case of zero temperature and for overdamped junctions. Then, the second derivatives in the equations of motion (Eqs. (2.1) and (2.2)) can be neglected and only the potential energy as given in Eq. (1.26) defines the behavior of the system.

At zero bias current the particle resides in the minimum at $(\varphi_1, \varphi_2) = (0, 0)$ (point *A* in Fig. 2.2). Once the bias current is increased, there are two scenarios, each starting with the tunneling in φ_2 -direction, that can lead to an escape. They both are illustrated in Fig. 2.2.

Escape triggered by tunneling (Fig. 2.2(a) and 2.2(b)). The particle can tunnel in φ_2 -direction as soon as the bias current tilts the potential $v(\varphi_1, \varphi_2)$ enough to lower the next adjacent minimum in φ_2 -direction (denoted by *B*) below minimum *A*. The bias current necessary to enable quantum tunneling in φ_2 -direction depends on the coupling constant k because k determines the curvature of the potential and thus the energy difference between the bottom of the two minima. The critical line $k_{c,1}^+(j)$ that connects the bias current necessary to energetically align the two minima with the corresponding coupling constant is calculated in Ref. [TGB09]:

$$k_{c,1}^+(j) = \frac{j}{\pi - \arcsin j}. \quad (2.3)$$

As can be seen in Fig. 2.2(b), once the particle has tunneled to $(\varphi_1, \varphi_2) \approx (0, 2\pi)$ (point *B* in 2.2(a)), there is no longer a barrier blocking the motion in φ_1 -direction. The particle moves to the next minimum close to $(2\pi, 2\pi)$ and the process repeats itself.

Escape triggered by increasing the bias current (Fig. 2.2(c)-2.2(e)). If the coupling k between the two junctions is too small, the particle can tunnel to minimum *B* but there the potential barrier in φ_1 -direction has not yet vanished completely (cf. Fig. 2.2(d)). A further increase in bias current is necessary to remove this barrier. The $k(j)$ -dependence of this process was also calculated in Ref. [TGB09]:

$$k_{c,1}^-(j) = \frac{1 - j}{\frac{3}{2}\pi + \arcsin(2j - 1)}. \quad (2.4)$$

When k is decreased even further, at some point the second minimum in φ_2 -direction becomes accessible via MQT. Thus, the particle tunnels first from *A* to *B* but before the barrier in φ_1 -direction vanishes for minimum *B*, the particle can tunnel to the next adjacent minimum in φ_2 -direction. There, no barrier blocks the motion in φ_1 -direction and the particle enters the running state. Thus, continuing to decrease the coupling does not change the quality of the two different escape scenarios but only the minimum that has to be considered. The corresponding equations are given by Eqs. (2.5) and (2.6). The $k(j)$ -dependence corresponding to the ability of the system to tunnel to the n -th minimum in φ_2 -direction is given by

$$k_{c,n}^+(j) = \frac{j}{(2n - 1)\pi - \arcsin j}. \quad (2.5)$$

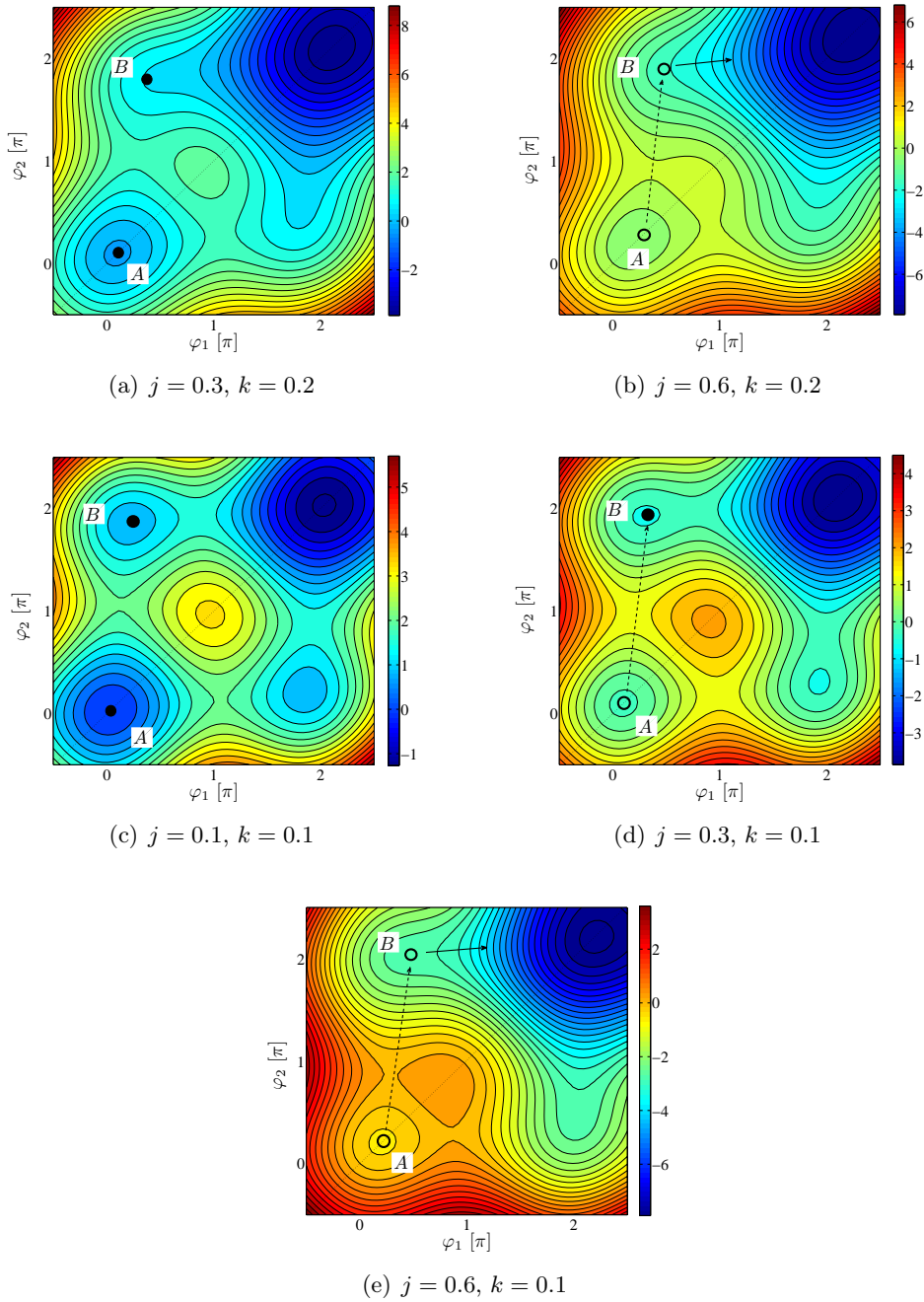


Fig. 2.2: Potential energy landscape. (a) and (b) illustrate the situation for $k = 0.2$ where the tunneling of junction 2 leads directly to the escape, while (c)-(e) show the case for $k = 0.1$, where, after the tunneling in φ_2 -direction, it is necessary to fully remove the barrier in φ_1 -direction by increasing the bias current. Solid circles depict minima that the particle cannot leave. Empty circles show minima, that can be left either via MQT in φ_2 -direction (dashed arrows) or because the minimum turns unstable in φ_1 -direction (solid arrows).

The line describing the removal of the barrier between the minimum at $(\varphi_1, \varphi_2) \approx (0, 2\pi n)$ and the adjacent minimum in φ_1 -direction by increasing the bias current is given by

$$k_{c,n}^-(j) = \frac{1-j}{(2n - \frac{1}{2})\pi + \arcsin(2j-1)}. \quad (2.6)$$

$k_{c,n}^\pm(j)$ defines implicitly critical currents $j_{c,n}^\pm$ at which the particle can tunnel or the barrier has vanished. Those currents are also listed in table C.1 in Appendix C.

In Fig. 2.3, the $k_{c,n}^\pm(j)$ -curves are plotted for several n . Curves with positive slope represent currents at which the particle can tunnel to the n -th minimum in φ_2 -direction. Curves with negative slope depict the current at which the barrier of the n -th minimum has vanished in φ_2 -direction. The effective critical current $j_c^{\text{eff}}(k)$ (solid line in Fig. 2.3) corresponds to the current at which the particle enters the running state, i.e. is able to leave every minimum on its way down the potential. It is composed partially of $j_{c,n}^+$ and partially $j_{c,n}^-$ depending on which process triggers the escape.

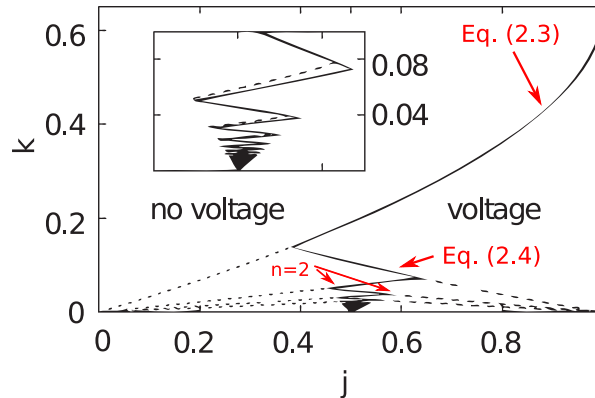


Fig. 2.3: Phase diagram for the Münchhausen effect as a function of the normalized bias current j and the coupling constant k . Lines with positive slope (dotted/solid) correspond to the tunneling of the quantum junction while lines with negative slope (dashed/solid) indicate the current at which the minimum of the classical junction turns into an inflection point. The solid line represents the effective critical current j_c^{eff} , when the particle can move down the potential. The inset shows $j_c^{\text{eff}}(k)$ for smaller k -values. The dashed line gives a more accurate numerical result, the solid line is a simplifying analytical approximation. The phase diagram is taken out of Ref. [TGB09].

Physically, the tunneling process can be understood as the entry of one flux quantum into the SQUID loop. This creates a circulating screening current in the loop, that decreases the current through junction 2 and increases the current flowing through junction 1. The potential for φ_1 is therefore tilted stronger, resulting in the decrease or even removal of the barrier. Once the particle advances also in φ_1 -direction the flux quantum exits the loop again.

2.3 Flux Dependence

Experimentally, the phase diagram in Fig. 2.3 can be probed only along horizontal ($k = \text{const.}$) lines since for one SQUID the critical current of the single junction I_c and the loop inductance L are fixed design parameters. Thus, many SQUIDs would have to be designed and measured to test the phase diagram in Fig. 2.3 satisfactorily.

However, in Ref. [TGB09] a way to circumvent this problem was found by including an externally applied flux into the discussion. As explained in Section 1.3.1, applying external magnetic flux supports the motion of the particle either in φ_1 - or in φ_2 -direction. Additionally, it reduces the critical current.

In order to find the flux dependence of the effective critical current of the Münchhausen effect, the same conditions for tunneling in φ_2 - and moving classically in φ_1 -direction, as mentioned previously, apply: For tunneling, the present minimum and the adjacent minimum in φ_2 -direction have to be energetically aligned and for the classical escape in φ_1 -direction the barrier has to vanish. Again k_n^+ and k_n^- were calculated in Ref. [TGB09].

$$k_n^+ \approx \frac{j}{(2n-1) - \arcsin(j) + 2\pi\phi_e} \quad (2.7)$$

$$k_n^- \approx \frac{1-j}{(2n-\frac{1}{2})\pi + \arcsin(2j-1) + 2\pi\phi_e} \quad (2.8)$$

For fixed k , Eqs. (2.8) and (2.7) can be solved for ϕ_e and define implicitly $j_{c,n}^\pm(\phi_e)$. In fact, if k is fixed, Eq. (2.8) is an approximation of the classical critical current vs. flux dependence $j_0^{(n)}(\phi_e)$, that was already mentioned in Section 1.3.1. In Fig. 2.4, the critical current lines $j_n^+(\phi_e)$ (red dashed) and $j_n^-(\phi_e)$ (solid blue) are plotted for $k = 0.1$. The colored arrows depict the effective critical current $j_c^{\text{eff}}(\phi_e)$ at which the system switches to the finite voltage state depending on the external flux. Without the Münchhausen effect the critical current would follow the solid blue $n = 0$ curve.

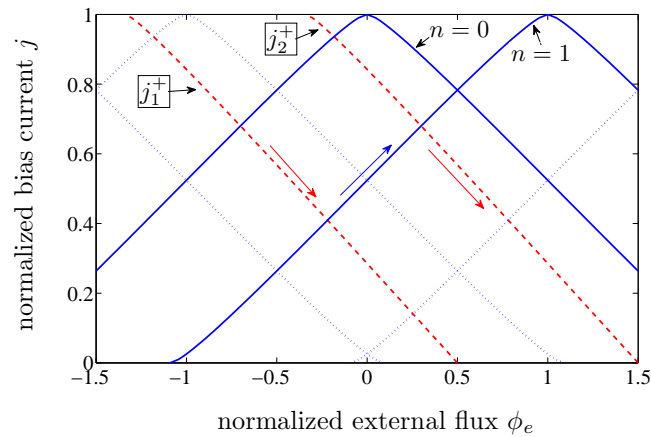


Fig. 2.4: Flux dependence of the normalized critical current lines $j = I/(2I_c)$ for $k = 0.1$. The blue lines give the classical theory $j_0^{(n)}(\phi_e)$, the solid blue lines correspond to lines considered in the text, while the dotted blue lines are included only for completeness. The dashed red lines show the critical current lines $j_n^+(\phi_e)$ ($n = 1, 2$) of the Münchhausen effect, when tunneling in φ_2 -direction becomes possible. The colored arrows denote the effective critical current of the SQUID according to the Münchhausen theory.

At zero flux, upon increasing the bias current, the system first reaches the critical line j_1^+ (dashed red) where the particle can tunnel in φ_2 -direction. Now, it finds itself in the minimum close to $(0, 2\pi)$. The critical current of this minimum is defined by the $n = 1$ classical flux line (solid blue). When the bias current is increased further, the particle will escape in φ_1 -direction

once the $n = 1$ line is reached. A different situation occurs for example at $\phi_e = -0.5$. When increasing the bias current the $n = 1$ line is crossed while the particle is still localized in the minimum close to $(0, 0)$ and before tunneling is possible. Thus, once the particle can tunnel to the minimum close to $(0, 2\pi)$, this minimum is already unstable in φ_1 -direction.

The reduced effective critical current and the shift in the position of maximum and minimum of the critical current vs. external flux dependence (cf. Fig. 2.4) can be used in the experimental search for the Münchhausen effect.

Chapter 3

Numerical Evaluation of the Asymmetric dc-SQUID

In order to understand the behavior of the system in more detail and to include the effects of nonzero temperature, numerical simulations were performed. The results will be presented together with the experimental ones in Chapter 5.

3.1 The Heun Method

A set of stochastic equations of motion can be written as [GSH88]

$$\dot{\vec{x}} = \vec{f}(\vec{x}) + \sigma(\vec{x})\vec{\eta} \quad (3.1)$$

where \vec{f} is called the drift term and describes the deterministic time evolution of the system and η defines the Langevin form of the noise. In the following only white noise will be considered. This yields for η :

$$\langle \eta_i(t) \rangle = 0, \quad (3.2)$$

$$\langle \eta_i(t)\eta_j(t') \rangle = \delta_{ij}\delta(t-t'). \quad (3.3)$$

The diffusion due to the noise is determined by σ , which in general is a $n \times n$ matrix (n being the dimension of \vec{x}). In the case of white noise, it does not depend on the variable \vec{x} and its off-diagonal terms are zero.

For $\vec{\eta} = 0$, the equations of motion are deterministic. Knowing \vec{x} at $t = 0$, \vec{x} at $t = h$ can be obtained by using a Taylor expansion. Depending on the order of the resulting polynomial in h , an arbitrary accuracy is possible. As shown in Ref. [GSH88], the expansion in h for stochastic differential equations contains nonlinear functionals of the white noise when including terms of the order of h^2 . Their behavior upon integration cannot be predicted and may decrease the accuracy of the result. Thus, restricted to low order polynomials, the integration has to be performed using small time steps and a simple, i.e. fast way of calculating $\vec{x}(h)$ has to be chosen.

The Heun Method [GSH88] is a such simple method. It corresponds to a second order Runge-Kutta algorithm but includes a white noise term. Knowing the variable $\vec{x}(t_0)$ at the start time t_0 , its value at time $t = t_0 + h$ is obtained by

$$x^i(h) = x^i(t_0) + \frac{1}{2} \left[f^i(\vec{x}(t_0)) + f^i(\vec{\xi}(h)) \right] h + \sigma^i W_i(h) \quad (3.4)$$

with

$$\vec{\xi}(h) = \vec{x}(0) + \vec{f}(\vec{x}(0))h + \sigma^i W_i(h). \quad (3.5)$$

Here, x^i , f^i and $\sigma^i = \sigma^{ii}$ are the variables defined above and depend on the system that shall be described. W_i are Gaussian-distributed random numbers.

3.2 Application to the Asymmetric dc-SQUID

In the case of the asymmetric dc-SQUID the simulation integrates the two coupled equations of motion (Eqs. (1.24) and (1.25)) and includes temperature as white noise. Using the Heun Method they have to be transformed to be differential equations of first order. The system is then described by

$$\vec{x} = \begin{pmatrix} x_1 \\ x_2 \\ x_3 \\ x_4 \end{pmatrix} = \begin{pmatrix} \varphi_1 \\ \varphi_2 \\ \dot{\varphi}_1 \\ \dot{\varphi}_2 \end{pmatrix} \quad (3.6)$$

where φ_1 and φ_2 are the phase differences across junction 1 and junction 2, respectively. As a reminder, junction 1 is shunted with a large capacitor, while junction 2 is unshunted, therefore $\omega_{p1} < \omega_{p2}$.

The drift term $\vec{f}(\vec{x})$ is given by

$$\vec{f}(\vec{x}) = \begin{pmatrix} x_3 \\ x_4 \\ \omega_{p1}^2 \left(-\sin x_1 + j - k(x_1 - x_2) - \frac{1}{\omega_c} x_3 \right) \\ \omega_{p2}^2 \left(-\sin x_2 + j + k(x_1 - x_2) - \frac{1}{\omega_c} x_4 \right) \end{pmatrix}. \quad (3.7)$$

The effect of finite temperature on the equations of motion can be taken into account by adding a fluctuation current i_F with white noise properties (cf. Ref. [Lic91]).

$$\langle i_{F,i}(t) i_{F,j}(t + \Delta t) \rangle = 2 \frac{k_B T}{E_J} \frac{1}{\omega_c} \delta(\Delta t) \delta_{ij} \quad (3.8)$$

Applying this to the numerical method and translating it into σ and η yields $\sigma_3 = \sigma_4 = 2k_B T / (E_J \omega_c) = \tilde{\sigma}$ and zero for all other components of σ .

Thus, Eq. (3.1) applied to the asymmetric SQUID becomes

$$\dot{\vec{x}} = \begin{pmatrix} x_3 \\ x_4 \\ \omega_{p1}^2 \left(-\sin x_1 + j - k(x_1 - x_2) - \frac{1}{\omega_c} x_3 \right) \\ \omega_{p2}^2 \left(-\sin x_2 + j + k(x_1 - x_2) - \frac{1}{\omega_c} x_4 \right) \end{pmatrix} + \begin{pmatrix} 0 \\ 0 \\ \omega_{p1}^2 \tilde{\sigma} \eta_3 \\ \omega_{p2}^2 \tilde{\sigma} \eta_4 \end{pmatrix}. \quad (3.9)$$

When numerically integrating the system, the Gaussian distributed random numbers W_i are generated within the simulation. Therefore, a uniform random number generator and a transformation method from Ref. [num07], that converts the uniform number stream into a Gaussian distributed one, are used.

In the simulation, the time is additionally normalized to dimensionless units $\tau = t\omega_p$ where $\omega_p = \omega_{p1}\omega_{p2}/(\omega_{p1} + \omega_{p2})$. The integration is then performed in normalized time steps of $h = 0.02$. The size of the time steps should be as small as possible. However, in order to simulate the experiment, the current j has to be increased with a given ramping rate. The time scale of this ramping rate is much larger than the time scale of the plasma oscillations and a compromise between step size and run time of the simulation had to be found.

The simulation was used to examine the time evolution of the system as well as its escape properties. For the latter, the integration was repeated ~ 200 times and the escape statistics were recorded. In Chapter 5, simulated and measured results are presented and compared.

Chapter 4

Experimental Realization and Setup

In this chapter the design of the different SQUIDs is presented and the experimental setup is introduced. Furthermore, the procedure and the results of current ramp measurements, that were used to experimentally test the SQUIDs, are discussed.

4.1 Chip Design

Four different dc-SQUIDs with suitable coupling constants and critical currents were designed by Alexey Feofanov. Four chips, each containing all four different SQUIDs, were fabricated in the Physikalisch-Technische Bundesanstalt (PTB) Braunschweig by Ralf Dolata and Brigitte Mackrodt in a Nb/AlO_x/Nb trilayer process using electron beam lithography, dry etching, anodization and planarization by chemical-mechanical polishing [DSZN05] to produce Josephson junctions with dimensions below 100 nm × 100 nm. An image of one full chip can be found in Appendix A.

Nb has a superconducting gap energy of $\Delta_{\text{Nb}} = 1.5$ meV and the critical current density of 1.4 kA/cm² of the wafer was measured very precisely on large area junctions by Kirill Fedorov. The SQUIDs were designed with parameter values as given in Tab. 4.1; the large capacitor that increases the capacitance of junction 1 always has a capacitance of $C_0 = 1$ pF, while junction 2 is not capacitively shunted.

	SQUID S1	SQUID S2	SQUID S3	SQUID S4
junction size $\mu\text{m} \times \mu\text{m}$	0.2×0.2	0.2×0.2	0.5×0.5	0.5×0.5
I_c [μA]	0.56	0.56	3.5	3.5
C [fF]	3	3	15	15
L [nH]	4	8	0.25	0.7
$\omega_{p1}/(2\pi)$ [GHz]	6.5	6.5	16	16
$\omega_{p2}/(2\pi)$ [GHz]	119	119	133	133

Table 4.1: Design parameters for the different SQUIDs. I_c is the critical current and C is the intrinsic capacitance of the single junction. L denotes the inductance of the SQUID loop. The plasma frequencies ω_{p1} and ω_{p2} are the plasma frequencies of the shunted and the unshunted junction, respectively.

Throughout the rest of this work the different SQUIDs 1, 2, 3 and 4 will be referred to as S1, S2, S3 and S4, respectively.

In Fig. 4.1 optical microscope images of S4 are shown. The middle image shows the full dc-SQUID; the gradiometric 8-formed shape of the loop is used to minimize the influence of unwanted external flux. The image on the left shows a zoom to the unshunted junction. In the right image the capacitively shunted junction including the capacitor can be seen. The flux lines are used to couple external flux into the SQUID loop. Since the size of the loop is the

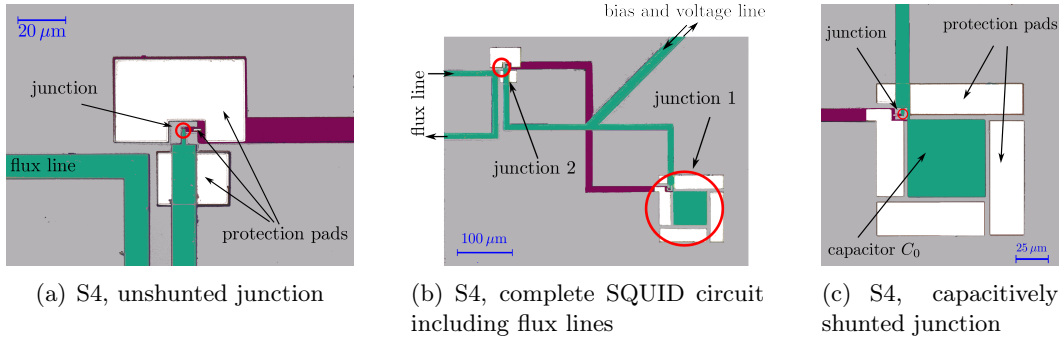


Fig. 4.1: Light microscope images taken of S4. For better visibility the colors of the images were changed. The substrate is shown in grey, the lower Nb layer is red, the upper layer green. The protection pads, which are required to protect the junctions during the chemical-mechanical polishing process during fabrication, are colored white.

most considerable difference between the SQUIDs, the other SQUIDs are shown only as full circuits in Appendix A. The requirement of weak coupling $k < 1$ and small junctions demands the fabrication of large loops in order to create large inductances $L \propto A$ (A being the area of the loop).

4.2 Experimental Setup

All measurements were performed using a sorption pumped ^3He -cryostat HelioxVL made by Oxford Instruments with a base temperature of $T_b \approx 300$ mK. The wiring consists of 24 dc lines without filtering and the wires for the three thermometers installed in the cryostat. For some of the measurements current dividers were installed on the sample holder.

An image of the sample holder with and without current dividers can be seen in Fig. 4.2.

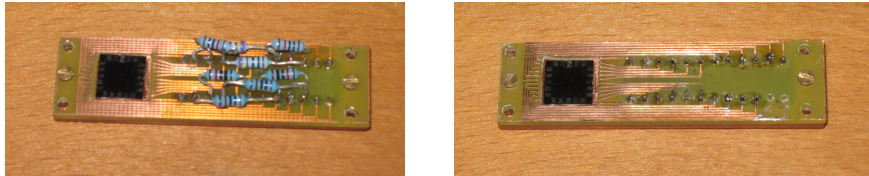


Fig. 4.2: Sampler holder with (left) and without (right) current dividers installed.

The sample is mounted onto the sample holder, which in turn is installed on the ^3He -cryostat and thermally anchored to it. For additional shielding from external fields, a Permalloy shield is installed around the sample.

4.3 Current Ramp Measurements

Current ramp measurements are one means to determine the escape rate of the dc-SQUIDs. Moreover, their direct result, i.e. the probability distribution of the switching currents, gives information about the underlying processes.

The basic setup and procedure for the current ramp measurements is shown in Fig. 4.3. A detailed image of the measurement setup and more information about the experimental procedure can be found in Appendix B.

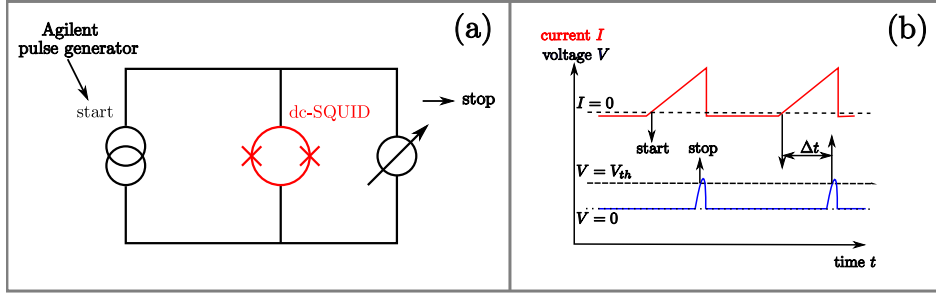


Fig. 4.3: (a) Strongly simplified schematic of the measurement setup. (b) $I(t)$ and $V(t)$ for the current ramp measurement.

The measurement starts by increasing the bias current from a current value $I_{\text{start}} \lesssim 0$, until the voltage across the SQUID switches to some finite voltage above the chosen threshold voltage. The time Δt between the crossing of $I = 0$ and the switching to a voltage $V > V_{\text{th}}$ is measured, and, by multiplying it with the ramping rate \dot{I} , the switching current is determined.

$$I_{\text{sw}} = \Delta t \cdot \dot{I} \quad (4.1)$$

As discussed in Chapter 1, the switching current I_{sw} is less than the critical current I_c in the presence of thermal noise. Thermal or quantum fluctuations also cause the switching events to happen at randomly distributed currents. Thus, repeating the ramping experiment $\sim 10^4$ times yields a statistical probability distribution $P(I)$ of switching currents. The probability that the system will switch to the voltage state in the current interval $[I, I + \Delta I]$ is then given by $P(I)\Delta I$. Obviously $P(I)$ is connected to the escape rate, but it also depends on the rate at which the current is ramped [FD74].

$$P(I) = \Gamma(I) \left(\frac{dI}{dt} \right)^{-1} \left(1 - \int_0^I P(u) du \right) \quad (4.2)$$

For data acquisition and control of the external parameters such as applied flux and repetition rate of the ramping events a custom-made MATLABTM software was used.

Chapter 5

Experimental Results

In this chapter, measurements performed to observe the Münchhausen effect are reported. At first, $I(V)$ -curves of the dc-SQUID were recorded with 'GoldExI' [Gol] to determine the normal resistance R_S of the SQUID. The resistance was then used to calculate the critical current $2I_c$ of the SQUID using the Ambegaokar-Baratoff formula [Tin04]. Additionally, current ramp histograms were recorded at different magnetic flux values. For each SQUID the modulation of the switching current with increasing current through the flux line was recorded over several periods. Since this modulation is periodic in Φ_0 , it allows to calibrate the current through the flux line with respect to Φ_0 .

The shape of the histograms is evaluated and the flux dependence of the critical current is compared with the theoretical predictions.

All measurements, except those examining the temperature dependence, were performed at the base temperature $T_b \approx 300$ mK of the ^3He -cryostat. Since no filters were installed in the electrical lines the effective temperature due to noise from the electronic setup seems to be considerable higher than the physical sample temperature T_b which is measured by the thermometers. Previous measurements with the cryostat and the same measurement setup show that the effective temperature is increased by 200 – 700 mK.

Each of the different SQUIDs is considered separately, since, as it will be shown, they exhibit qualitatively different behavior which corresponds to different underlying mechanisms. SQUIDs S3 and S4 are designed to have the same critical current. In the first two sections it will be shown, that they exhibit thermally activated escape behavior. SQUID S2, on the other hand, shows in addition to TA also phase diffusion, as will be demonstrated in the last section. If not pointed out differently, the measurements were performed on the same chip, AF42. SQUID S1 on chip AF42 was broken; measurements on other chips did not yield analyzable results. Therefore S1 will not be considered in the following.

5.1 SQUID S3

SQUID S3 is the SQUID with the largest coupling constant $k = 0.37$, i.e. the smallest inductance $L = 700$ nH. On the other hand it is one of the two SQUIDs that have larger junctions. The resulting Josephson energy $E_J = I_c\Phi_0/(2\pi)$ corresponds to a temperature $E_J/k_B = 83$ K and puts the system in a regime where MQT is not a dominating process (cf. Ref. [KNC⁺05]). However, without MQT the Münchhausen effect should not be observable and flux dependent measurements support this notion, as will be shown.

5.1.1 $I(V)$ -Characteristic

The $I(V)$ -characteristic of the SQUID shown in Fig. 5.1 yields a normal resistance of $R = 270 \Omega$, and a gap voltage of $V_{\text{gap}} = 2.76$ mV. Using those values the SQUID parameters are calculated. They are given in Tab. 5.1 together with the designed values.

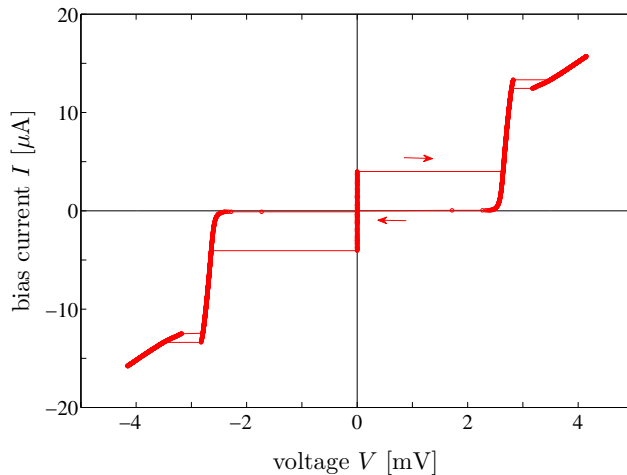


Fig. 5.1: $I(V)$ -curve of S3 taken at $T_b = 300$ mK (phonon temperature).

	$2I_c$ [μA]	R_S [Ω]	k	$\omega_{p1}/(2\pi)$ [GHz]	$\omega_{p2}/(2\pi)$ [GHz]	Q_1	Q_2
measured	8.02	270	0.33	16	133	60	7.7
designed	7.0	-	0.37	16	133	-	-

Table 5.1: Measured and designed SQUID parameters of S3. $Q_1 = \omega_{p1}C_1R$ and $Q_2 = \omega_{p2}C_2R$ are the quality factors of junction 1 and junction 2, respectively.

The measured result for the critical current is larger than the designed value. The deviation of 14% lies within the range that was given in Ref. [DSZN05] but for considerably smaller junctions. Furthermore, the parameters of the junctions of SQUID S2, which are almost an order of magnitude smaller in area, agreed quite well with the designed values as will be shown in Sec. 5.3. It can be assumed that the accuracy of the fabrication process does not decrease with increasing junction size and, in addition, the critical current density for this wafer was measured rather precisely on a large area junction by Kirill Fedorov. Since the $I(V)$ -curve presented here is the only $I(V)$ -curve that was measured and the normal resistance branch is quite short, any value gained from this measurement cannot be considered to be accurate enough. Therefore, we will use the designed critical current value throughout the rest of this section.

Although the designed and measured critical current values are different, the plasma frequencies in Tab. 5.1 are the same. This is based on the interdependence of capacitance and critical current. Both are proportional to the area of the junction and the plasma frequency depends only on the ratio of the two values. Of course, this does not hold for the plasma frequency ω_{p1} of the shunted junction. But in this case, the change in the intrinsic capacitance due to the larger junction area is not noticeable (at least not with the accuracy displayed in Tab. 5.1), since the shunting capacitance is very large. The other possibility, i.e. to explain the increased critical current by an increased critical current density, would of course not yield the same result for the plasma frequencies. However, as mentioned earlier, the critical current density for this wafer was measured rather precisely.

5.1.2 Current Ramp Measurements

Already in the $I(V)$ -curve one can see that the switching current is well below the Ambegaokar-Baratoff value of the critical current. The current ramp histograms support this conclusion. The current was ramped at a rate $\dot{I} = 3.3 \text{ mA/s}$ and the ramping procedure was repeated 64000 times at a rate of 774 Hz.

When calculating the duration of one repetition period T_{rep} and comparing it with the time Δt it takes to ramp the current to the average switching current, one notices that $\Delta t > T_{\text{rep}}$. Since the current source ignores a start signal generated by the pulse generator if it is already in ramping mode (cf. details on the measurement setup in Appendix B) the repetition period is effectively doubled in most ramping events. This is supported by measurements on S4 (next section) for which there are measurements with a corrected repetition rate.

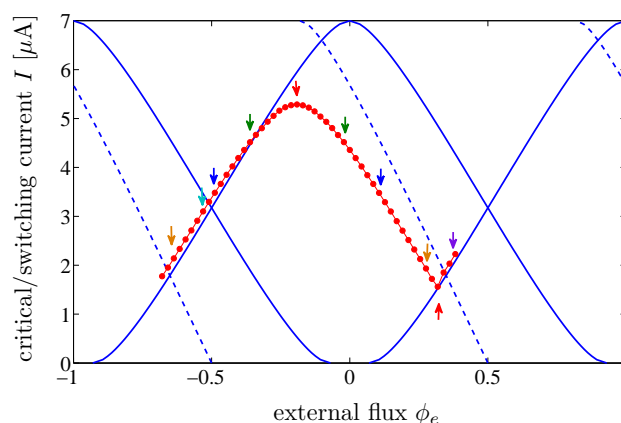


Fig. 5.2: Flux dependence of the switching current of S3. The red circles give the mean switching current of the main peaks. The solid lines give the dependence of the critical current I_0 on external flux ϕ_e for the classical symmetric dc-SQUID; dashed lines represent the predicted switching current due to tunneling. All blue lines were calculated using the designed SQUID parameters. Colored arrows refer to the respective histograms shown in Fig. 5.3.

In Fig. 5.2, the measured dependence of the switching current on the external flux (red circles) is shown together with the calculated critical current vs. magnetic flux dependence $I_0(\phi_e)$ (solid lines). The magnetic flux is given in dimensionless units $\phi_e = \Phi_e/\Phi_0$. For completeness, the predictions of the Münchhausen effect $I_{c,n}^+(\phi_e)$ are also plotted with dashed blue lines. The different currents were introduced in Chapter 1 and a table listing all of them can be found in Appendix C.

Each data point in Fig. 5.2 represents one measured histogram and gives the mean switching current of the main peak of the histogram. The main peak corresponds to the escape out of the deepest minimum and is always situated at higher switching currents.

For the sake of clarity not all histograms are shown in Fig. 5.3. The corresponding data points in the flux dependence plot are indicated by colored arrows. For better visibility histograms corresponding to points on the positive and on the negative slope are shown in separate diagrams. Histograms that were measured close to the minima of the $I_0(\phi_e)$ -curve show additional peaks at smaller bias currents. They will be discussed later.

At a first glance, it seems as if the measured data agree quite well with the Münchhausen effect. Indeed, the shift of the flux dependence curve is an intrinsic effect of the Münchhausen theory [TGB09]. In this picture, when moving from negative to positive external flux values,

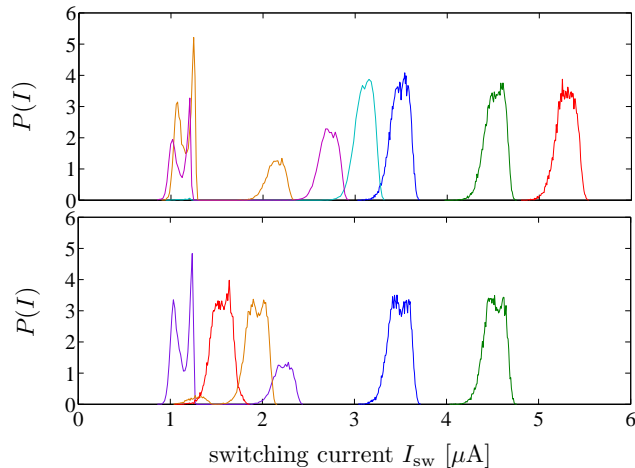


Fig. 5.3: Histograms of S3 at different flux values. Colors of the histograms correspond to the color of the arrows in Fig. 5.2. The upper diagram shows the histograms on the left shoulder of the flux dependence, including the histogram with the maximum switching current, while the lower picture shows histograms right of the maximum. For the sake of clarity, not all histograms are plotted.

the escape is triggered first by TA in φ_1 -direction. Once the maximum is reached, the TA escape changes to MQT in φ_2 -direction until it switches back to TA, when the next side minimum becomes the deepest. Yet, the recorded switching current always stays below the critical current curves $I^+(\phi_e)$ (cf. Appendix C). At a bias current below $I^+(\phi_e)$, the adjacent minimum in φ_2 -direction is still energetically higher than the one currently occupied. Thus, the Münchhausen effect is not feasible to explain the early switching.

The other possibility is to assume only TA as escape mechanism. Then, the maximum switching current should be measured at an external flux value of $\phi_e^{\text{theo}} = 0$. However, the curve is shifted from this theoretically expected value to $\phi_e^{\text{meas}} = -0.19$. This results either from some trapped flux in the SQUID loop or asymmetries in the SQUID. In the following, first the shift in the flux dependence will be discussed and later the histograms and escape rates will be evaluated.

Shift in Flux Dependence

First of all, the effect of asymmetries in the critical currents of the two junctions α and in the inductances of the two SQUID arms η is considered (cf. Sec. 1.3). According to Ref. [CT77] the flux value with a maximum switching current of ϕ_e^{max} can be used to calculate one of the asymmetry parameters α and η , assuming that the other is zero.

$$\phi_e^{\text{max}} = -\frac{\beta_L(\alpha + \eta)}{2\pi} \quad (5.1)$$

Obviously, this yields the same result for both parameters, either $\alpha = 0.44$ and $\eta = 0$ or $\alpha = 0$ and $\eta = 0.44$. In Fig. 5.4 these two possibilities are compared with the measured results. Additionally, the effect of additional flux, that might be trapped in the loop is depicted.

All three calculated curves are scaled with respect to the maximum measured switching current to facilitate the comparison with the measured results. None of the calculated curves reproduces the measured curve. This is not surprising, since for each flux value the same

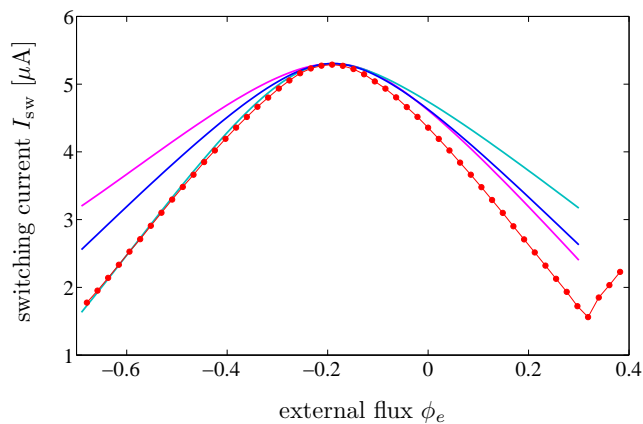


Fig. 5.4: Comparison of the calculated critical current vs. flux dependence with the experimental results (red). All calculated curves are scaled by a factor 0.7 to match the maximum critical current $2I_c$ and the maximum switching current at ϕ_e^{\max} . The dark blue curve corresponds to a shift of the classical symmetric dependence by $\Delta\phi_e = -0.19$, the pink curve depicts the effect of $\alpha = 0.44$ and $\eta = 0$ and the light blue curve shows the opposite case, $\eta = 0.44$ and $\alpha = 0$.

scaling factor is used. However, the measured curve gives, simplified, the current value at which the barrier height along the optimal trajectory is comparable to temperature. It cannot be assumed that the ratio between this current value and the critical current $I_0(\phi_e)$ stays the same, when ϕ_e is changed.

As it turns out, the flux dependence is explained consistently for all flux values only by a shift of the $I_0(\phi_e)$ -curve due to some trapped flux in the loop. Of course, the proper combination of $\alpha + \eta = 0.44$ might also yield the desired symmetric result, but in order to achieve balance, the two asymmetry parameters would have to be roughly equal, i.e. $\eta \approx 0.2$. Such a large relative difference between the two SQUID arms could be noticed almost with the bare eye, but certainly under the microscope, which is not the case. Therefore, no asymmetries are considered in the following discussion and the effective flux in the SQUID loop is taken to be $\phi_e^{\text{eff}} = \phi_e^{\text{meas}} + 0.19$.

Histograms and Escape Rates

We start with comparing the measured histogram with the maximum switching current (down pointing red arrow in Fig. 5.3) to histograms generated by the simulation described in Chapter 3. The simulated histograms were generated at $\phi_e^{\text{eff}} = 0$ and for different temperature values (cf. Fig. 5.5). In the simulation, the designed SQUID parameters, as presented in Tab. 5.1, were used (apart from R , where only the measured result exists). The only deviation from the experiment is a slight change in the ramping rate. Instead of $\dot{I} = 3.3 \text{ mA/s}$, $\dot{I} = 4 \text{ mA/s}$ is used. However, this effect is negligible.

In order to generate histograms a break condition is included in the simulation which mimics the threshold voltage in the current ramp measurement. The integration process is repeated ~ 200 times and the normalized currents at which the break condition is fulfilled are recorded.

The comparison with the simulation shows that the temperature that would match simulation with measurement is $T \gtrsim 2 \text{ K}$. This temperature is supported by the comparison of the escape rates, but does not agree with the effective temperature usually measured in the cryostat.

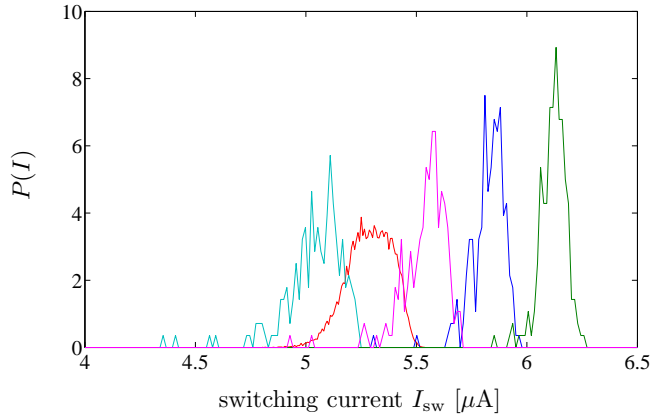


Fig. 5.5: Comparison of the histogram with the maximum switching current, measured at $\phi_e^{\text{meas}} = -0.19$, with histograms generated by the simulation for temperatures $T = 1$ K (green), $T = 1.5$ K (dark blue), $T = 2$ K (pink) and $T = 3$ K (light blue).

Explanations will be given at the end of this section.

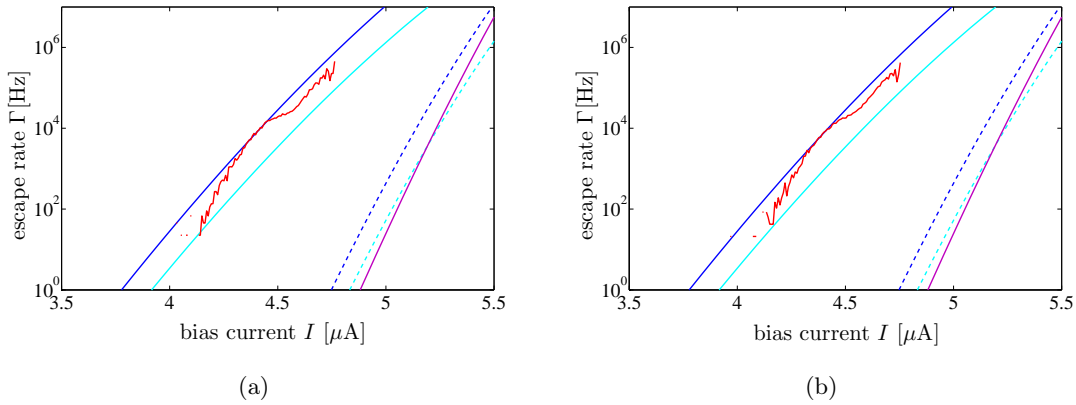


Fig. 5.6: Comparison of the measured escape rates (red solid line) with the calculated escape rates in a 2D potential. (a) Escape rate measured at $\phi_e^{\text{meas}} = -0.36$ and (b) escape rate measured at $\phi_e^{\text{meas}} = -0.02$. The solid blue lines correspond to the TA rates with $T = 2.1$ K. The dark and light blue lines depict the thermal rate with an attempt frequency defined by ω_{p2} and ω_{p1} , respectively. For comparison, the dashed blue lines display the thermal escape rate for $T = 1$ K (dark and light blue again stand for the light and heavy junction). For completeness, the purple line shows the MQT rate.

The escape rates for TA and MQT in a 2D potential can be calculated using Eqs. (1.33) and (1.34). In Fig. 5.6 they are compared to the measured escape rates. Since simplifying assumptions about the normal mode frequencies do not hold anymore for $I_0(\phi_e) \approx 2I_c$ (cf. Sec. 1.3), the two histograms denoted by green arrows are investigated instead. They are measured at effective flux values $\phi_e^{\text{eff}} = \pm 0.17$. The required parameters x_c , y_c and $I_0(\phi_e)$ are obtained by solving Eqs. (1.28)-(1.30) for the respective flux values. Inserting those values in Eqs. (1.33) and (1.34) yields the escape rates for TA and MQT, respectively. They are depicted in Fig. 5.6. The only difference between light and dark blue curves of the same line style are the attempt frequencies $\omega_A = \omega_p(1 - j^2)^{1/4}$. Due to the capacitive asymmetry of the SQUID the plasma

frequencies of the two junctions are different. The dark blue line represents the escape rate if the plasma frequency of the unshunted junction 2 is used, the light blue line corresponds to the escape rate of the shunted junction 1.

In Fig. 5.6, the red measured curves are situated in between the two thermal escape rates (plotted light and dark blue) calculated with $T = 2.1$ K. This can be understood when considering the 2D potential for this SQUID at flux values $\phi_e^{\text{eff}} = \pm 0.17$ as depicted in Fig. 5.7. The escape starts with an angle $\theta = \pm 23^\circ$. However, the plasma frequencies that determine the prefactor of the escape rate are defined only in φ_1 - and φ_2 -direction (i.e. $\theta = \pm 45^\circ$). Thus, the real attempt frequency for the actual escape direction lies somewhere in between the two known frequencies. Consequently, the red measured curves are situated in between the two calculated rates in Fig. 5.7.

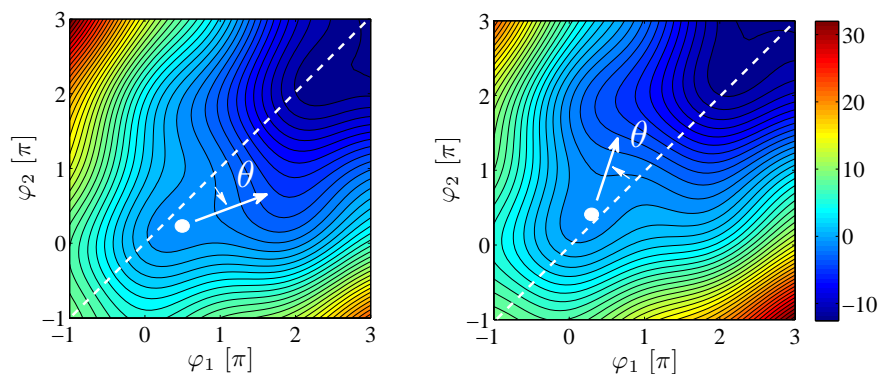


Fig. 5.7: Potential landscape of S3 for $\phi_e^{\text{eff}} = 0.17$ (left) and $\phi_e^{\text{eff}} = -0.17$ (right) at a bias current that is equal to the normalized critical current $j_0(\phi_e^{\text{eff}} = \pm 0.17) = 0.89$. The bisectrix is illustrated by a dashed white line, the escape direction with an arrow.

Additionally, it should be noted that the tunneling rate (solid purple in Fig. 5.6) is calculated for the correct deflection from the bisectrix but with the plasma frequency ω_{p2} of the light junction. However, as explained, the actual attempt frequency is smaller than ω_{p2} . Still, the calculated rate is much smaller than the measured result. This supports the conclusion that the Münchhausen effect is not observed in this measurement.

As a matter of fact, even at temperatures below the crossover temperature of $T_{\text{cr}} \approx 1$ K when MQT becomes the dominating escape process the escape rate is not increased. Therefore, although tunneling might be possible at a bias current I_c^+ this does not mean that the escape rate is already appreciable at this current value. The ratio of Josephson energy to the plasma frequency of junction 2 $E_J/(\hbar\omega_{p2}) \approx 13$ defining the exponent of the tunneling rate indicates that the bias current at which tunneling is observable is higher than the effective critical current I_c^+ considered in Ref. [TGB09].

Flux Dependence of the Histograms

When investigating histograms that are measured at the same absolute value of effective flux, a difference between the two of them is noticed. In Fig. 5.8 histograms measured at positive effective flux are plotted with solid lines, histograms at negative effective flux are depicted with dashed lines. The same color connects histograms measured at the same absolute value of effective flux.

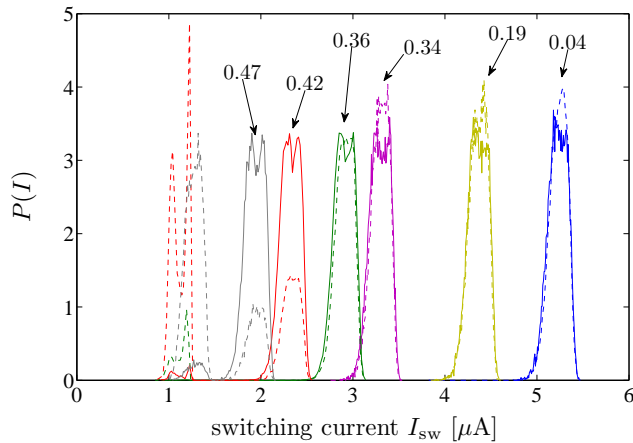


Fig. 5.8: Histograms recorded at different flux values. The numbers give the absolute effective flux value. Histograms plotted with solid lines are measured at positive effective flux while histograms plotted with dashed lines are recorded at negative flux values. Histograms with the same color correspond to the same absolute flux value given in the picture.

Starting with the solid histograms ($\phi_e^{\text{eff}} > 0$), it is clearly noticeable that the main peak moves to smaller switching currents, as the external flux is increased. Upon approaching $\phi_e^{\text{eff}} = 0.5$ a second peak arises (red and grey solid) at lower bias currents that results from escape out of the side minimum as depicted by empty circles in Fig. 5.9.

The behavior of the dashed histograms ($\phi_e^{\text{eff}} < 0$) is similar to the solid ones: Increasing the flux in negative direction leads to decreasing switching currents. However, the second structures at lower currents start to grow much earlier. Besides, there is a threshold value in the switching current. Starting at $\phi_e^{\text{eff}} = -0.5$ and increasing the flux towards $\phi_e^{\text{eff}} = 0$, the single minor peak turns into a double peak and does not continue to move to smaller bias currents (cf. grey, red and green dashed histograms in Fig. 5.8).

In the following the above observations shall be explained. In Fig. 5.9, the potential for $\phi_e^{\text{eff}} = \pm 0.34$ is displayed. For negative flux values (top row), the escape out of the main minimum starts with an escape in φ_1 -direction, the escape out of the side minimum starts in φ_2 -direction. The opposite applies for retrapping. If the phase particle is retrapped in the main minimum, its last motion was in φ_2 -direction, while the retrap process in the side minimum ends with moving in φ_1 -direction. For positive effective flux values, the escape and retrapping directions are inverted.

In Fig. 5.8, the area beneath the main or the minor peak represents the escape probability out of the main or the side minimum, illustrated by solid and empty circles in Fig. 5.9. However, in order to be able to escape out of the side minimum the particle has to be retrapped in it before. The question is now, why the retrapping probability is higher for one flux polarity than for the other. The answer is found in the different effective masses of the particle for the orthogonal directions. In order to be retrapped in a side minimum, the particle has to overcome an additional barrier either in φ_1 -direction ($\phi_e^{\text{eff}} < 0$) or in φ_2 -direction ($\phi_e^{\text{eff}} > 0$).

Once the system enters the voltage state, the bias current is set to zero.¹ Since the system is underdamped, the particle is not retrapped at once but is decelerated and still overcomes several of the rising barriers before being stopped. When the particle is in the running state,

¹in fact, the current is set to a value a little bit below zero, but the system still can relax (cf. Appendix B)

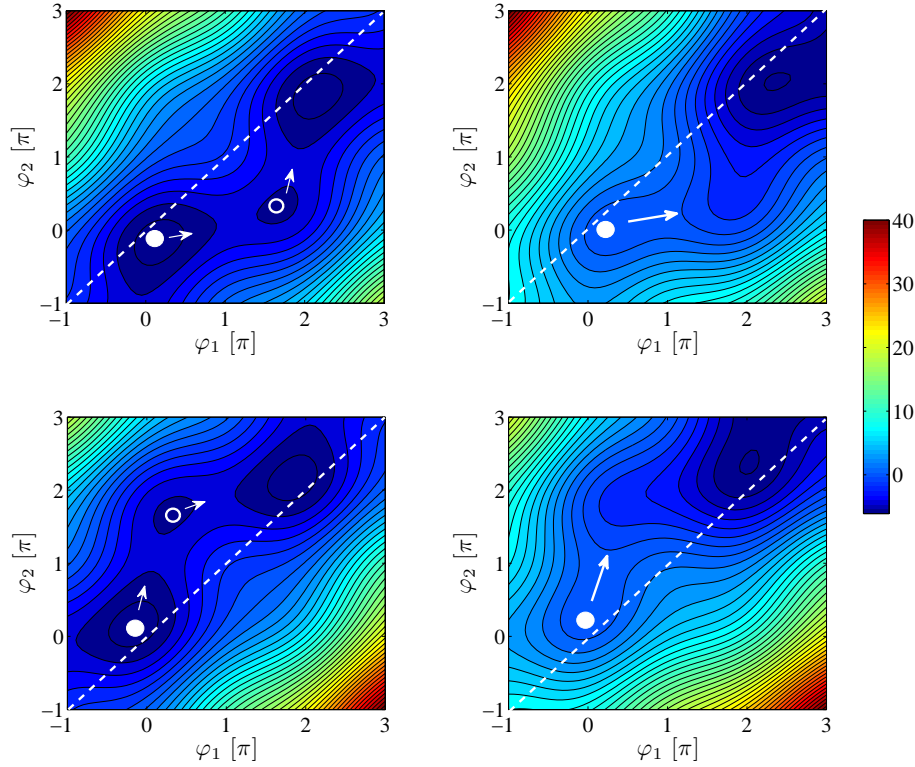


Fig. 5.9: 2D potential for $\phi_e^{\text{eff}} = -0.34$ (top row) and $\phi_e^{\text{eff}} = 0.34$ (bottom row) at bias currents $j = 0$ (left) and $j = 0.5$ (right). Solid and empty circles depict the main and the side minimum, respectively. Arrows point in the direction of escape.

the velocities are equal in both directions. However, due to the larger mass the momentum in φ_1 -direction is larger and it is easier for the particle to overcome an additional barrier in φ_1 -direction. Therefore, the probability of being retrapped in the side minimum is larger if the side minimum is situated in φ_1 -direction of the main minimum. This is the case for negative effective flux (cf. top row in Fig. 5.9). Indeed, the corresponding dashed histograms in Fig. 5.8 show larger minor structures than the solid histograms.

The reason why the single minor peak changes into a double peak structure and why this double peak structure does not move to lower switching currents upon decreasing $|\phi_e^{\text{eff}}|$ could not be found.

Now, the main part of the histograms that result from escape out of the main minima are considered. The different masses, i.e. plasma frequencies in the orthogonal directions also affect the escape rate. As the plasma frequency defines the prefactor of the escape rate, a larger plasma frequency leads to higher escape rates at lower bias currents for the escape out of the main minimum. As already mentioned above, positive effective flux (solid lines) supports the escape out of the main minimum in φ_2 -direction and negative flux supports the escape in φ_1 -direction (cf. Fig. 5.9). Due to the larger plasma frequency in φ_2 -direction, the switching current for positive effective flux should be lower than for negative effective flux. Indeed, when comparing histograms at the same absolute flux value, the main part of histograms with the same absolute flux values are shifted slightly relative to each other at least for $|\phi_e^{\text{eff}}| > 0.3$

and the shift increases with increasing flux. Thus, also the main peaks are affected by the asymmetry of the SQUID.

For flux values $|\phi_e| < 0.3$, the the angle between escape trajectory and bisectrix is too small and the attempt frequency is dominated by the mean value of the two plasma frequencies, instead.

Temperature

The comparisons of the measured results with the simulated histograms as well as the calculated escape rates yield similar temperatures. Both of them are considerably higher than the phonon temperature $T_b \approx 300$ mK that the thermometer displays.

One explanation for this discrepancy could be that the barrier height is smaller than assumed. This would mean, that the critical current, that defines the Josephson energy, is smaller than designed. However, although the values calculated from the design and extracted from the $I(V)$ -curve do not agree perfectly, they indicate a higher critical current, not a lower. Both, fabrication and the Ambegaokar-Baratoff formula are usually reliable and there is no indication to assume otherwise. Therefore, this explanation can be excluded.

Another explanation might be that the effective temperature in the experiment is in fact as high as simulation and calculation let assume. However, the cryostat was and is extensively used and the temperature never was estimated to be above 1 K. Thus, the effective temperature has to be explained by additional noise, that most probably originates from within the electronic setup and couples to the SQUID.

5.1.3 Conclusions

The experimental results themselves as well as the comparison with calculations show that the Münchhausen effect is not observed in this measurement. In fact, the ratio determining the tunneling rate $E_J/(\hbar\omega_{p2})$ is too large to permit tunneling in φ_2 -direction with an appreciable rate at bias currents considerably below the critical current. Thus, even for lower temperatures the Münchhausen effect should not be observable for S3, at least not as strongly as predicted in Ref. [TGB09].

Histograms recorded at the same absolute flux value but with different polarities show a shift relative to each other. Additionally, the respective parts of the histograms that correspond to the escape out of a side minimum occur with different probabilities. Both effects could be attributed to the different plasma frequencies of junction 1 and junction 2.

Another observation that should be noted is the temperature difference between the physical temperature of the cryostat and the effective temperature necessary to explain the reduction of the switching current. Its origin seems to be additional electronic noise.

5.2 SQUID S4

SQUID S4 and SQUID S3 were designed to have the same junction size. As for S3 the designed values for the critical current will be used. They can be found in Tab. 5.2.

	$2I_c$ [μ A]	R_S [Ω] ²	k	$\omega_{p1}/(2\pi)$ [GHz]	$\omega_{p2}/(2\pi)$ [GHz]	Q_1	Q_2
designed	7.0	270	0.13	16	133	60	7.7

Table 5.2: Designed SQUID parameters of S4.

Having the same critical current as S3 results in having the same Josephson energy $E_J/k_B \approx 83$ K. Therefore, MQT and the Münchhausen effect can be excluded again as dominating escape mechanisms. As will be shown, the behavior of S4 is similar to S3, the only difference is the different coupling constant k which creates more different minima in the potential (cf. Sec. 1.3.1).

5.2.1 Current Ramp Measurements

Switching current histograms were measured at different flux values. Each histogram consists of 64000 single ramping measurements. The repetition rate 774 Hz was the same as for S3 and the ramping rate $\dot{I} = 3.5$ mA/s differed only slightly from the ramping rate of S3 ($\dot{I}_{S3} = 3.3$ mA). This means that the same issue of having a repetition period which is shorter than the time Δt it takes to ramp the current to its switching value arises. However, in this case the mistake was corrected. The switching current vs. flux dependence over several Φ_0 was measured with the same ramping rate, but only half the repetition rate.³

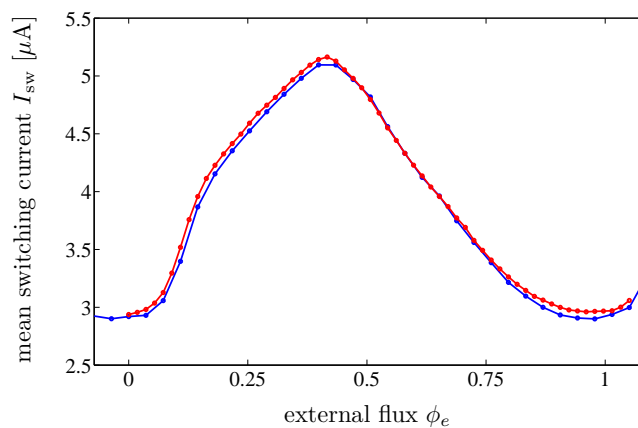


Fig. 5.10: Comparison of the mean switching current vs. flux dependence curves with a repetition rate of 774 Hz (red) and 372 Hz (blue).

Comparing the two measurements (cf. Fig. 5.10) indicates clearly, that there is no qualitative and hardly any quantitative difference between the two measurements. Thus, the repetition period is indeed doubled automatically, as already suggested in the previous section and the measurement over only one period of Φ_0 with more histograms and better statistics can and will be used. The curves are not symmetric because the mean switching current includes also the double peak structures that correspond to an escape out of a side minimum. If only the flux dependence of one single peak is plotted, this asymmetry vanishes (cf. Fig. 5.11).

In Fig. 5.12 some of the recorded histograms are presented. The colors correspond to the arrows in Fig. 5.11 and the histograms always show a double peak structure. Additionally, a second (minor) double peak structure arises when approaching the minima of the switching current vs. flux dependence. It again corresponds to the escape out of a side minimum. The switching current of both main peaks is plotted in Fig. 5.11 in dependence of external magnetic flux (green and red data points). The solid blue curve represents the classical $I_0^{(n)}(\phi_e)$ -

²the resistance measured for SQUID S3 is used since no $I(V)$ -curve was recorded for S4 on AF42

³Originally the curve over several periods of Φ_0 was recorded and used to determine the relation between the current sent through the flux line and Φ_0 .

dependence. For the sake of completeness, the Münchhausen tunneling curves are plotted with dashed lines.

The reason why the Münchhausen effect can be excluded as possible escape mechanism is the same as for S3. Although the smaller coupling parameter $k = 0.13$ decreases the barrier height of the 2D potential in φ_2 - (and in φ_1 -) direction, TA is still the dominating process. Even at lower temperatures MQT is not possible with an appreciable rate for currents considerably below the critical current.

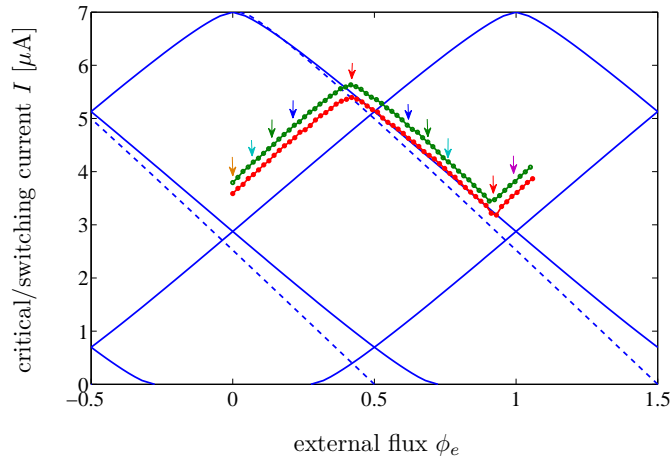


Fig. 5.11: Flux dependence of the switching current of S4 compared with the classical theory (solid blue line) and the prediction of the Münchhausen theory for the flux dependence of I_c^+ (dashed blue lines). The red dots correspond to the current value at the small peak, the green dots to the current value of the high peak. The color of the arrows connects the indicated data points to the histograms in Fig. 5.12.

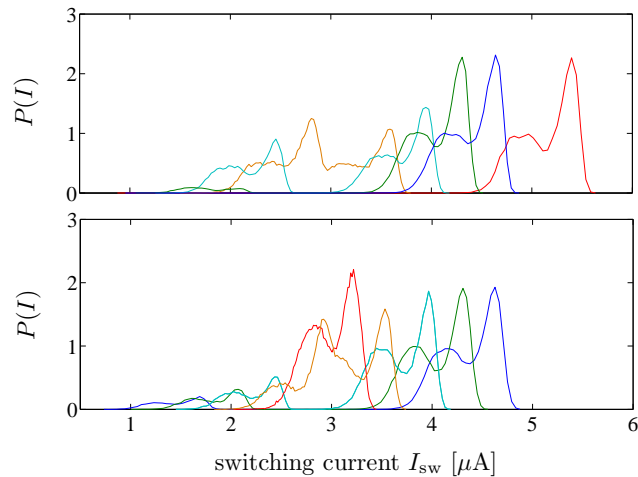


Fig. 5.12: Histograms measured for S4 at different flux values. The upper diagram depicts histograms measured at $\phi_e^{\text{meas}} \leq -0.19$ while the lower pictures shows histograms for $\phi_e^{\text{meas}} > -0.19$. The different colors correspond to the colored arrows in Fig. 5.11.

Shift in Flux Dependence

The shift in flux dependence is evaluated as was done already in the previous section for S3. Using Eq. (5.1), the shift could be explained by $\alpha = -0.34$ and $\eta = 0$ or vice versa and any combination of $\alpha + \eta = -0.34$. The results are presented in Fig. 5.13. The most successful and only consistent explanation is again a simple shift of the flux dependence curve of the symmetric SQUID. This means that there is again flux trapped in the loop. The effective flux threading the loop is $\phi_e^{\text{eff}} = \phi_e^{\text{meas}} - 0.42$.

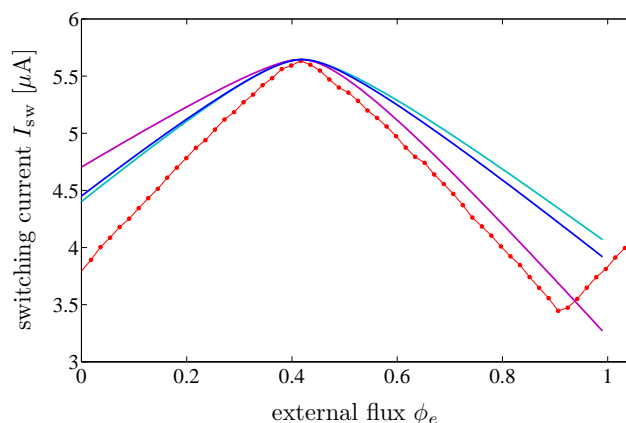


Fig. 5.13: Comparison of the calculated with the measured (red) critical current vs. flux dependences. The curve corresponding to the sharp peak at higher bias currents is plotted. Again, the calculated curves are scaled to match the maximum critical current at $\phi_e = 0.42$ to facilitate the comparison. The dark blue curve shows the symmetric flux dependence that is shifted by $\Delta\phi_e = 0.42$. The light blue curve corresponds to an asymmetry in critical current of $\alpha = -0.34$, the purple curve to an asymmetry in inductance, $\eta = -0.34$.

Histograms and Escape Rates

As for S3, the histogram at $\phi_e^{\text{eff}} = 0$ is compared with results of the simulation for different temperatures (cf. Fig. 5.14). The simulated histograms are obtained as explained in the previous section. Additionally, the escape rates extracted from the histograms at $\phi_e^{\text{eff}} = \pm 0.20$ and the calculated escape rates for the 2D potential are juxtaposed in Fig. 5.15.

Due to the width of the double peak structure the comparison of the simulated with the measured histograms cannot be very accurate. Nonetheless, it suggests an effective temperature $T \approx 2$ K, that was already extracted from the measurements on S3. The same temperature range $1.5 \text{ K} < T < 2.1 \text{ K}$ is obtained when comparing the calculated escape rates with the measured rates (cf. Fig. 5.15). In order to explain the full double peak structure two different temperatures $T = 2.1 \text{ K}$ (solid blue curves) and $T = 1.5 \text{ K}$ (dashed blue curves) have to be applied.

The difference between light and dark blue curves are again the different attempt frequencies. The light blue curve is calculated with the plasma frequency ω_{p1} of junction 1, the dark blue curve is calculated with ω_{p2} of junction 2. The measured rate is situated in between the light and dark blue curves (as for S3). The reason therefor is the same as for S3. The direction of escape is not deflected enough from the bisectrix and the escape is determined by an effective plasma frequency corresponding to the mean value of ω_{p1} and ω_{p2} .

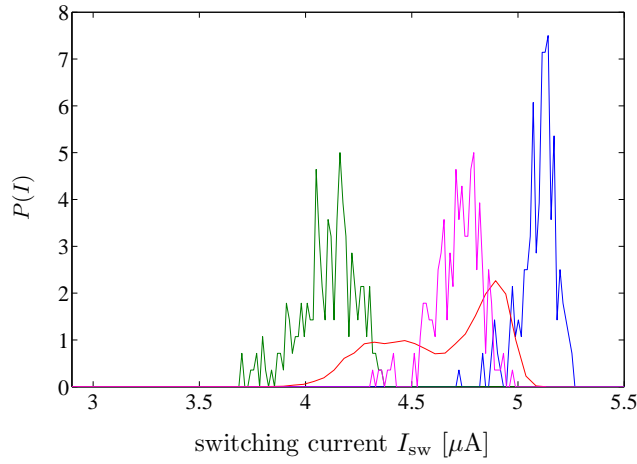


Fig. 5.14: Comparison of the measured histogram at $\phi_e^{\text{eff}} = 0$ (red) with histograms generated by the simulation for $T = 1.5$ K (blue), $T = 2$ K (pink) and $T = 3$ K (green).

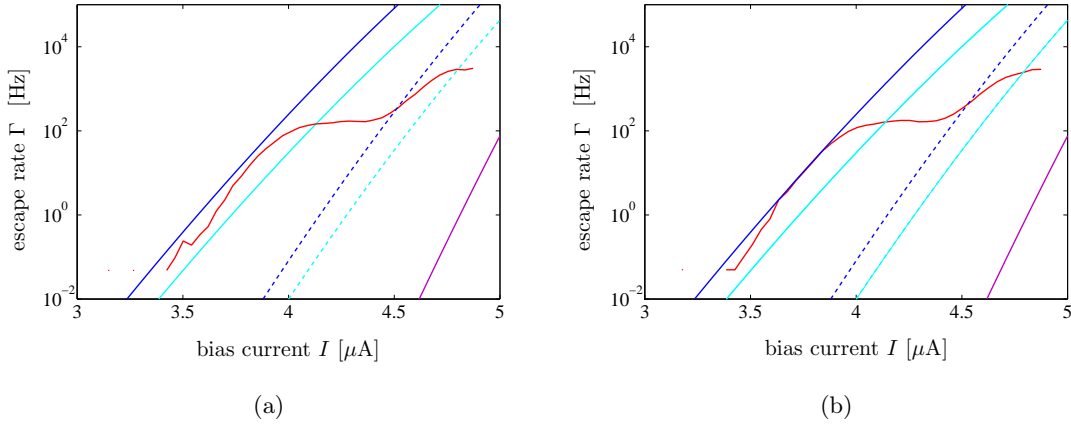


Fig. 5.15: Measured escape rates (red) at effective flux values (a) $\phi_e^{\text{eff}} = -0.2$ and (b) $\phi_e^{\text{eff}} = 0.2$ are compared with the calculated escape rates. The solid lines depict the thermal escape rates at $T = 2.1$ K with different attempt frequencies in φ_1 - and φ_2 -direction (light and dark blue, respectively). The dashed curves give the thermal escape rates at $T = 1.5$ K with the same color code as for $T = 2.1$ K. The purple lines represent the escape rate due to MQT.

Neither the calculated escape rates nor the simulation reproduces the double peak structure of the measured histograms. For the calculated escape rate this is obvious since it considers only one frequency for the full system. The simulation however includes the full asymmetric system. The fact that it still does not produce two peaks suggests that the reason for the double peaks is not intrinsic to the system but instead due to some nonequilibrium effect such as a too short relaxation time in the current ramp measurement.

Double Peak Structure

To be able to continue evaluating the results for S4, the origin of the double peak structure should be understood. Besides, it should be known which peak to consider in the following discussion.

In Fig. 5.15, the lower part of the escape rate corresponds to the smaller peak at smaller bias currents. Its slope agrees almost perfectly with the TA rate at 2.1 K, the same temperature that was already estimated for S3. Thus, it seems to be obvious to choose the lower peak as the one to consider. However, a mechanism that prevents the escape and keeps the particle in its minimum in order to explain an additional peak at higher bias currents could not be found. In contrast, an additional peak at lower currents can be explained by additional noise or nonequilibrium effects. For instance, the time between stop and start of the current ramp might have been too short to allow the system to fully relax every time.

The notion, that the additional peak results from nonequilibrium effects is further supported by measurements on the same SQUID S4 but on another chip (chip AF24). Those measurements were performed with current dividers installed on the sample holder (details can be found in Appendix B) and with a considerably lower ramping rate $\dot{I} = 0.12$ mA/s as well as longer repetition periods $T_{\text{rep}} = 100$ ms. Unfortunately, only the switching current of the full resistor-SQUID system was measured. The actual switching current of the SQUID had to be extracted a posteriori by comparing the $I(V)$ -curves with and without current dividers. For lack of knowledge, the a priori method of renormalizing the ramping rate during the measurement was not used.

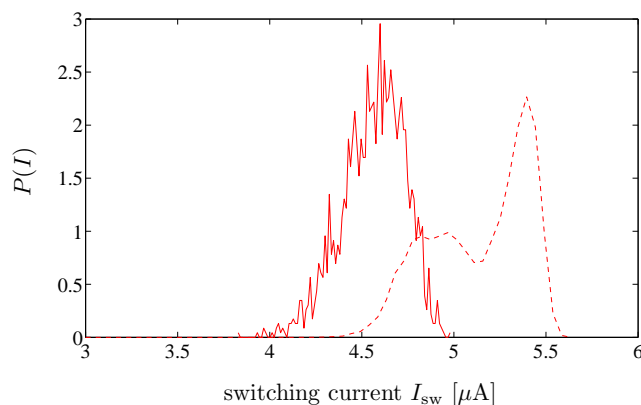


Fig. 5.16: Histograms measured for S4 on AF24 with current dividers (solid red line) and for S4 on AF42 without current dividers (dashed red line). Each time the histogram with the maximum switching current is presented. Note that the position of the single peak histogram is not very accurate due to the very rough method of recalculating the actual switching current from the measured one.

Clearly, the histogram obtained for the measurement with current dividers does not display a double peak structure. Assuming that both SQUIDs are as designed, the only difference between the two measurements is the reduction of noise due to the installed current dividers, a lower ramping rate and a longer relaxation time between stop and start of the current ramp.

Thus, the smaller peak at lower currents might in fact be due to a short relaxation time. In this case, the sharper peak at higher switching currents should correspond to the escape of the fully relaxed system. Still, some unanswered questions remain, for example, why the slope of measured escape rate does not agree with the slope of the calculated TA rate in Fig. 5.6 and why the effective temperature for this SQUID, $T \approx 1.5$ K is smaller than $T \approx 2$ K obtained for S3. Additionally, the width of the histogram recorded with current dividers seems to be comparable to the width of the full double peak structure in Fig. 5.16.

Since the real switching current of SQUID S4 on AF24 is known only very roughly, a further evaluation of this SQUID is omitted. The comparison with simulation as well as with the calculated escape rates relies on knowing the switching current and therefore cannot be performed. Additionally, the recorded flux dependence of the switching current histograms does not contain enough data to allow for a satisfying examination of the flux dependence of the histograms.

Flux Dependence of the Histograms

Although the issue of the double peak structure is not solved completely, the flux dependence of the histograms shall be evaluated nonetheless. In Fig. 5.18 the 2D potential for effective flux values $\phi_e^{\text{eff}} = \pm 0.3$ is displayed. The white arrows denote the escape direction. As explained before, the attempt frequencies in the two orthogonal directions are not equal and different flux polarities support different escape directions. Therefore, similar to SQUID S3 the histograms show different behavior in positive and negative flux direction (Fig.5.17).

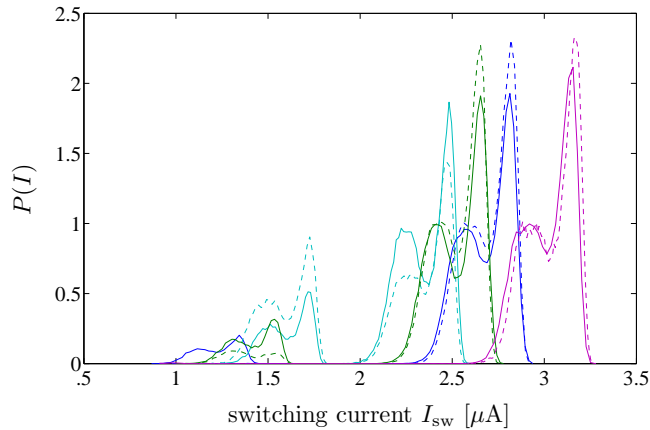


Fig. 5.17: Measured histograms at different flux values. Histograms plotted with solid or dashed lines are recorded at effective flux values $\phi_e^{\text{eff}} > 0$ or $\phi_e^{\text{eff}} < 0$. Histograms with the same color correspond to the the same absolute flux value $|\phi_e^{\text{eff}}| = 0.2$ (dark blue), $|\phi_e^{\text{eff}}| = 0.27$ (green) and $|\phi_e^{\text{eff}}| = 0.34$ (light blue).

In Fig. 5.17, histograms with solid lines are recorded at flux values $\phi_e^{\text{eff}} > 0$ and histograms with dashed lines at $\phi_e^{\text{eff}} < 0$. Histograms with the same color correspond to the same absolute effective flux value $|\phi_e^{\text{eff}}|$. Additionally, the colors again correspond to the arrows in Fig. 5.11.

We start with investigating the minor double peak structures that correspond to an escape out of the side minimum (empty circles in Fig 5.18). At flux values $|\phi_e^{\text{eff}}| \approx 0$ (purple histograms) there is no evidence of escape out of a side minimum. This is because, even if the particle was retrapped in a side minimum (empty circles in Fig. 5.18), overcoming the barrier between side and main minimum does not result in the escape to the running state. Instead, the particle is retrapped in the main minimum.

In Fig. 5.17, at some flux value the minor histograms start to arise. For negative and positive flux direction they start to grow at different flux values and with different speed, for example when comparing the dark blue histograms: While there is no second double peak structure at $\phi_e^{\text{eff}} = -0.2$ (dashed dark blue), the minor double peaks are clearly visible for $\phi_e^{\text{eff}} = 0.2$ (solid dark blue). Nonetheless, at $|\phi_e^{\text{eff}}| = 0.34$, the dashed minor double peak structure outgrew the solid minor structure.

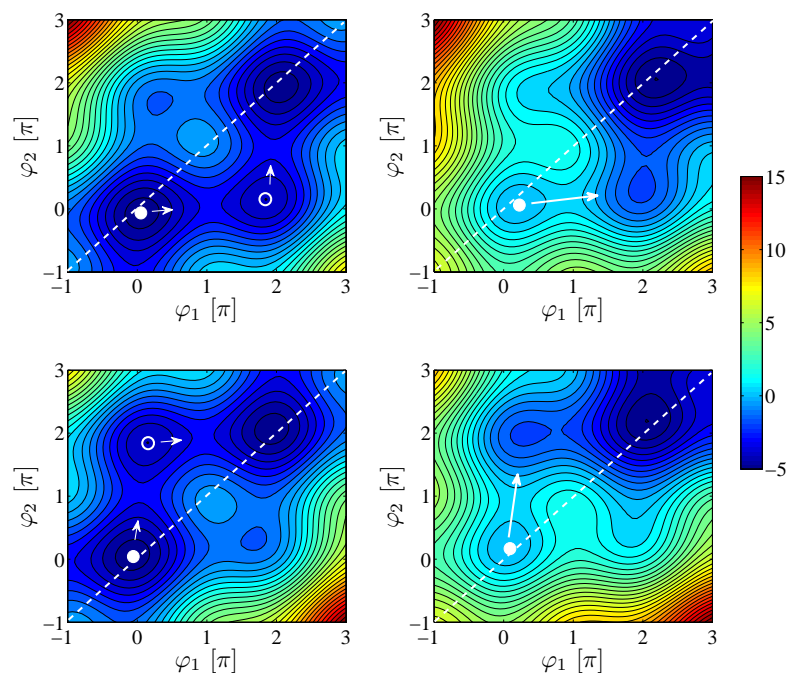


Fig. 5.18: 2D potential at a normalized bias current $j = 0$ (left column) and $j = 0.4$ (right column) at $\phi_e^{\text{eff}} = -0.3$ (top row) and $\phi_e^{\text{eff}} = 0.3$ (bottom row). Solid circles depict the main minimum, empty circles the side minimum. Arrows denote the escape direction out of the main minimum.

The explanation for both observations can be found in the capacitive asymmetry of the system. For negative applied flux, the particle leaves the main minimum in φ_1 -direction (cf. top row in Fig. 5.18) but the side minimum in φ_2 -direction. If localized in the side minimum at zero bias, the particle can leave this minimum already at small currents and in φ_2 -direction. However, the large mass of the particle in φ_1 -direction prevents the further escape. Or, in other words, the damping due to the large shunting capacitance of junction 1 is strong and causes the particle to be retrapped in the main minimum.

The effect of damping when leaving the side minimum in φ_1 -direction ($\phi_e^{\text{eff}} > 0$) is small because it is defined by the small intrinsic capacitance of junction 2. Thus, the particle is not retrapped in the main minimum and instead, starts to run down the potential. Then the system switches to the finite voltage state. This explains why there is a minor histogram for the solid dark blue curve ($\phi_e^{\text{eff}} > 0$) but none for the dashed dark blue curve.

The reason why the minor peaks grow faster for $\phi_e^{\text{eff}} < 0$ than for $\phi_e^{\text{eff}} > 0$ is the same as explained already for S3: The retrapping probability is not the same for positive and negative effective flux.

There are two mechanisms that determine the behavior of the minor part of the histograms. The first mechanism influences the escape probability out of the side minimum and was explained above. Its impact decreases with increasing absolute value of flux. The second mechanism was already explained in the previous section and it affects the probability of being retrapped in the side minimum and increases with increasing absolute value of flux. Combined, they explain the different evolution of the minor double peaks for positive and negative

applied flux.

As for S3, a small shift between the main double peak structure of the same color can be observed. However, it does not seem to increase with increasing flux and the effect is not strong enough to exclude an inaccuracy in determining the value of the applied flux as possible explanation for this effect. Another reason for this discrepancy between expectation and measured result might be the not fully resolved issue of the double peak structure.

5.2.2 Conclusions

SQUID S4 shows similar effects resulting from the capacitive asymmetry as does SQUID S3. However, due to the not fully explained double peak structure the results were not unambiguous.

The double peak structure also complicated the estimate of the effective temperature $1.5 \text{ K} \leq T \leq 2.1 \text{ K}$. Nonetheless, the temperature $T = 2.1 \text{ K}$ also extracted from the measurements on S3 seems to be an upper limit. The reason for the elevated temperature is electronic noise from the setup as already mentioned in the previous section.

Due to the high temperature the M \ddot{u} nchhausen effect, where MQT has to be the dominating process, is not possible. However, also at temperatures below the crossover temperature, the ratio $E_J/(\hbar\omega_p2)$ is too high to allow tunneling at bias currents much smaller than the critical current. Therefore, if the M \ddot{u} nchhausen effect should establish itself, the effect would not be as pronounced as predicted in Ref. [TGB09].

5.3 SQUID S2

S2 is designed to have a large inductance but small junctions ($L = 8 \text{ nH}$, $I_c = 600 \text{ nA}$). Assuming an effective temperature $T \approx 2 \text{ K}$ as extracted from the previous measurements, MQT is not the dominating process.

Nevertheless, this SQUID has something else to offer. The ratio of $E_J/k_B T \leq 10$ puts the light junction in another interesting regime, namely in the phase diffusion regime, that was described in Sec. 1.2.3. The question is now, whether phase diffusion can actually be observed and what it looks like in a 2D potential.

In Ref. [MLQ⁺05], the authors report on phase diffusion in SQUIDs with $\beta_L \ll 1$. This creates a strong coupling, which locks the two junctions closely together, thus making the SQUID behave like a single junction with tunable critical current. Since our SQUIDs have $\beta_L > 1$, phase diffusion in truly two dimensions can be examined.

5.3.1 $I(V)$ -characteristic

In Fig. 5.19, the $I(V)$ -curve is shown and the strongly decreased switching current compared to the critical current $2I_c$ due to thermal fluctuations becomes obvious. When looking more closely at the superconducting branch (inset in Fig. 5.19), a small deviation from $V = 0$ can be observed for $I > 0$. This is a typical feature of the $I(V)$ -curve in the phase diffusion regime.

In Tab. 5.3 the designed and measured parameters of the S2 are listed. $V_{\text{gap}} = 2.7 \text{ mV}$ agrees perfectly with the gap values measured in Ref. [DSZN05] and the deviation of 4% of the measured critical current value from the designed one is also well inside the specified range. The resistance that was extracted from the slope of the normal resistance branch of the $I(V)$ -curve corresponds to the normal resistance of the SQUID R_S and, assuming equal junctions, $R_S = R/2$. R is the normal resistance of the single junction.

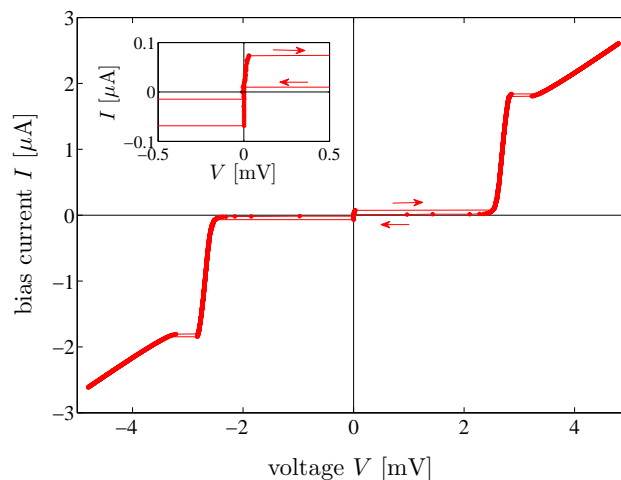


Fig. 5.19: $I(V)$ -curve of S2. The switching current is strongly suppressed. The inset shows a zoom to voltages $|V| < 500 \mu\text{V}$, where a small deviation from $V = 0$ of the superconducting branch is visible for currents $I > 0$.

	$2I_c$ [μA]	R_S [Ω]	k	$\omega_{p1}/(2\pi)$ [GHz]	$\omega_{p2}/(2\pi)$ [GHz]	Q_1	Q_2
measured	1.17	1840	0.07	6.5	119	155	7.6
designed	1.12	-	0.07	6.5	119	-	-

Table 5.3: Measured and designed SQUID parameters of S2. $Q_1 = \omega_{p1}C_1R$ and $Q_2 = \omega_{p2}C_2R$ are the quality factors of junction 1 and junction 2, respectively.

Using a 12 GHz Agilent oscilloscope in the fast acquisition mode and sampling $I(V)$ -curves over 8 s while the current is ramped from $I = 0$ to $I = I_{\text{sw}}$ at a ramping rate $\dot{I} = 0.33 \text{ mA/s}$ and a repetition rate of 1 kHz, yielded the image presented in Fig. 5.20.

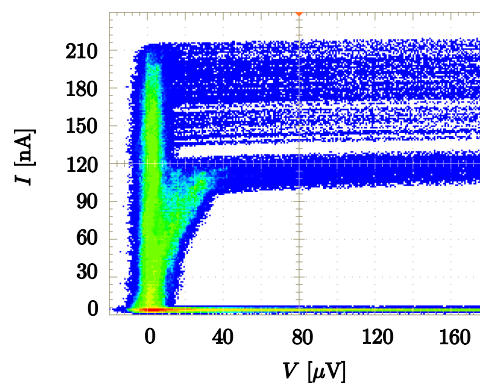


Fig. 5.20: Order of 10^4 $I(V)$ -curves of S2. Zoom to voltages $V < 160 \mu\text{V}$

Contrary to a first guess there are two branches. One of them shows phase diffusion and has a lower switching current than the other one that does not show any deviation from $V = 0$.

Due to low switching current $I_{\text{sw}}/(2I_c) \approx 0.1$ (a table listing the different currents can be found in Appendix C) the escape rates in 2D as introduced in Sec. 1.3.2 cannot be applied. They are only valid for currents close to the critical current.

5.3.2 Current Ramp Measurements

The current ramp measurements were taken at a ramping rate $\dot{I} = 0.33 \text{ mA/s}$ and 1000 ramping events were taken per second. The resulting current ramp histograms shed more light on the actual processes and together with the numerical results the behavior of the system becomes clear.

Phase Diffusion

When measuring histograms, the typical indicator for the phase diffusion regime is the dependence of the histogram width σ on temperature $\partial\sigma/\partial T < 0$. In Fig. 5.21, histograms recorded at different temperatures and zero applied flux as well as the temperature dependence of the standard deviation of the sharp peak is shown.

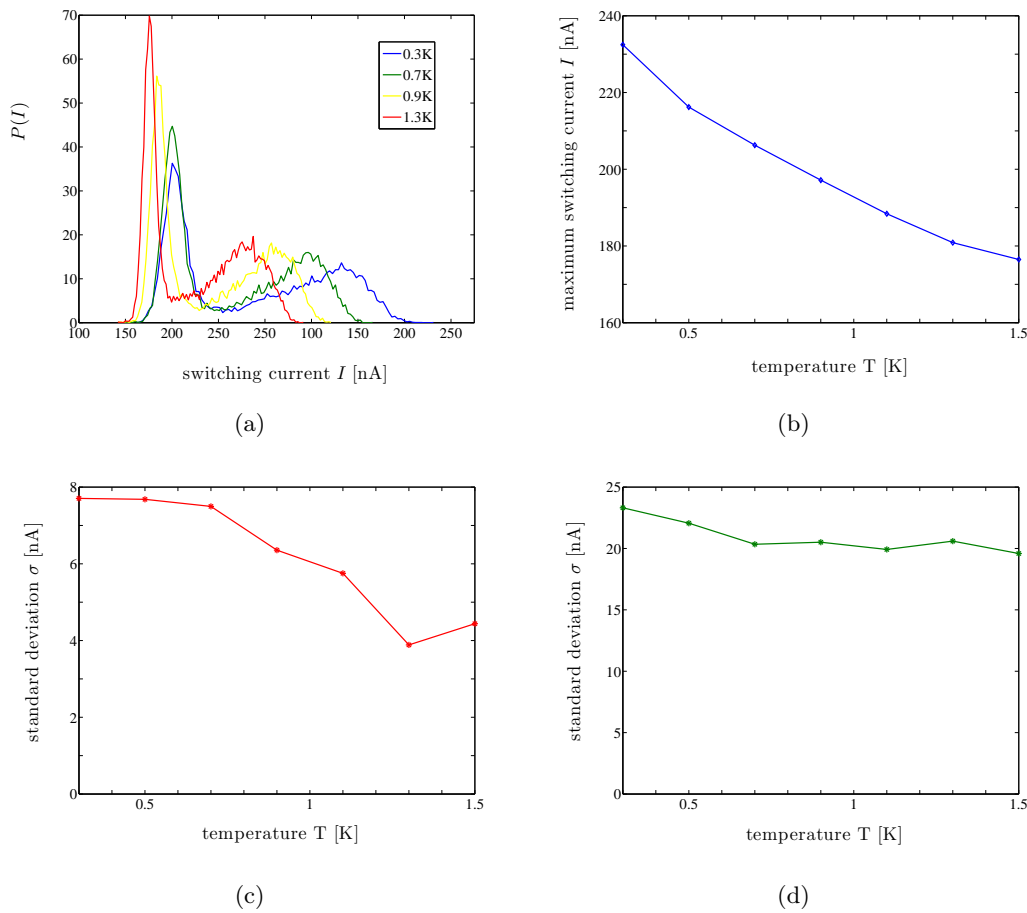


Fig. 5.21: (a) Histograms measured at temperatures $T_b = 0.3, 0.7, 0.9$ and 1.3 K . The temperature corresponds to the temperature T_b measured by the RuO-thermometer of the cryostat. (b) Temperature dependence of the switching current. The maximum nonzero value of the corresponding histogram is plotted. (c) Temperature dependence of the standard deviation σ of the sharp peak. (d) Temperature dependence of the standard deviation of the broader peak at higher currents.

The switching current decreases with increasing temperature as expected (in Fig. 5.21 the maximum nonzero value of the histogram is plotted) and especially the sharp low-current peak

is strongly affected by phase diffusion while $\partial\sigma/\partial T$ of the broader peak is hardly noticeable. This suggests that the two peaks correspond to different escape mechanisms.

Double Peak Structure

The above observation is supported by the numerical simulation, as will be shown later. First, in order to understand the double peak structure of the histograms, it is helpful to look once more at the 2D potential as given in Fig. 5.22. The φ_2 -axis corresponds to the phase difference across the unshunted junction. The effective mass of the phase particle is small in that direction. The phase difference across the shunted junction is represented by φ_1 and the effective mass of the particle in φ_1 -direction is large.

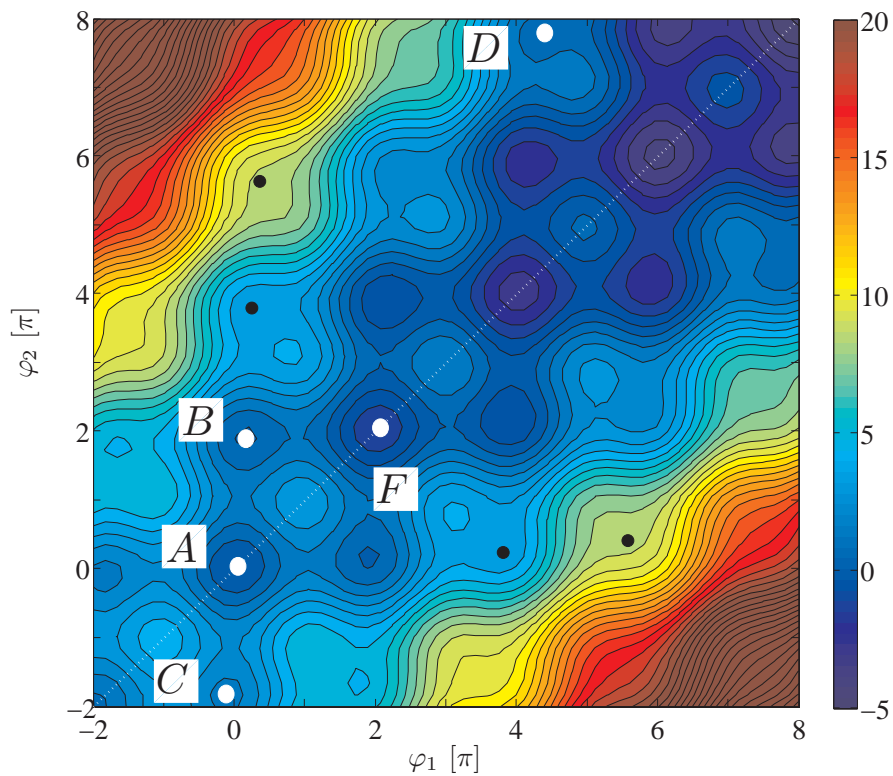


Fig. 5.22: Two dimensional potential for $k = 0.07$, $j = 0.1$ at $\phi_e = 0$

At zero current there are three different minima, the particle can be trapped in. They are denoted by A at $(0, 0)$, B at $(0, 2\pi)$ and C at $(0, -2\pi)$ in Fig. 5.22. Minima that are farther away from the bisectrix (dashed white line in Fig. 5.22) are illustrated by small black circles. They are metastable but in the temperature range considered here the barrier height $U_0(0)$ is smaller than the amplitude of the thermal fluctuations. Therefore, if the particle is retrapped in either one of them, it escapes already at $j \approx 0$ either to A , B or C , where it is retrapped.

Once the bias current is increased, the potential is tilted along the bisectrix. This means, that the minimum F is energetically below minimum A . However, the local potential landscape for minimum F is the same as for minimum A , i.e. the barrier blocking the motion of the particle that is localized in either one of the minima is the same for both. The same applies for any

minimum that can be obtained by a simple translation along the bisectrix.

If the particle is localized in the main minimum A , it stays there until the increase in bias current is sufficient to escape via TA. As $E_J/(k_B T) \leq 10$ this is possible already at bias currents that are considerably smaller than the critical current $I_0^{(0)}$ (a list of the nomenclature of the different currents can be found in Appendix C) and the phase particle starts to run down the potential. This process is illustrated in Fig. 5.23(a).

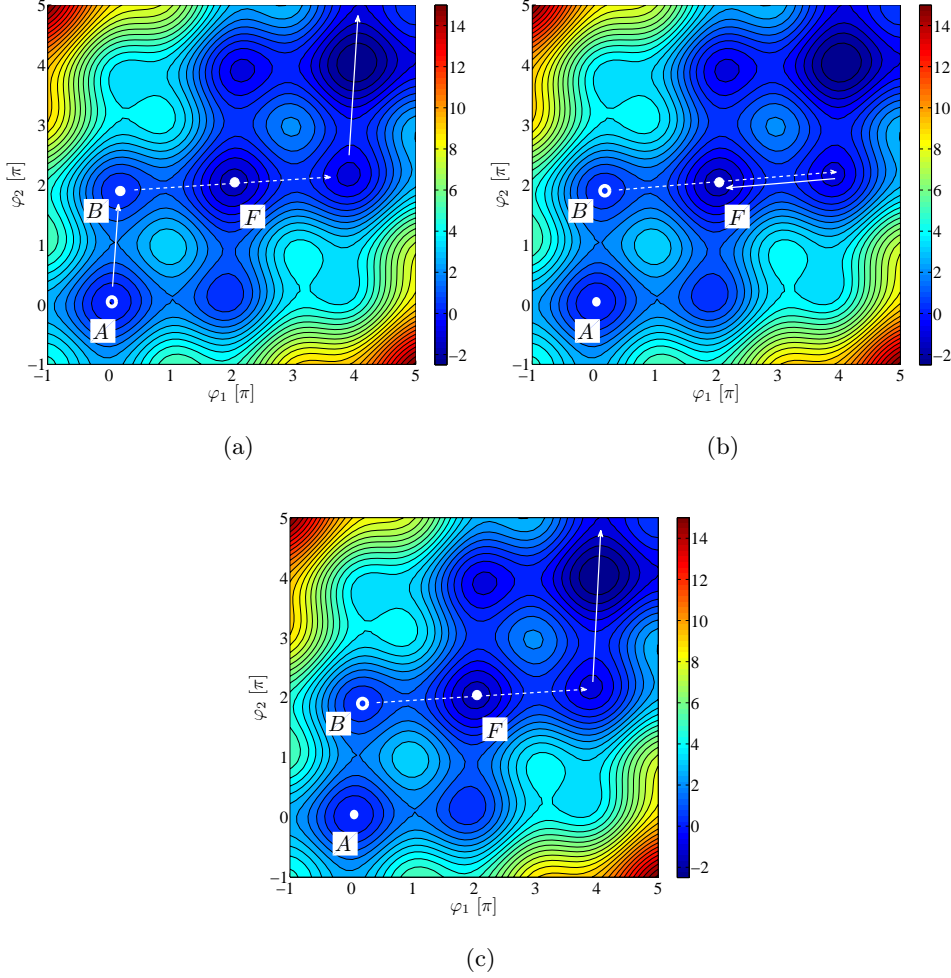


Fig. 5.23: Different escape scenarios. The open circle denotes the respective start minimum. Explanations are given in the text.

If the particle is trapped in B , the barrier it has to overcome is smaller than when starting in A . Therefore it can escape at a smaller bias current. And since (cf. Fig. 5.22) the barrier separating B from F is higher than the barrier between F and the minimum close to $(4\pi, 2\pi)$, it can run through the minimum in F and reach $(4\pi, 2\pi)$. If fate is against the escape, the motion in φ_2 -direction is negative and the particle runs up against the mountain, loses all its kinetic energy, turns back across the barrier and is retrapped in the minimum at F (cf. Fig. 5.23(b)). As mentioned before, F is physically the same situation as A . The particle stays there until the escape condition as described above for A applies.

If the odds are in favor for escape and the motion in φ_2 -direction is positive, then the moment of inertia carries the particle on in positive φ_1 -direction, while on a much shorter time scale

it moves across several minima in φ_2 -direction. It finds itself now in point D (cf. Fig. 5.22), where the path in φ_1 -direction is only blocked by a small barrier that can be overcome by TA or kinetic energy. Running across the following potential landscape the particle gains enough kinetic energy in φ_1 -direction to continue its journey without being stopped by a negative motion in φ_2 -direction, since its moment of inertia is large enough. The beginning of this escape process is depicted in Fig. 5.23(c).

The last possibility, i.e the particle being localized in C results in escape either from A or from B . It leaves its minimum C already at small bias currents, moves then across A until it is retrapped in B or falls back into the minimum at A . Since the effective mass in φ_2 -direction is much smaller than in φ_1 -direction, it has a very small moment of inertia and most probably cannot initialize the motion in φ_1 -direction.

From considering the above scenario, we can argue that the escape directly to the running state from the side minima like B where $\varphi_2 \approx \varphi_1 + 2\pi$ corresponds to the sharp peak at smaller bias currents. The escape from A (or F) leads to the broad peak at higher bias currents.

In order to test these predictions, the simulation described in Chapter 3 was used to study the evolution of the two phase differences in time. Histograms were generated by including a break condition corresponding to the threshold voltage in the current ramp measurements and repeating the simulation 200 times.

The results of the simulation for escape from points A and B of Fig. 5.22 are shown in Fig. 5.24 for $T = 0.7\text{K}$. This temperature is chosen to explain the basic properties of the results. Later the effect of higher temperature will be discussed.

In Fig. 5.24, the escape out of B happens at lower currents than the escape out of A as predicted. This can be verified by taking more statistics and generating switching current histograms for the escape out of the different minima. They are plotted in Fig. 5.25. The upper picture in Fig. 5.25 shows the histogram when starting in B . As explained above, sometimes the particle is retrapped in one of the minima along the bisectrix, which results in the small peak at higher currents. The peak at lower currents corresponds to the successful escape out of minimum B . The middle picture depicts the statistics for escape out of A and in the lower diagram the two curves are added together with a ratio 2 : 3. This ratio also results from the simulation when the time evolution of the particle after setting the bias current back to zero is monitored and its final state is recorded.

In Fig. 5.26 the behavior of the two variables φ_1 and φ_2 in the very small time interval where the actual escape happens is shown for the escape from A (left picture) as well as from B (right picture). Additionally, the velocities in the two directions are plotted. They are proportional to the voltage across the respective junction. In both cases, the escape starts with a phase diffusion like behavior in φ_2 -direction but the motion in φ_1 -direction is almost constantly accelerating. In the beginning the zigzag motion in 4π sized steps through the potential as described above is clearly visible. At some point the jumps and subsequent oscillations in φ_2 -direction cease to exist and the particle moves along the bisectrix $\varphi_1 = \varphi_2$. It has to be emphasized that Fig. 5.26 is a very strong zoom to the vertical line depicted as escape in Fig. 5.24.

However, when comparing simulated and measured histograms in more detail, one notices that first of all, the escape happens at currents that are much higher than in the experiment, where the voltage state occurs already at $j \approx 0.1$.

Second, in Fig. 5.27 the time evolution of the velocities $\dot{\varphi}_1$ and $\dot{\varphi}_2$ is plotted. It can be understood as an $I(V)$ -curve where current and voltage axis are exchanged. The simulation shows for both events (escaping from A or from B) the same resistive branch (black dashed line) that corresponds to the normal resistance $R_{\text{SQUID}} = 1822\ \Omega \approx R_S$ of the SQUID. Thus, although being able to explain the two different peaks, so far the simulation does not reproduce

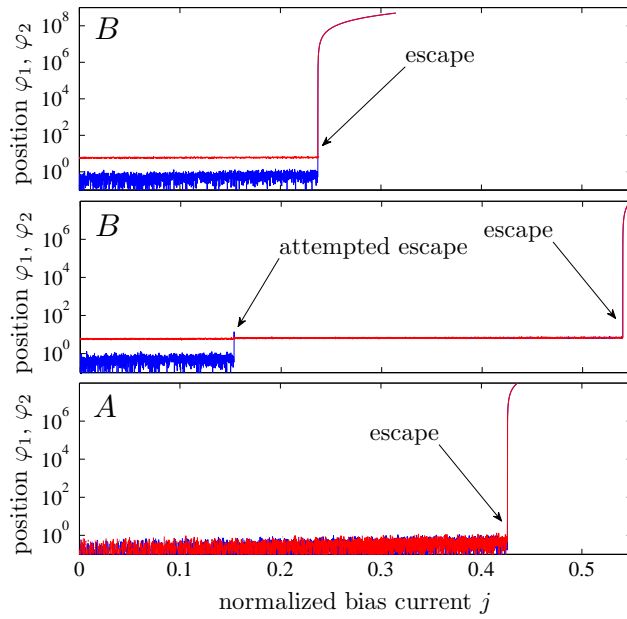


Fig. 5.24: Results of the simulation for the time evolution of φ_1 (blue lines) and φ_2 (red lines) for the escape out of minimum B that was successful (upper diagram) and unsuccessful (middle). The blue line (φ_1) in the middle picture does not vanish after the attempted escape, instead the red line is printed above it. The escape out of A is shown in the lower diagram.

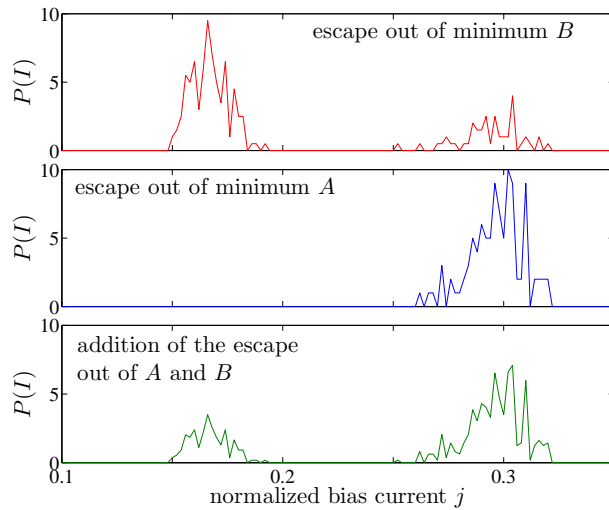


Fig. 5.25: Histograms generated by the simulation. The upper picture shows the probability distribution of the escape out of B , the middle picture corresponds to the escape out of A and the lowest picture is the sum of the two, weighted according to the retrap probability: 40% being retrapped in B and 60% being retrapped in A .

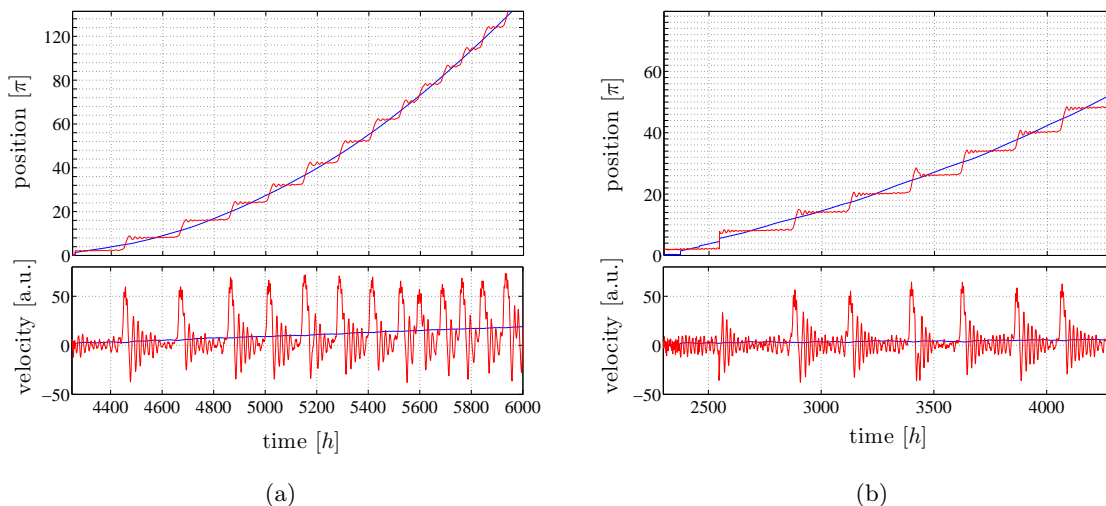


Fig. 5.26: Zoom to the “moment” of escape from A (a) and B (b). The respective upper picture shows the values of φ_1 (blue) and φ_2 (red), the lower picture the velocities $\dot{\varphi}_1$ (blue) and $\dot{\varphi}_2$ (red).

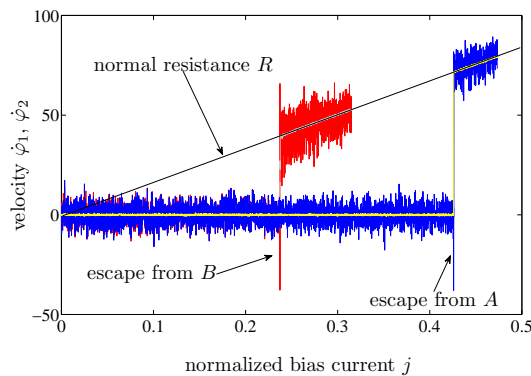


Fig. 5.27: Velocities $\dot{\varphi}_1$ and $\dot{\varphi}_2$ for the escape from B ($\dot{\varphi}_1$ in grey, $\dot{\varphi}_2$ red) and escape from A ($\dot{\varphi}_1$ yellow, $\dot{\varphi}_2$ blue). The black line depicts $\dot{\varphi} = \gamma \cdot Rj$ where $\gamma = 4I_c e / (\hbar \omega_p)$ contains the prefactors due to normalization.

phase diffusion in the sense of a measurable small voltage branch before switching.

To observe phase diffusion, i.e. a branch with $\dot{\varphi} > 0$ but with a smaller resistance than the normal resistance branch, within the simulation, a few tricks have to be performed. For one thing, a higher temperature, e.g. $T = 1.0$ K is necessary, which allows for an escape at lower bias currents. The problem hereby is the decreased stability of the side minimum B . If the particle is localized in B the elevated temperature causes the particle to escape out of B at currents that are so small that the particle is always retrapped in the main minimum A (or F). Therefore, only the escape at higher currents would be observed with the simulation. In order to circumvent this, the system is prepared artificially in the minimum close to $(\varphi_1, \varphi_2) = (0, 2\pi)$ at some current $j > 0$ which is close the current where escape is possible without being retrapped.

This and the fact that even with increased temperature the simulated switching current is still higher than the one measured indicates that the simulation does not take into account the whole physical system. For example, in the simulation the damping is assumed constant and derived from the normal resistance of the system, but for higher frequencies such as ω_{p2} the

impedance of the lines has to be considered as already mentioned in Sec. 1.2.3. This would result in a higher damping, which could stabilize the particle in one of the side minima at higher temperatures.

In Ref. [KFU04] an expression for the $I(V)$ -dependence of the phase diffusion branch is derived.

$$I_{\text{pd}} = I_c Q \frac{V_p}{(V^2) + (\delta V_p)^2} \quad (5.2)$$

In our case, I_c is the critical current for the minimum D in Fig. 5.22, because, as shown by the simulation (cf. Fig. 5.26), those are the minima in which the particle is retrapped in φ_2 -direction. Q is the damping parameter, $V_p = \Phi_0 \omega_p / (2\pi)$ and δ is connected to the high frequency impedance via $Z = \delta V_p \Phi_0 / (2\pi k_B T)$. Fitting Eq. (5.2) to our data with Q and δ as fit parameters (cf. Fig. 5.28) yields $Q = 0.097$, which is almost two orders of magnitude smaller than for the low frequency damping, and $\delta = 0.13$ which translates into a high frequency impedance $Z \approx 400 \Omega$ (where $T = 2 \text{ K}$ was used). Thus, the damping used in the simulation is in fact too small to reproduce phase diffusion accurately.

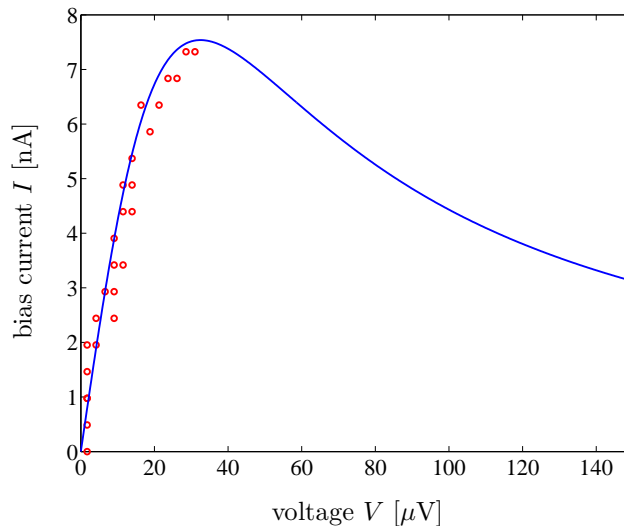


Fig. 5.28: Phase diffusion branch of the measured $I(V)$ -curve in Fig. 5.19 (red circles) and fit using Eq. (5.2) (blue line).

This explains why Fig. 5.29, where only $\dot{\varphi}_1$ and $\dot{\varphi}_2$ are plotted, agrees only qualitatively with the expectations. In the phase diffusion branch, the particle oscillates in φ_2 -direction, which creates the phase diffusion and hinders the motion in φ_1 -direction. However, the switching current in the simulation $I_{\text{sw}} = j_{\text{sw}} \cdot 2I_c \approx 240 \text{ nA}$ is considerably higher than the results measured from $I(V)$ -curves and current ramp histograms and so are the corresponding voltage and resistance values.

Repeating this simulation several times shows that the current value at which the system switches to the phase diffusion branch varies strongly, due to the thermal fluctuations while the escape from phase diffusion to V_{gap} varies only slightly. This indicates that the final escape is not a thermally triggered effect but happens once a critical velocity, i.e. voltage, is reached.

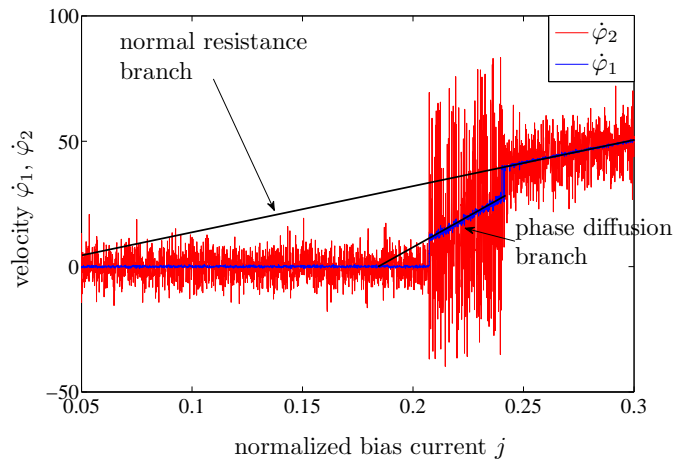


Fig. 5.29: Results of the simulation for $T = 1$ K with φ_2 set from its value $\varphi_2 \approx 0$ to $\varphi_2 \approx 2\pi$ artificially at $j = 0.207$. The phase diffusion branch is clearly visible. Note that $\dot{\varphi}_1 > 0$ while φ_2 oscillates strongly.

Flux Dependence

In this last part the flux dependence of the histograms is evaluated. As already mentioned in the beginning of this section, the flux dependence is very weak, but nonetheless observable. In Fig. 5.30, the maximum none zero value of each histogram is plotted. The roughness of the curve is due to the strong thermal fluctuations.

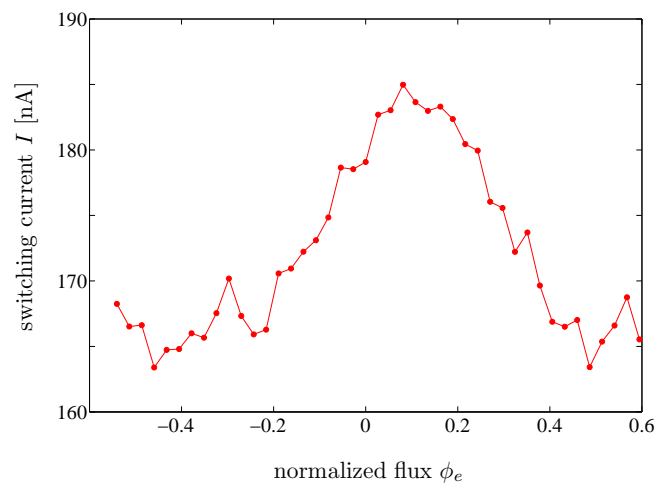


Fig. 5.30: Flux dependence of S2. The last nonzero value of each histogram is plotted.

For the sake of clarity, only the histograms with maximum (red) and minimum (blue) switching current are plotted in Fig. 5.31. As expected, the broader peak that corresponds to the thermal escape out of the main minimum A has its maximum switching current value at $\phi_e \approx 0$ and shifts to smaller current values with ϕ_e decreasing or increasing.

The sharp peak corresponds to the escape out of B (first to the phase diffusion state and from there to V_{gap}). Since B is a side minimum, it should become more stable with negative

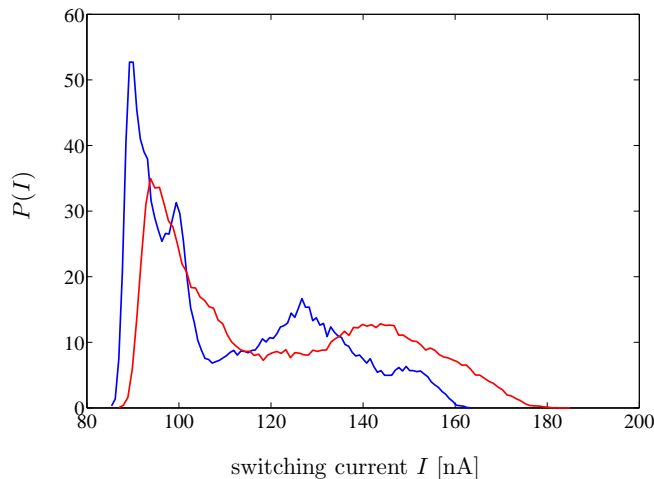


Fig. 5.31: Histograms at different flux values $\phi_e = 0$ (red) and $\phi_e = -0.5$ (blue).

flux and less stable for positive flux values or vice versa. But, contrary to those expectations, the sharp peak follows the motion of the broad peak but with lower amplitude.

The reason for that can be found in the experimental definition of the escape: The voltage that triggers the stop signal in the measurement is considerably higher than the voltage that occurs in the phase diffusion regime. Therefore, not escape out of B to the phase diffusion state is recorded but the switching from phase diffusion to $V = V_{\text{gap}}$. Thus, not the removal of the barrier of one specific minimum changes the switching current. Instead, in general the fact, that the particle that follows the optimal trajectory in the potential has to overcome smaller barriers for nonzero flux than at zero flux, defines the switching. As a result the critical velocity is reached at a smaller bias current.

5.3.3 Conclusions

SQUID S2 shows a switching current that is almost an order of magnitude smaller than the critical current. The reason for that is the ratio $E_J/(k_B T) \leq 10$. The existence of a phase diffusion regime is proven and we were able to explain the double peak structure of the histograms by two different escape scenarios, which is also supported by $I(V)$ -measurements and the flux dependence of the histograms.

Due to the elevated temperature the escape process is dominated by TA. However, assuming lower temperatures the ratio $E_J/(\hbar\omega_p2) \approx 2$ suggests that the tunneling rate might be appreciable already at small bias currents. Therefore, it should be possible to observe the Münchhausen effect in this SQUID.

Conclusions and Outlook

In this thesis, capacitively asymmetric dc-SQUIDs with large loop inductance were studied. Starting from the objective of testing the Münchhausen effect which was introduced in Chapter 2, current ramp measurements were performed on SQUIDs with different parameters and for different magnetic flux values. Common to all tested SQUIDs is a large inductance of the individual SQUID loop, resulting in a weak coupling between the two Josephson junctions. Additionally, a large shunting capacitor is installed close to one of the junctions. The latter ensures that the shunted junction behaves classically even when the unshunted junction resides in the quantum mechanical regime.

In order to gain a better understanding of the system, the picture of a phase particle in a two dimensional and - depending on the coupling strength of the two junctions - rather undulating potential was applied and used throughout this work. A picture of such a potential can be found in Fig. 1.7. One axis in the potential corresponds to the phase difference across one junction and the perpendicular direction represents the phase difference across the other. Due to the different effective capacitances of the two junctions, the particle behaves differently in the two directions.

The experimental results of $I(V)$ -characteristics and current ramp measurements were presented and investigated for three different SQUIDs.

The results indicate, that the SQUIDs S3 and S4 both behave according to classical theory. Their switching to the finite voltage state is determined by thermal activation. The evaluation of the histograms and escape rates indicates an effective temperature between $T \approx 1.5$ K and $T \approx 2.1$ K. This large difference between phonon temperature of the cryostat $T_b \approx 300$ mK and the measured effective temperatures can be explained by external noise from the electronic setup which is coupling to the SQUIDs.

We have shown that the Münchhausen effect is not and probably cannot be observed as predicted in those two SQUIDs, even at lower temperatures. In order to observe the Münchhausen effect, macroscopic tunneling should occur already at bias currents much less than the critical current. However, SQUIDs S3 and S4 have comparatively large junctions. Therefore, the ratio $E_J/(\hbar\omega_p)$ allows macroscopic quantum tunneling with an appreciable rate only for currents close to the critical current.

Nonetheless, measurements on both SQUIDs displayed a behavior that was ascribed to two different, direction dependent, effective masses of the phase particle. The difference between these masses was noticeable in the flux dependence of the minor peaks, that result from the escape out of a side minimum of the potential. Additionally, a small relative shift between histograms measured for different polarities but the same absolute values of flux could be observed. Although, for S4 this effect was not unambiguous, it was shown that for S3 this shift was due to the different attempt frequencies in the different escape directions.

SQUID S2 showed two qualitatively different mechanisms of switching to the voltage state. One of those mechanisms is thermal activation and there is strong evidence for interpreting the

other as escape via the phase diffusion regime. Thus, these two very different regimes were for the first time shown to be present simultaneously in one device.

Using numerical simulations the phase diffusion branch could be qualitatively reproduced. The simulation integrates the coupled differential equations within the RCSJ-model including a thermal noise term. The agreement of numerical with experimental results can only be qualitative as the RCSJ-model does not incorporate frequency dependent damping. All the more, it is quite surprising that phase diffusion is reproduced at all. This is only possible because two junctions instead of only one are considered. The large capacitor shunting one of them damps intrinsically the evolution of the other junction.

The simulation shows that the two different escape channels correspond to the different initial positions of the phase particle in the two dimensional potential: Starting from the more elevated side minimum leads to phase diffusion while being (re)trapped in the deeper minimum results in escape via switching to the running state.

We would expect that for this SQUID the Münchhausen effect should be observable. However, due to effective temperatures close to $T \approx 2$ K in the experiment, macroscopic quantum tunneling of the unshunted junction is not a dominating process. Nonetheless, at lower temperatures tunneling should be appreciable already at bias currents considerably below the critical current.

Outlook

Although the results of the measurements on SQUIDs S3 and S4 showed interesting and consistent results, they raise a few issues that should be examined further. For instance, the effect of the different plasma frequencies in the two orthogonal directions could be quantified. One way to realize this is to prepare the system to start always from the same minimum and examine the minor and major parts of the histograms separately. Additionally, the physical noise source which elevates the effective temperature should be investigated and removed, if possible.

In what concerns SQUID S2, the examination of phase diffusion in two dimensions could produce intriguing results. A more detailed investigation of the high frequency properties of the shunting capacitor and the transmission line impedance should be included. The experimental settings for the Münchhausen effect is not yet optimal in this circuit. At temperatures attainable in a dilution refrigerator, macroscopic quantum tunneling would be the dominating escape mechanism and tunneling would be appreciable already at relatively small bias currents. In this case the Münchhausen effect should be observed. It will be interesting to see if and how experiment and theoretical predictions agree.

Appendix A

Chip and Sample Design

In Fig. A.1 an example of a designed chip (chip AF42) is displayed. Each chip has a size of $9 \times 9 \text{ mm}^2$ and the four SQUIDs are arranged around the center structure. This center structure is not connected to the experiments presented in this work and may differ from chip to chip. However, the arrangement of the SQUIDs is always the same. Two SQUIDs are placed on opposite sides of the chip and share a common flux line. In this way the number of necessary electrical lines is reduced.

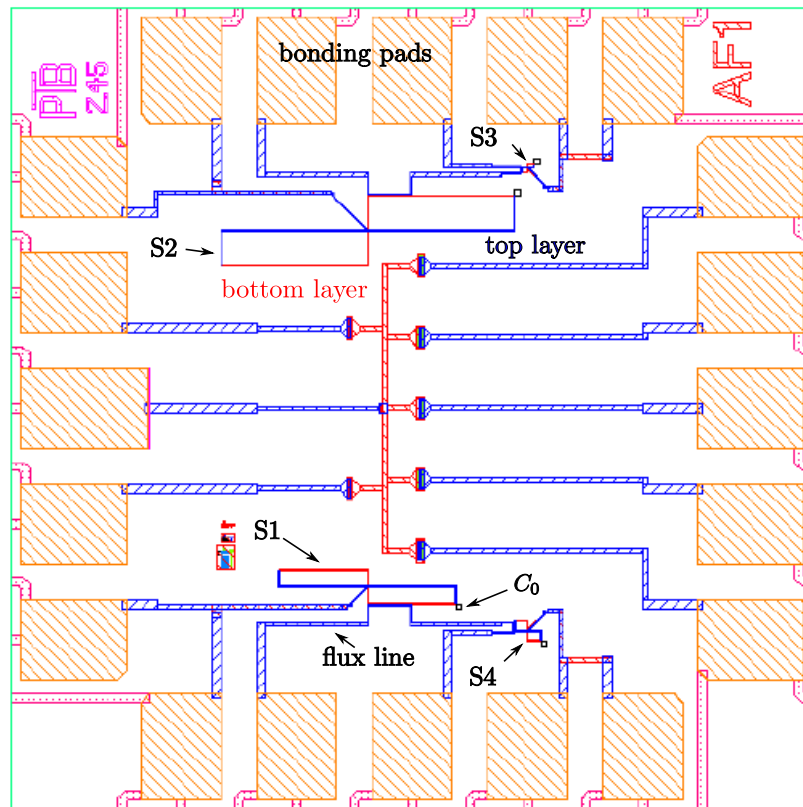


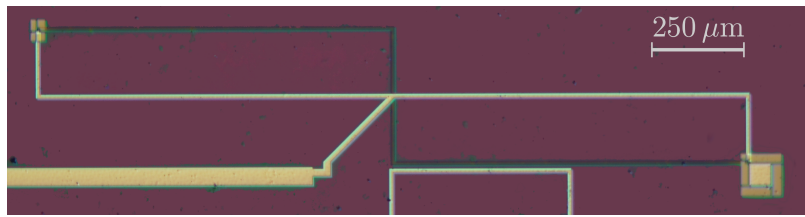
Fig. A.1: Layout of chip AF42. The four different SQUIDs are indicated by arrows. The structures in the center of the chip are not of interest for this thesis. Red lines and areas correspond to the bottom layer and blue areas and lines to the top layer. The bonding pads are colored orange. The little black square in one corner of each SQUID depicts the shunting capacitance C_0 (not to scale).

Blue areas and lines correspond to the top layer, red areas to the bottom layer. Both layers are made from Nb of 150 nm thickness. In the junction area, in between the two layers there is a very thin isolating barrier of 10 nm thickness of Al/ AlO_x . The leads to the SQUIDs partially

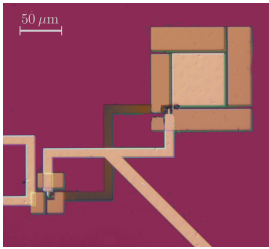
run on top of each other. In this case bottom and top layer are isolated against each other with a thin layer of NbO_5 and a thick layer ($\sim 150 \text{ nm}$) of SiO_2 . In one corner of each SQUID a small black square can be found. It depicts the position of the shunting capacitor C_0 but does not shown the capacitor to scale.

It is clearly visible that the loop sizes, i.e. the inductances are different for each SQUID. The two large inductance SQUIDs S1 and S2 have a single junction area of $0.2 \times 0.2 \mu\text{m}^2$ while the small inductance SQUIDs S3 and S4 have a single junction area of $0.5 \times 0.5 \mu\text{m}^2$. The width of the lines that form the SQUID is $10 \mu\text{m}$.

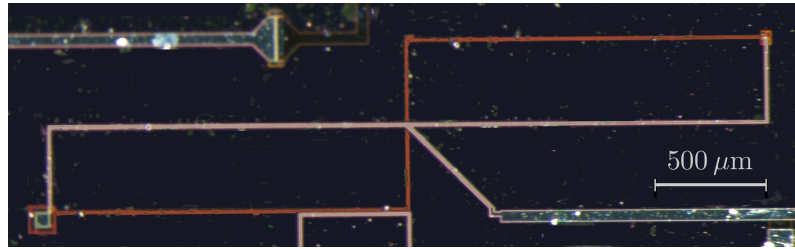
Optical microscope images of S1, S2 and S3 are presented in Fig. A.2. S4 is shown already in Sec. 4.1 including zooms to the two junctions.



(a) SQUID S1



(b) SQUID S3



(c) SQUID S2

Fig. A.2: Optical microscope images of S1 (top), S3 (bottom left) and S2 (bottom right).

The picture of S2 looks different, because it was too big to fit even in the smallest magnification objective of the upright optical microscope. A stereo optical microscope had to be used instead which has a smaller magnification but a larger field of view.

Appendix B

Measurement Setup

Current Ramp Measurement

The schematics of the experimental setup for the current ramp measurement is presented in Fig. B.1.

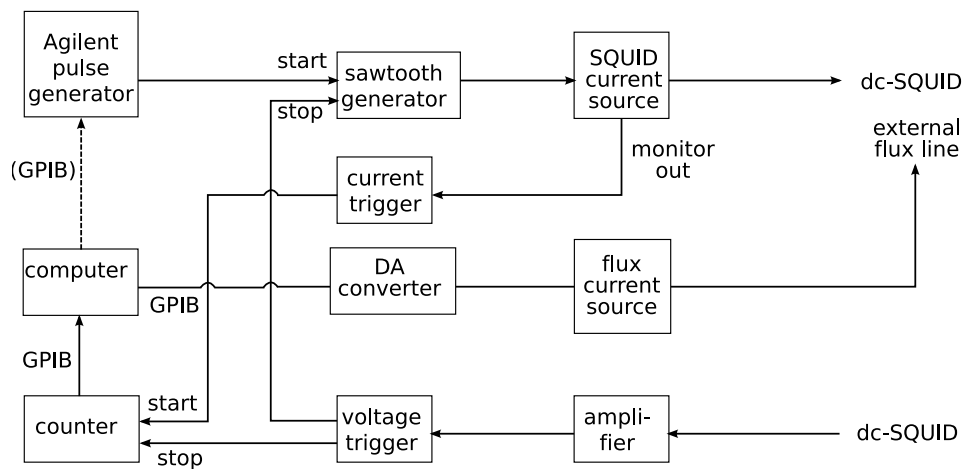


Fig. B.1: Measurement setup for current ramp measurements.

A sawtooth current generator with adjustable offset and ramping rate \dot{I} modulates the current of the current source. Additionally, the generator has two trigger inputs for the start and the stop signal. During the relaxation time the SQUID is biased with a small negative current. The value of this current is chosen to be small enough so that the SQUID does not switch to the voltage state for any flux value. The Agilent pulse generator delivers a start signal for the ramp generator with a repetition rate that is either defined by the MATLABTM measurement software or adjusted by hand directly at the pulse generator. The current is ramped with a constant rate. Once it crosses $I = 0$, a trigger signal starts the counter.

The voltage across the SQUID is measured and as soon as this voltage crosses a set threshold voltage ($V_{th} \approx 600 \mu\text{V}$)¹ a trigger signal stops counter and current ramp. The current is set back to its relaxation value.

The counter measures the time Δt between the start and the stop signal. The switching current is then calculated by the data acquisition software which is provided with the ramping rate \dot{I} . The measurement software also controls the current source for the flux line that produces the flux bias for the SQUID if needed. More details on the measurements setup can be found in Ref. [WLC⁺03].

¹The threshold voltage could be adjusted between 50-600 μV

Current Dividers

In order to build a current divider, metal-film resistors were soldered between the respective lines. In Fig. B.2 a schematic of the setup can be found. The resistors have a room temperature resistance of $R_1 = 10\text{ k}\Omega$ and $R_2 = 1\text{ k}\Omega$ which results in a ratio $I_1/I_2 = 1/11$.

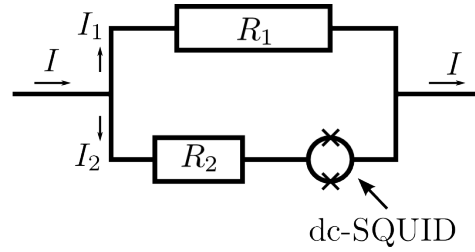


Fig. B.2: Schematic of the current divider including the dc-SQUID

Appendix C

Nomenclature of Critical Currents

notation	description	introduced on
I	bias current through the junction/dc-SQUID	p. 4
I_c	critical current of the Josephson junction	p. 4
j	normalized bias current $j = I/I_c$ (single junction) and $j = I/(2I_c)$ (dc-SQUID)	p. 5 and p. 10
I_r	retrapping current at which the energy gained between two adjacent maxima in the washboard potential is equal to the energy dissipated	p. 6
$I_0^{(n)}(\Phi_e)$	critical current of the SQUID corresponding to the n -th minimum and depending on external magnetic flux Φ_e	p. 12
$j_0^{(n)}$	$I_0^{(n)}/(2I_c)$	p. 14
I_{sw}	switching current of the system	p. 15
$j_{c,n}^+$	normalized current at which tunneling to the n -th minimum in φ_2 -direction becomes possible ¹	p. 20
$j_{c,n}^-$	normalized current at which the barrier of the minimum close to $(0, 2\pi n)$ vanishes in φ_1 -direction ^{1,2}	p. 20
j_c^{eff}	normalized effective critical current due to the Münchhausen effect composed of $j_{c,n}^+$ and $j_{c,n}^-$ ¹	p. 20

Table C.1: Nomenclature for the different specific currents.

¹The real current I_c^\pm can be obtained by $I_c^\pm = j_c^\pm \cdot 2I_c$.

²Analytical approximation of j_0^n

Zusammenfassung

Experimente mit asymmetrischen dc-SQUIDs - auf der Suche nach dem Münchhausen Effekt

In dieser Arbeit wurden kapazitiv asymmetrische dc-SQUIDs mit großen Induktivitäten untersucht. Ein SQUID (Superconducting QUantum Interference Device) besteht entweder aus zwei parallel geschalteten Josephson Kontakten (dc-SQUID) oder aus einem supraleitenden Ring, der von nur einem Josephson Kontakt unterbrochen ist (rf-SQUID). Im Folgenden werden nur dc-SQUIDs betrachtet. Der kritische Strom eines SQUIDs ist durch den Strom gegeben, bei dem das SQUID vom supraleitenden Zustand (Nullspannungszustand) in den Spannungszustand umschaltet. In diesem Fall ist die Phasendifferenz über den Josephson Kontakten nicht mehr konstant. Da ein externer magnetischer Fluss durch den SQUID-Ring die Stromverteilung in den beiden SQUID-Armen beeinflusst und damit auch den Strom, der durch die einzelnen Kontakte fließt, ist der kritische Strom des dc-SQUIDs vom externen Fluss abhängig.

Das System kann als virtuelles Phasenpartikel in einem zweidimensionalen Potential verstanden werden. Ein solches Potential ist in Fig. 1.7 dargestellt. Die eine Achse des Potentials bezieht sich auf die Phasendifferenz φ_1 über Kontakt 1, die andere Achse beschreibt die Phasendifferenz φ_2 über Kontakt 2. In diesem Bild entsprechen die Kapazitäten der einzelnen Kontakte der effektiven Masse des Teilchens in den orthogonalen Richtungen. Im Nullspannungszustand ist das Phasenteilchen in einem Minimum lokalisiert und oszilliert in diesem Minimum mit der sogenannten Plasmafrequenz.

In Ref. [TGB09] wurde von V. Geshkenbein, A. Thomann und G. Blatter die Idee vorgestellt, dass ein klassisches Teilchen ein metastabiles Minimum auch am absoluten Nullpunkt ($T = 0\text{ K}$) verlassen kann, vorausgesetzt es ist an ein sich quantenmechanisch verhaltendes Teilchen gekoppelt. Da dieses Verhalten an Baron Münchhausen erinnert, der behauptete sich selbst (und sein Pferd) an seinen eigenen Haaren aus dem Sumpf gezogen zu haben, wurde dieser Prozess „Münchhausen“ Effekt genannt.

Experimentell kann ein solches System mit einem dc-SQUID realisiert werden. Einem der beiden Kontakte wird ein großer Kondensator parallel geschaltet. Im Folgenden wird dieser Kontakt als Kontakt 1 bezeichnet. Diese große Kapazität nahe einem der beiden Kontakte bewirkt, dass sich die Phasendifferenz über diesen Kontakt klassisch verhält. Falls die intrinsische Kapazität des Kontaktes ohne parallelen Kondensator (im Folgenden als Kontakt 2 bezeichnet) klein genug ist, zeigt die Phasendifferenz über diesem Kontakt quantenmechanisches Verhalten. So zum Beispiel die Fähigkeit durch eine Potentialbarriere zu tunneln.

Am absoluten Nullpunkt kann das Teilchen ein Minimum in φ_1 -Richtung erst verlassen, wenn die Potentialbarriere in dieser Richtung vollständig verschwunden ist. Nichtsdestoweniger ist Tunneln in φ_2 -Richtung möglich, sobald das benachbarte Minimum energetisch unterhalb des momentan besetzten Minimums liegt. Nach dem Tunnelprozess in φ_2 -Richtung befindet sich das Phasenteilchen im benachbarten Minimum, bei dem die Potentialbarriere in φ_1 -Richtung entweder bereits nicht mehr vorhanden oder aber in jedem Fall verkleinert ist. Der effektive

kritische Strom, der in diesem Fall den Nullspannungs- vom Spannungszustand trennt, ist somit niedriger als der kritische Strom des rein klassischen Systems.

Ziel dieser Arbeit ist die Überprüfung der in Ref. [TGB09] gemachten Voraussagen und die Erprobung weiterer Eigenschaften dieses dynamisch asymmetrischen Systems. Eine der Voraussetzungen für die Beobachtung des Münchhausen Effekts ist die schwache Kopplung der beiden Kontakte. Es ermöglicht unter anderem allerdings auch die Untersuchung von Phasendiffusion in zwei Dimensionen. In Ref. [MLQ⁺05] wurde Phasendiffusion in dc-SQUIDs beobachtet, allerdings waren die beiden Kontakte der betrachteten SQUIDs stark gekoppelt wodurch sich diese SQUIDs wie ein eindimensionales System.¹

Vier kapazitiv asymmetrische dc-SQUIDs mit unterschiedlicher Induktivität und unterschiedlichem kritischem Strom wurden entworfen und in der Physikalisch-Technischen Bundesanstalt (PTB) Braunschweig hergestellt. Um den Einfluss des Münchhausen Effekts auf den kritischen Strom der SQUIDs und dessen Flussabhängigkeit zu ermitteln, wurden an den SQUIDs Stromrampenmessungen durchgeführt. Dabei wurden bei variierendem magnetischen Fluss Histogramme aufgenommen, die der Wahrscheinlichkeitsverteilung des Stromes, bei dem das SQUID in den Spannungszustand umschaltet, entsprechen. Wegen thermischer Aktivierung und der Möglichkeit zu tunneln entspricht der tatsächliche "Umschaltstrom" nicht dem kritischen Strom, sondern liegt etwas darunter. Desweiteren verursachen thermische und quantenmechanische Fluktuationen eine Verbreiterung der Wahrscheinlichkeitsverteilung des Umschaltstroms.

Die experimentellen Ergebnisse der Stromrampenmessungen und Strom-Spannungskurven für drei unterschiedliche SQUIDs wurden ausgewertet und vorgestellt.

Für die SQUIDs S3 und S4 deuten die Ergebnisse darauf hin, dass sich beide SQUIDs klassisch verhalten. Thermische Aktivierung bestimmt das Umschalten zwischen dem Nullspannungszustand, in dem das Phasenteilchen in einem Minimum lokalisiert ist, und dem Zustand mit Spannungsabfall am SQUID, bei dem das Teilchen das Minimum verlassen hat und dem Potentialverlauf folgt. Die Auswertung der Histogramme und Schaltraten ergab eine effektive Temperatur zwischen $T = 1.5$ K und $T = 2.1$ im Kryostaten. Die recht große Diskrepanz zwischen der Phonontemperatur, die die Thermometer wiedergeben $T = 300$ mK und der effektiv gemessenen Temperaturen kann mittels elektronischem Rauschen aus dem Messaufbau, das an die dc-SQUIDs koppelt, erklärt werden.

Außerdem wurde gezeigt, dass der Münchhausen Effekt nicht beobachtet wurde und in den SQUIDs S3 und S4 auch nicht in dem Ausmaß wie theoretisch vorhergesagt beobachtet werden kann. Dafür müsste makroskopisches Tunneln bereits bei Strömen möglich sein, die deutlich kleiner als der kritische Strom sind. Allerdings ist das Verhältnis von Josephson Energie zu Plasmafrequenz $E_J/(\hbar\omega_p)$ so groß, dass das Tunneln mit nicht vernachlässigbarer Rate nur für Ströme nahe dem kritischen Strom erlaubt ist.

Nichtsdestoweniger, zeigten die Messungen an beiden SQUIDs ein Verhalten auf, das auf die unterschiedlichen effektiven Massen des Phasenteilchens in den beiden orthogonalen Richtung zurückzuführen ist. Hierbei unterschied sich zum einen die Flussabhängigkeit der Nebenstrukturen für positiven und negativen magnetischen Fluss. Die Nebenstrukturen entstehen dadurch, dass das Phasenteilchen nicht im tiefsten Minimum sondern in einem der Nebenminima lokalisiert war. Da die Potentialbarriere für diese Nebenminima kleiner ist, als für das Hauptminimum, fällt bereits bei deutlich kleineren Strömen eine Spannung am SQUID ab. Zum anderen

¹Außer für externe magnetische Flusswerte nahe ungeraden halbzahligen Vielfachen des Flussquantums.

konnte eine kleine Verschiebung zwischen Histogrammen festgestellt werden, die bei betragsmäßig gleichen positiven und negativen Flüssen aufgenommen wurden. Diese Verschiebung kommt dadurch zustande, dass positiver oder negativer magnetischer Fluss das Teilchen zwingt sein Minimum entweder in φ_2 - oder in φ_1 -Richtung zu verlassen. Da die Plasmafrequenzen in den orthogonalen Richtungen unterschiedlich sind, unterscheiden sich damit auch die Raten, mit denen das Teilchen sein Minimum verlässt. Für S4 war der Effekt nicht eindeutig auf die unterschiedlichen effektiven Massen zurückzuführen. Im Gegensatz dazu ließ sich für S3 zeigen, dass sich die Verschiebung zwischen den beiden Histogrammen entsprechend der Erwartungen mit zunehmendem Betrag des magnetischen Flusses vergrößerte.

Bei SQUID S2 konnten zwei qualitativ verschiedene Mechanismen beobachtet werden, wie das System zum Spannungszustand schaltet. Einer dieser Mechanismen ist wieder thermische Aktivierung und es konnte gezeigt werden, dass der andere Vorgang dem Umschalten zwischen Phasendiffusion und Spannungszustand entspricht.² Das bedeutet, dass diese sehr unterschiedlichen Mechanismen zum ersten Mal gleichzeitig im selben System beobachtet werden konnten.

Unter Verwendung numerischer Simulationen konnte der Phasendifusionszweig qualitativ reproduziert werden. Die Simulation integriert die gekoppelten Differentialgleichungen des RCSJ-Modells unter Berücksichtigung thermischen Rauschens. Die Übereinstimmung zwischen Simulation und experimentellen Ergebnissen kann nur qualitativ sein, da im RCSJ-Modell die Dämpfung nicht frequenzabhängig ist. Um Phasendifusion in unterdämpften Kontakten zu beobachten ist frequenzabhängige Dämpfung allerdings eine notwendige Voraussetzung. Umso mehr überrascht es, dass Phasendifusion mit der Simulation überhaupt reproduziert wurden. Der Grund dafür liegt darin, dass zwei gekoppelte Kontakte betrachtet werden. Die große Kapazität des parallelgeschalteten Kondensators dämpft intrinsisch das Verhalten des Kontaktes ohne zusätzlichen Kondensator.

Mit Hilfe der Simulation wurde außerdem noch gezeigt, dass die zwei unterschiedlichen Umschaltprozesse auf die verschiedenen Startpositionen des Phasenteilchens im Potential zurückzuführen sind: Wenn das Teilchen aus dem erhöhten Nebenminimum startet, führt das Verlassen des Minimums zu Phasendifusion. Befindet sich das Teilchen zu Beginn im Hauptminimum wird es das Minimum mittels thermischer Aktivierung verlassen und das System schaltet sofort zum Spannungszustand um.

Außerdem konnte festgestellt werden, dass in diesem SQUID der Münchhausen Effekt beobachtbar sein sollte. Wegen effektiver Temperaturen von $T \approx 2$ K im Experiment ist makroskopisches Tunneln nicht der dominierende Effekt. Bei niedrigeren Temperaturen sollte sich das ändern und die Tunnelrate bereits bei Strömen deutlich unterhalb des kritischen Stromes nicht vernachlässigbar sein.

Ausblick

Die SQUIDs S3 und S4 können noch weitergehend untersucht werden. So könnte zum Beispiel der Effekt der unterschiedlichen Plasmafrequenzen in den orthogonalen Richtungen quantitativ überprüft werden. Dies kann realisiert werden, indem das System künstlich so präpariert wird, dass das Phasenteilchen immer aus demselben Minimum startet. So könnten Neben- und Hauptstrukturen separat untersucht werden. Außerdem sollte der physikalische Ursprung des

²Bei Phasendiffusion fällt zwar auch eine Spannung über dem SQUID ab, diese ist jedoch deutlich kleiner als die Spannung, die dem Spannungszustand entspricht, bei dem das Teilchen ohne angehalten zu werden dem Potentialverlauf folgt.

Rauschens, das die effektive Temperatur im Experiment erhöht, gefunden und, wenn möglich, eliminiert werden.

Was SQUID S2 angeht, könnte die Untersuchung der Phasendiffusion in zwei Dimensionen unter Einbeziehung der Hochfrequenzeigenschaften des parallelgeschalteten Kondensators und der restlichen Schaltung interessante Ergebnisse liefern. Außerdem ist die experimentelle Realisierung des Münchhausen Effekts noch nicht abgeschlossen. Bei Temperaturen, wie sie in einem Mischkryostaten erreichbar sind, sollte makroskopisches Tunneln bereits bei Strömen deutlich unterhalb des kritischen Stromes beobachtbar sein und somit auch der Münchhausen Effekt.

Bibliography

- [AH69] Vinay Ambegaokar and B. I. Halperin, *Voltage Due to Thermal Noise in the dc Josephson Effect*, Phys. Rev. Lett. **22** (1969).
- [BCS57] J. Bardeen, L. N. Cooper, and J. R. Schrieffer, *Theory of Superconductivity*, Phys. Rev. **108** (1957), no. 5.
- [BHL83] M. Büttiker, E. P. Harris, and R. Landauer, *Thermal activation in extremely underdamped Josephson-junction circuits*, Phys. Rev. B **28** (1983), no. 3, 1268–1275.
- [CT77] J. Clarke and C. D. Tesche, *dc-SQUID: Noise and optimization*, Journal of Low Temperature Physics **29** (1977), no. 3-4.
- [DSZN05] R. Dolata, H. Scherer, A. B. Zorin, and J. Niemeyer, *Single-charge devices with ultrasmall Nb/AlO_x/Nb trilayer Josephson junctions*, Journal of Applied Physics **97** (2005).
- [FD74] T. A. Fulton and L. N. Dunkleberger, *Lifetime of the zero-voltage state in Josephson tunnel junctions*, Phys. Rev. B **9** (1974), no. 11.
- [Gol] E. Goldobin, <http://www.geocities.com/goldexi/>.
- [GSH88] A. Greiner, W. Strittmatter, and J. Honerkamp, *Numerical integration of stochastic differential equations*, Journal of Statistical Physics **51** (1988).
- [Jos62] B. D. Josephson, *Possible new effects in superconductive tunnelling*, Physics Letters **1** (1962), no. 7.
- [KFU04] Y. Koval, M. V. Fistul, and A. V. Ustinov, *Enhancement of Josephson Phase Diffusion by Microwaves*, Phys. Rev. Lett. **93** (2004).
- [KM90] R. L. Kautz and John M. Martinis, *Noise-affected I-V curves in small hysteretic Josephson junctions*, Phys. Rev. B **42** (1990).
- [KNC⁺05] J. M. Kivioja, T. E. Nieminen, J. Claudon, O. Buisson, F. W. J. Hekking, and J. P. Pekola, *Observation of transition from escape dynamics to underdamped phase diffusion in a josephson junction*, Phys. Rev. Lett. **94** (2005), no. 24, 247002.
- [KO11] H. Kamerlingh Onnes, *Further experiments with Liquid Helium G. On the electrical resistance of Pure Metals etc. VI. On the Sudden Change in the Rate at which the Resistance of Mercury Disappears*, Koninklijke Nederlandse Akademie van Wetenschappen Proceedings Series B Physical Sciences **14** (1911).
- [Kra40] H. A. Kramers, *Brownian motion in a field of force and the diffusion model of chemical reactions*, Physica **7** (1940).
- [Lic91] Konstantin K. Licharev, *Dynamics of Josephson junctions and circuits*, Gordon and Breach, Philadelphia [u.a.], 1991.

- [LSTU⁺92] Valérie Lefevre-Seguin, Emmanuel Turlot, Cristian Urbina, Daniel Esteve, and Michel H. Devoret, *Thermal activation of a hysteretic dc superconducting quantum interference device from its different zero-voltage states*, Phys. Rev. B **46** (1992).
- [LYZ⁺02] Shao-Xiong Li, Yang Yu, Yu Zhang, Wei Qiu, Siyuan Han, and Zhen Wang, *Quantitative Study of Macroscopic Quantum Tunneling in a dc SQUID: A System with Two Degrees of Freedom*, Phys. Rev. Lett. **89** (2002).
- [MDC87] John M. Martinis, Michel H. Devoret, and John Clarke, *Experimental tests for the quantum behavior of a macroscopic degree of freedom: The phase difference across a Josephson junction*, Phys. Rev. B **35** (1987).
- [MK89] John M. Martinis and R. L. Kautz, *Classical phase diffusion in small hysteretic Josephson junctions*, Phys. Rev. Lett. **63** (1989), no. 14.
- [MLQ⁺05] J. Männik, S. Li, W. Qiu, W. Chen, V. Patel, S. Han, and J. E. Lukens, *Crossover from Kramers to phase-diffusion switching in moderately damped Josephson junctions*, Phys. Rev. B **71** (2005).
- [MO33] W. Meissner and R. Ochsenfeld, *Ein neuer Effekt bei Eintritt der Supraleitfähigkeit*, Naturwissenschaften **21** (1933), no. 44.
- [num07] *Numerical recipes : the art of scientific computing; source code CD-ROM*, 2007.
- [Sch97] Vadim V. Schmidt, *The physics of superconductors: Introduction to fundamentals and applications*, Springer, Berlin, 1997.
- [SP70] M. Simmonds and W. H. Parker, *Thermal Fluctuations in Superconducting Weak Links*, Phys. Rev. Lett. **24** (1970).
- [TGB09] A. U. Thomann, V. B. Geshkenbein, and G. Blatter, *Quantum instability in a dc-SQUID with strongly asymmetric dynamical parameters*, Phys. Rev. B **79** (2009), no. 18.
- [Tin04] Michael Tinkham, *Introduction to superconductivity*, 2. ed. ed., Dover Publ., Mineola, NY, 2004.
- [WLC⁺03] A. Wallraff, A. Lukashenko, C. Coqui, A. Kemp, T. Duty, and A. V. Ustinov, *Switching current measurements of large area Josephson tunnel junctions*, Review of Scientific Instruments **74** (2003).

Acknowledgments

First of all, I want to express my gratitude to Prof. Alexey Valentinowitsch Ustinov for giving me the opportunity to pursue this very interesting topic in his great group. Apart from the scientific support, I am indebted to him for generously allowing me to participate in the ski seminar and for giving me the chance to visit the DPG conference in Regensburg and the theorists' group in Zürich.

I also would like to thank Prof. Wulf Wulfhekel for being the second reviewer of this thesis.

I am indebted to Gianni Blatter, Vadim Geshkenbein and Alexander Thomann at the ETH Zürich for initializing the topic, for inviting me to Zürich and for several very helpful discussions.

I am very grateful to Alexey Feofanov, who designed the chips, introduced me to cryophysics and always had an answer up his sleeve if I ran out of them.

I also would like to thank Kirill Fedorov, who always helped with the cryostat whenever strong arms were needed and never refused any scientific or other discussion. Additionally, his efforts of trying to teach me Russian are very much appreciated.

Alexandr Lukashenko's magic hands in repairing the fridge and his huge knowledge about cryophysics, which he was always ready to share, are greatly acknowledged.

Hannes Rotzinger earned being mentioned in this list by his great ability of asking the right questions and always being willing to share his vast knowledge about physics and movies.

I also want to thank the whole group. I am indebted to everybody for making this year as enjoyable and instructive as it was. I especially want to thank everybody in the diplomands' room for the productive, helpful and fun atmosphere that made working there a pleasure.

Jürgen Lisenfeld and many others earn my thanks for proof reading this thesis.

I also have to say thanks to everybody in the Fachschaft and its corona. Among all those people, without whom my life would have been so much more boring I want to especially thank Julian Merkert, Jens Küchenmeister and very specially Rolf Schön and Tobias Märkl, who all started this journey with me, were great company and never left. And then there are Christina Stawiarski and Rosmarie Blomley, the much needed and even more appreciated female support.

Last but certainly not least I want to thank my sister Annika, my mum Anita, her partner Rudolf and my dad Roland for believing in me and supporting me throughout my studies (and the rest of my life). Without them nothing of this would have been possible.

Erklärung

Hiermit erkläre ich, diese Arbeit selbstständig und unter ausschließlicher Verwendung der angegebenen Literatur angefertigt zu haben.

(Ort, Datum)

(Susanne Butz)